Title

Ultrastructure of Melanopsin-Expressing Retinal Ganglion Cell Circuitry in the Retina and Brain Regions that Mediate Light-Driven Behavior

Author

Liu, Yu Hsin

Publication Date

2017

Peer reviewed|Thesis/dissertation

UNIVERSITY OF CALIFORNIA, SAN DIEGO

Ultrastructure of Melanopsin-Expressing Retinal Ganglion Cell Circuitry in the Retina and Brain Regions that Mediate Light-Driven Behavior

A dissertation submitted in partial satisfaction of the
Requirements for the degree Doctor of Philosophy

in

Neurosciences

by

Yu Hsin Liu

Committee in charge:

Professor Satchidananda Panda, Chair
Professor Mark Ellisman, Co-Chair
Professor Nicola Allen
Professor Brenda Bloodgood
Professor Ed Callaway
Professor David Welsh

2017

This Dissertation of Yu Hsin Liu is approved,

and it is acceptable in quality and form

for publication on microfilm and electronically:

_____

_____

_____

_____

_____
Co-Chair

_____
Chair

University of California, San Diego

2017

TABLE OF CONTENTS

LIST OF FIGURES

ACKNOWLEDGEMENTS

I would like to acknowledge and thank my thesis advisor Dr. Satchidananda Panda. His devotion to science and discovery is matched only by his dedication to my success and the success of his lab members. I will always be grateful for his guidance and mentorship over these past four years and for his faith in me as I ventured down an uncharted path by taking on the projects described in this dissertation. I hope to one day be able to pay it forward. I would also like to acknowledge and thank my co-chair Mark Ellisman for his encouragement and guidance throughout my research studies and his seemingly limitless knowledge about all things microscopic.

I would like to acknowledge and thank my dissertation committee members Nicola Allen, Brenda Bloodgood, Ed Callaway, and David Welsh for their infectious love of science and for all of their encouragement and support.

I would like to acknowledge and thank everyone in the Panda lab for all of their help and support throughout the years. I would especially like to thank: Hiep Le for keeping the lab running and being the go-to guy for all things, Luis Rios for being ever-patient with me as we bounced ideas off of each other and figured out how to move forward with our tracing studies, and Emily Manoogian for always being on my side. I would also like to acknowledge my team of undergraduate researchers Benjamin Finander, Kevin Nguyen, Tanya Kantak, and Xinyue (Tracy) Chen for all of their help in the final stages of my studies. It has been a pleasure and a privilege to work with you all.

I would specifically like to thank Christine Keunyoung Kim for all of her help with the optimizing and executing the tissue processing, electron microscopy, and image processing. Without her hard work and guidance, the projects described in this dissertation would not be possible. She was always available to answer my endless questions and is always a very positive and encouraging voice of reason.

I would like to thank and acknowledge my teammates Alie Caldwell, Brandon Cisneros, Micah Caldwell, Vladimir Jovanovic, and Vy Vo for picking me up when I was down, for carrying me when I was tired, and for being upstanding citizens as we traveled to end of the world and back; and my friends David Adamowicz, Tido (Eric) Geier, and Priya Nayak for walking this long path with me and always having my back. My time here at UCSD would be poorer for lack of your camaraderie, strengths and perspectives.

I would like to thank my mom and dad, Nicole and Tom Liu, and my brother Charles Liu for their unquestioning love and support over the years. They were there from the beginning, and I would not have gotten this far without them.

Finally, I would like to acknowledge my husband, Steven D. Brown. His integrity and love of science is a constant inspiration for me to be an ever-better scientist and his confidence in me and love for me has been the light by which I travel into this and that. Because of him, I am exactly where I want to be.

I have been supported by the Aginsky Endowment, the Ruth L. Kirschstein Individual Predoctoral MD/PhD National Research Service Award

Grant F30EY025560, and the Medical Scientist Training Program Grant NIGMS07198.

Chapter 2 is currently being prepared for submission for publication of the material. Kim, Keunyoung; Liu, Cindy Yu Hsin; Rios, Luis; Perez, Alex; Phan, Sebastien; Garcia, Guadalupe C.; Ju, Suyeon; Ellisman, Maya; Ellisman, Mark; Panda, Satchidananda. I am the primary investigator and will be co-first author on this paper with Keunyoung Kim who performed and optimized all of the tissue processing, electron microscopy, and image processing. Luis Rios contributed significant segmentation and quantification. Alex Perez contributed the autosegmentation results. Mark Ellisman and Satchidananda Panda directed and supervised the research.

Chapter 3 is currently being prepared for submission for publication of the material. Liu, Cindy Yu Hsin; Kim, Keunyoung; Rios, Luis; Garcia, Guadalupe; Ellisman, Mark; Panda, Satchidananda. I am the primary investigator and first author of this material. Keunyoung Kim performed the tissue preparation, electron microscopy, and image processing. Luis Rios contributed some help with the data analysis. Guadalupe Garcia was a tremendous help with the automatic segmentation. Mark Ellisman and Satchidananda Panda directed and supervised the research.

VITA

2008	Bachelor of Arts, Neurosciences. Johns Hopkins University
2011-2019	Medical Scientist Training Program. University of California, San Diego
2017	Doctor of Philosophy, Neurosciences University of California, San Diego – La Jolla, CA

PUBLICATIONS

Kang E, Kim JY, **Liu CY**, Xiao B, Chen PY, Kristian K, Worley P, Song H, Ming GL. Rheb1 mediates DISC1-dependent regulation of neuronal development in the adult hippocampus. Neurogenesis. 2015 Nov 10;2(1):e1081715.

Zhou, M, Li W, Huang S., Song J, Kim JY, Tian X, Kant E, Sano Y, **Liu C**, Balaji J, Wu S, Zhou Y, Zhou Y, Parivash S, Ehninger D, He L, Song H, Ming GL, Silva A. mTOR inhibition ameliorates cognitive and affective deficits caused by Disc1 knockdown in adult-born dentate granule neurons. Neuron. 2013 Feb 20;77(4):647-54.

Kim JY, **Liu CY**, Zhang F, Duan X, Wen Z, Song J, Feighery E, Lu B, Rujescu D, St Clair D, Christian K, Callicott JH, Weinberger DR, Song H, Ming GL. Interplay between DISC1 and GABA signaling regulates neurogenesis in mice and risk for schizophrenia. Cell. 2012 Mar 2: 148(5): 1051-64.

Kim PM, Duan X, Huang AS, **Liu CY**, Ming GL, Song H, Snyder SH. Aspartate Racemase, Generating Neuronal D-Aspartate, Regulates Adult Neurogenesis. Proc Natl Acad Sci USA. 2010 Feb 16; 107(7):3175-9.

Kim JY, Duan X, **Liu CY,** Jang M, Guo JU, Pow-anpongkul N, Kang E, Song H, Ming G. DISC1 Regulates New Neuron Development in the Adult Brain via Modulation of AKT-mTOR Signaling through KIAA1212. Neuron. 2009 Sep 24; 63(6):761-73.

Duan X, Kang E, **Liu CY**, Ming GL, Song HJ. Development of Neural Stem Cell in the Adult Brain. Current Opinions in Neurobiology. 2008 May 29; 18:108-155

Duan X, Chang JH, Ge S, Faulkner RL, Kim JY, Kitabatake Y, Liu XB, Yang CH, Jordan JD, Ma DK, **Liu CY**, Ganesan S, Cheng HJ, Ming GL, Lu B, Song H. Disrupted-in-schizophrenia 1 Regulates Integration of Newly Generated Neurons in the Adult Brain. Cell. 2007 Sep; 130(6):1146-58.

ABSTRACT OF THE DISSERTATION

Ultrastructure of Melanopsin-Expressing Retinal Ganglion Cell Circuitry in the Retina and Brain Regions that Mediate Light-Driven Behavior

by

Yu Hsin Liu

Doctor of Philosophy in Neurosciences

University of California, San Diego, 2017

Professor Satchidananda Panda, Chair

Professor Mark Ellisman, Co-Chair

Melanopsin-expressing retinal ganglion cells (mRGC) are intrinsically photosensitive and combine their melanopsin-based photoresponses with rod and cone signals to convey light information to a subset of retinal brain targets. mRGC axons to non-image forming (NIF) visual centers are essential for the proper functioning of processes like circadian photoentrainment and pupillary light reflex. Surprisingly, mRGCs also send axons to image-forming regions of the brain. It is unknown how mRGCs mediate such diverse functions.

Classically, a cell's morphology and location in a biological system is a direct reflection of its synaptic connections and, by definition, their function. mRGCs can be divided into five subtypes (M1-M5) based on morphology and dendritic stratification in the inner plexiform layer. In the classical sense, since M1s send axons to only a subset of mRGC-target regions and are the only subtype that monostratify in the OFF-sublamina, M1s likely serve a distinct function from other subtypes. However, M1s, like all mRGCs, exhibit an ON-response. This reveals a hole in what we understand about intraretinal connectivity and attenuates the weight that should be afforded to stratification in determining function. While the other mRGC subtypes have distinct morphology and branching patterns, it is unknown whether they serve specific functions. Thus, in order to explore the structure-function relationship of mRGC subtypes, we must consider connectivity. Unfortunately, the variable expression of melanopsin protein between subtypes and across the architecture of a single mRGC and the lack of unique markers for up- and downstream interactors has precluded rigorous study of mRGC connectivity in the retina and central targets.

We use a correlated light and electron microscopy label and serial blockface scanning electron microscopy to explore the architecture and synaptic partners of mRGCs in an attempt to better understand the connectivity of mRGC subtypes. We show significant differences in the ultrastructure of mRGC axonal terminals in mRGC-recipient brain regions, stratification-specific differences in mRGC dendrites, and catalog the intraretinal connections specific to mRGC subtypes.

Chapter 1

General Introduction

The brain is a world consisting of a number of unexplored continents and great stretches of unknown territory.

- Ramon y Cajal (1906)

Light is important. Light allows us to see- to create a virtual representation of the physical world within our mind so that we can navigate our surroundings. Light also colors our life- alerting us to the dangers of various garishly colored organisms and inspiring our imaginations with the dazzling palettes of wildflowers and rainbows. However, beyond informing us about the surrounding environment, light also plays important roles in human behavior and physiology. The appreciation and fascination in what and how we see is reflected in the fact that vision is the most heavily and thoroughly studied sensory system.

The retina lines the back of the eye and is a self-contained neural system made up of millions of interconnected cells that collect, translate, and parse all the light information from our physical surroundings into signals to the brain that allow us to see and estimate the time of day. The precise connectivity of these the cells in the retina with each other and with the regions of the brain that piece together that information is crucial to vision. In the past twenty years, a new type

of photosensitive cell in the eye has been discovered that is absolutely essential for non-image forming (NIF) visual processes such as the synchronization of an organism's behavior and physiology to the time of day and constricting the pupil in response to bright light. These cells do not reside in the photoreceptor layer like the canonical light sensitive cells, the rods and cones, but instead are retinal ganglion cells in the ganglion cell layer that express the photopigment melanopsin. Axons from these melanopsin-expressing retinal ganglion cells (mRGCs) project specifically to regions of the brain that mediate NIF visual processes such as the suprachiasmatic nucleus, the intergeniculate leaflet, and the olivary pretectal nucleus (Berson, Dunn, and Takao 2002; Hattar et al. 2002). More recently, new subtypes of mRGCs have been shown to project to regions of the brain that are canonically known to be image-forming visual regions (Brown et al. 2010; Ecker et al. 2010). Without the benefit of decades upon decades of research, as has been dedicated to image-forming vision, the pre-synaptic and post-synaptic partners involved in mRGC circuitry in the eye and brain are largely unknown.

In this thesis dissertation, I present two bodies of work that elucidate the interactions between mRGCs and downstream cells in target brain regions and upstream cells in the retina. To better understand the context of this thesis work, I have provided some background information about retinal circuitry and what is known about mRGCs and mRGC circuitry.

1.1 Retinal circuitry

The mammalian retina lines the back half of the eye and is made up of five main cell types: photoreceptor cells, bipolar cells, horizontal cells, amacrine cells, and retinal ganglion cells. These cells are organized (starting from closest to the center of the eye) into three nuclear layers: the ganglion cell layer (GCL), which contains the cell bodies of retinal ganglion cells, inner nuclear layer (INL), which contains the cell bodies of amacrine, bipolar, and horizontal cells, and outer nuclear layer (ONL, or photoreceptor layer), which contains the cell bodies of the photoreceptor cells. These nuclear layers are separated from one another by layers of cell processes called the inner plexiform layer (IPL), which separates GCL from INL and contains dendritic processes of retinal ganglion cells, axonal processes of bipolar cells, and dendritic processes of amacrine cells, and the outer plexiform layer (OPL), which separates INL from ONL and contains the axon terminals of photoreceptors, dendrites of bipolar cells, and all horizontal cell processes (Figure 1.1).

When light enters the eye through the pupil and is incident upon the retina, photons must pass through the entire thickness of the retina to be absorbed by the *11-cis-retinal* bound to light-sensitive rhodopsin and cone opsin on rod and cone photoreceptors, the canonical light sensitive cells in the retina. The absorption of photons by the *11-cis-retinal* photoisomerizes the *11-cis-retinal* to *all-trans-retinal* which activates G-proteins in the rods and cones that ultimately lead to hyperpolarization. When light stimulation is removed, the rods and cones will then depolarize leading to the release of glutamate. The hyperpolarization and depolarization in rods and cones leads to decreases and increases in

glutamate release, respectively, around a baseline level from the photoreceptor terminals, rod spherules and cone pedicles, onto horizontal and bipolar cell processes in the outer nuclear layer (Ayoub and Copenhagen 1991). In addition to chemical synapses at their terminals, gap junctions have been shown to link rod and cone photoreceptors in the OPL (Kolb 1977).

Horizontal cells have cell bodies in the inner nuclear layer and processes that stratify in the OPL where they integrate rod and cone signals across large swaths of retina to signal luminance. There are two main types of horizontal cell: A-type, which are axonless, and B-type which have axons. In mammals, the dendrites of both A- and B-type contact cone pedicles and only the axons of B-type horizontal cells contact rod spherules (Bloomfield and Miller 1982). Both types hyperpolarize in response to light stimuli and are known to feed back to photoreceptor terminals in such a way that increases neurotransmitter release from cones. Horizontal cells are also known to make gap junctions with other horizontal cell processes within the IPL (Mills and Massey 1994) and to feed forward to bipolar cells (Kolb and Jones 1984).

Bipolar cells, like horizontal cells, have cell bodies that are found in the distal inner nuclear layer (INL). In response to glutamate release from photoreceptor terminals onto bipolar cell dendrites in the OPL, bipolar cells will react by hyperpolarizing or depolarizing (Werblin and Dowling 1969). Due to the expression of metabotropic glutamate receptors (Nakajima et al. 1993; Nomura et al. 1994), ON-bipolar cells will hyperpolarize in response to glutamate release (signaling lights off) from rod and cone photoreceptors. The metabotropic

glutamate receptor is coupled to a G-protein which, when activated, leads to the closure of ion channels (Koike et al. 2010). When lights are present, the decrease in glutamate release from the photoreceptor terminals releases the inhibition on ON-bipolar cells, allowing them to depolarize. OFF-bipolar cells, which express ionotropic glutamate receptors, will depolarize in response to glutamate release from rods and cones in the absence of light. Depolarization causes the release of glutamate from bipolar cell terminals in the inner plexiform layer (IPL).

ON- and OFF-bipolar cell axons ramify in very specific layers in the IPL where they synapse with retinal ganglion cell dendrites. OFF-bipolar cells have axons that stratify in the outer half of the IPL (sublamina *a* or OFF-sublamina) where they interact with OFF-retinal ganglion cells, and ON-bipolar cell axons stratify in the inner half of the IPL (sublamina *b* or ON-sublamina) where they interact with ON-retinal ganglion cells (Famiglietti and Kolb 1976). The specific input from rod or cone photoreceptor and the strata in which they stratify has been used to separate the bipolar cells in mice into nine cone bipolar cell types (four OFF-cone bipolar cells and five ON-cone bipolar cells) and one type of rod bipolar cell which stratifies in the ON-sublamina (Ghosh et al. 2004).

Of all bipolar cell types, the rod bipolar cell type is the most easily recognizable because of its characteristic dendritic interaction with rod spherules and its axonal arborization deep into the ON-sublamina of the IPL ending in a bulbous terminal in the layer closest to the ganglion cell layer. Though rod bipolar cell terminals are very close to retinal ganglion cells (RGC), they do not contact RGCs directly, instead synapsing on AII amacrine cells which transfer rod bipolar

cell signals to retinal ganglion cells via chemical synapses with OFF-bipolar cells or gap junctions to ON-bipolar cell axons (Kolb and Famiglietti 1974). Two other ways that rod signals reach the RGCs is via gap junctions between rod and cone photoreceptors whereby rod signals get passed to cone photoreceptors and thus to cone bipolar cells (Raviola and Gilula 1973) and via direct dendritic contact between OFF-cone bipolar cells and rods (Li, Chen, and DeVries 2010).

Amacrine cells are a heterogeneous type of cell with cell bodies in the proximal half of the INL and dendrites that stratify in the IPL (Kolb, Nelson, and Mariani 1981). The over 30 types of amacrine cells in the mouse retina make up ~40% of the neurons in the INL and ~59% of neurons in the GCL (Jeon, Strettoi, and Masland 1998) and differ from each other in size, ramification within the IPL, branching pattern, and neurotransmitter patterns (MacNeil and Masland 1998; Masland 2012). Amacrine cells synapse with bipolar cell axons and RGC dendrites in the IPL and integrate, modulate, and add a temporal aspect to the light information being presented to RGCs. Most amacrine cells are inhibitory-containing the neurotransmitters GABA or glycine (Menger, Pow, and Wassle 1998; Balasubramanian and Gan 2014)- and GABAergic amacrine cells often make reciprocal synapses with bipolar cells (Pourcho and Goebel 1983).

Finally, after being detected by photoreceptors, integrated by horizontal cells, passed to bipolar cells, and modulated by amacrine cells, light information finally reaches the RGCs. RGC axons are the only way that light information can reach the brain. RGCs have somas in the GCL (~41% of all cell bodies in the GCL, the remainder being displaced amacrine cells), dendrites that stratify in the

IPL, and axons that course along the innermost edge of the retina toward the optic disc where they come together to form the optic nerve. There are upwards of ~22 different ganglion cell types in the mouse retina that are identified based on soma size, soma shape, dendritic field diameter, dendritic morphology, dendritic branching pattern, and stratification levels within the IPL (Volgyi, Chheda, and Bloomfield 2009). Physiologically, some ganglion cells respond maximally to the presence or absence of light or movement in general or in a specific direction; others respond to particularly oriented images/edges (Kong et al. 2005). Ultimately, ganglion cells are a heterogeneous population of cells that receive input from bipolar and amacrine cells in the IPL and convey processed light information to image-forming regions of the brain via action potentials down axonal projections to the lateral geniculate nucleus (LGN) and superior colliculus (SC) where they signal through the release of glutamate. 90% of all RGC axons leaving the eye end up at the LGN with the remainder projecting to the SC or making up the retinohypothalamic tract which terminates in the pretectum (to control pupillary light reflex), the suprachiasmatic nucleus (to synchronize activity cycles to environmental lighting conditions), and other regions like the ventrolateral preoptic nucleus (to regulate sleep) (Schmidt, Chen, and Hattar 2011).

1.2 Current state of knowledge regarding mRGC circuitry

1.2.1 mRGCs are essential for non-image forming visual processes

As the above text has briefly introduced, the circuitry involved in image-forming vision is largely understood. However, much less is known about the retinal circuitry that forms the basis of the retinohypothalamic tract and informs non-image forming (NIF) visual processes such as the synchronization of sleep and activity rhythms to environmental lighting conditions (circadian photoentrainment), the constriction of pupils in response to light stimulation (pupillary light reflex, PLR), the acute modulation of activity by light (negative masking), and sleep regulation. Considering that these NIF visual functions are mediated by axonal projections from the retina, it may come as a surprise that these NIF visual processes persist despite the loss of rod and cone photoreceptors (Foster et al. 1991; Freedman 1999; Keeler 1927).

The suprachiasmatic nucleus (SCN) is necessary for circadian behavior and physiology such as daily patterns in water drinking and activity, changes in serum corticosterone, and fertility (Stephan and Zucker 1972; Moore and Eichler 1972; Wiegand and Terasawa 1982) and is the seat of the master pacemaker of body-wide circadian rhythms (Lehman et al. 1987; Ralph et al. 1990). Experiments using engineered pseudorabies virus to anterogradely label RGC projections in mutant mice without rods and cones (*rd/rd*) showed that the RGCs in mice projected to regions of the brain that were known to be essential for circadian rhythms and other NIF visual processes: SCN, intergeniculate leaflet, ventral lateral geniculate nucleus, and the pretectum (which includes the olivary pretectal nucleus) (Provencio, Cooper, and Foster 1998). To identify the cells that were sending axons specifically to the SCN, fluorescent microspheres were

injected into the SCN of wildtype rats. The retrograde transport of these microspheres identified a small subset of sparsely but evenly distributed retinal ganglion cells that were intrinsically photosensitive- responding maximally to ~480 nm light with large persistent depolarizations to light- and had relatively large soma sizes, and dendrites that largely stratified in the outer sublamina of the inner plexiform layer (Berson, Dunn, and Takao 2002). The distribution pattern and maximal sensitivity of these intrinsically photosensitive retinal ganglion cells was similar to that of melanopsin (*Opn4*), a novel opsin identified in *Xenopus* (Provencio et al. 2000) and the intrinsically photosensitive RGCs retrogradely labeled from the SCN were shown to be immunopositive for the expression of melanopsin protein (Hattar et al. 2002). These melanopsin-expressing retinal ganglion cells were shown to send axonal projections to the SCN, intergeniculate leaflet (IGL) , and olivary pretectal nucleus (OPN)- NIF visual centers (Hattar et al. 2002)

Melanopsin is an opsin-class protein that is very similar in amino-acid sequence to invertebrate opsins (Provencio et al. 1998) as opposed to ciliary opsins, the class to which rod and cone opsins belong. Like rod and cone opsins, melanopsin is a G-protein coupled receptor that is expressed on the cell surface and uses the chromophore 11-*cis*-retinal. However, unlike rod and cone opsins, melanopsin can form a stable bond with all-*trans*-retinal and regenerate the 11-*cis* form through photoisomerization (Panda et al. 2005). As previously mentioned, mice without rods and cones, but intact melanopsin-expressing retinal ganglion cells (mRGCs) have functional NIF visual processes- suggesting

that melanopsin is sufficient for driving NIF vision. However, melanopsin and rod and cone opsins must play a complementary role in informing NIF visual processes as transgenic mice that do not express melanopsin (*Opn4*$^{-/-}$) have circadian photoentrainment, intrinsic circadian period lengths, and photic suppression of melatonin production, similar to wildtype animals and only some attenuation in phase shifting, negative masking and pupillary light reflex at high irradiance levels (Panda et al. 2002, 2003). As all non-image forming visual processes are lost in mice that lack rods, cones, and melanopsin (*rd/rd; Opn4*$^{-/-}$) (Panda et al. 2003), rod, cone, and melanopsin signals must all be integrated at the circuit level within the retina. Studies involving the specific ablation of mRGCs in the adult retina reveal that despite the presence of rods and cones and having intact image-forming vision, adult mice with ablated mRGCs had complete loss of circadian photoentrainment, pupillary light reflex, and negative masking (Hatori et al. 2008; Güler et al. 2008). Thus, mRGCs are absolutely essential for NIF visual processes.

1.2.2 mRGC subtypes

Studying the mRGC circuitry- by which light information reaches the NIF visual centers of the brain- is difficult. mRGCs make up only 2-5% of all RGCs and are thus sparsely distributed across the retina- requiring the careful acquisition and processing of large amounts of tissue to study. Also, not all mRGCs are created equal. The first mRGCs identified by incorporating a *tau-lacZ* reporter gene into the mouse melanopsin locus (*Opn4*$^{tau\text{-}lacZ}$) and then staining

tissue with X-gal only described a seemingly uniform population of mRGCs (now known to be the M1 subtype) that had dendrites that stratified in the OFF-sublamina of the IPL (Hattar et al. 2002). However, the use of highly sensitive antibodies to melanopsin revealed that mRGC dendrites stratify in the ON-sublamina as well (Provencio, Rollag, and Castrucci 2002) suggesting the presence of other subtypes of melanopsin-expressing retinal ganglion cell.

Ultimately, by using transgenic mice that express Cre-recombinase driven by the melanopsin promoter (Hatori et al. 2008; Ecker et al. 2010), five morphologically-defined mRGC subtypes (M1 through M5) have been identified based on soma size and dendritic branching pattern, field diameter, and stratification in the inner plexiform layer (IPL). Of these five subtypes, only three, M1, M2, and M3, express enough melanopsin to be detectable via immunohistochemistry. Figure 1.2 summarizes the morphological differences between the subtypes, but briefly, M1 mRGCs have somas around 15 um in diameter, dendritic field sizes ~350 um in diameter, and dendrites that stratify in the OFF-sublamina in the IPL. M2 mRGCs have slightly larger somas, ~17 um, similar dendritic field sizes to M1 and stratify solely in the ON-sublamina of the IPL. M3 mRGCs stratify in both the OFF- and ON-sublamina and have soma and dendritic field diameters between those of M1 and M2. M4 and M5 both stratify solely in the ON-sublamina, like M2, but M4 somas are significantly larger, > 19 um in diameter, and M5 somas are significantly smaller, <15 um in diameter, as compared to M2. Also, M4 dendrites have more branch points, total dendritic length, and thicker axons than M2 and M5 mRGCs have compact, highly

branched dendrites with a dendritic field diameter of ~200 um (Baver et al. 2008; Schmidt and Kofuji 2009; Estevez et al. 2012; Schmidt and Kofuji 2011; Ecker et al. 2010).

1.2.3 mRGC intraretinal circuitry

One of the underlying principles in retina circuitry is that an RGC's dendritic stratification in the various strata of the IPL predicts its response to light stimulation. For example, an RGC that has dendrites in the distal IPL, or a-sublamina, or OFF-sublamina, fires when lights are not present. Conversely, an RGC that has dendrites in the inner IPL (b-sublamina, or ON-sublamina) fires action potentials in the presence of light (Famiglietti and Kolb 1976). In a surprising break from these principles, all mRGCs, regardless of where their dendrites stratify exhibit on ON-response, depolarizing in response to the presence of light (Tu et al. 2005; Schmidt and Kofuji 2011; Estevez et al. 2012). How this ON-response is mediated in this OFF-stratifying RGC and in the bistratified M3 mRGC is largely unknown.

While mRGCs are intrinsically photosensitive and can convey light information to NIF visual centers of the brain without the presence/function of rods and cones, rod and cones can contribute to NIF visual processes through mRGCs (Hatori et al. 2008; Hattar et al. 2003; Panda et al. 2002). In general, mRGC dendrites stratify in the IPL and receive input from bipolar cells and amacrine cells and send axons to many different regions of the brain. Specifically, M1 mRGC dendrites stratifying in the outer sublamina of the IPL have been

shown by immunohistochemistry to be postsynaptic to amacrine cell processes and ectopic ON bipolar cell processes (Dumitrescu et al. 2009) and by retrograde viral labeling to be postsynaptic to dopaminergic amacrine cells (Viney et al. 2007). ON-stratifying mRGC processes have also been shown by EM to be postsynaptic to bipolar cells and amacrine cells in the inner IPL (Belenky et al. 2003) and by retrograde labeling to be postsynaptic to monostratified amacrine cells and type 8 cone bipolar cells in the inner IPL (Viney et al. 2007). An immunohistochemical approach using light microscopy showed that molecular markers for rod bipolar cells were colocalized with markers for ribbon synapses directly adjacent to melanopsin-positive RGCs- suggesting that rod bipolar cells have direct contact with mRGCs (Østergaard, Hannibal, and Fahrenkrug 2007).

Outside of the few immunolabeling and immunoEM studies, no further specification of the interactions between mRGCs and the 10 different mouse bipolar cell types and over 30 different amacrine cell types is known. Hindered by the lack of specific markers for subtypes of mRGCs, the fact that not all mRGCs can be immunolabeled with antibodies to melanopsin, and because there is a dearth of known unique molecular markers for different bipolar and amacrine cell types, there is a need for an unbiased approach for studying mRGC interactions in the retina.

1.2.4 mRGC interactions in mRGC-recipient brain regions

In terms of central projections, most mRGC axons project equally to both sides of the SCN and contralateral OPN and 20% of mRGC axons will project to

ipsilateral IGL (Gooley et al. 2003; Ecker et al. 2010). The use of *Opn4*^{Cre} mice, a more sensitive transgenic mouse line, showed that in fact, mRGCs also project to dorsal and ventral lateral geniculate nucleus (dLGN, vLGN) and superior colliculus (Ecker et al. 2010). In the search for subtype-specific projections, there have been suggestions that 80% of SCN projections come from M1 mRGCs and that M1 and M2 mRGCs project to the OPN approximately equally (Baver et al. 2008). A comparison between M1 and non-M1 mRGC central projections suggested that both M1 and non-M1 mRGCs project to the SCN and IGL and that non-M1 mRGCs send the vast majority of projections to the dLGN, vLGN, OPN core, posterior pretectal nucleus, and superior colliculus (Ecker et al. 2010). In fact, M4 mRGCs were preferentially labeled by injections of a retrograde label injected into the dLGN suggesting that M4 mRGCs may play a role in pattern vision (Estevez et al. 2012).

As it seems that different subtypes of mRGCs preferentially send axons to different target brain regions and that mRGC subtypes are morphologically and physiologically different, one would expect to be able to observe differences in mRGC terminals across brain regions. mRGCs mediate both pupillary light reflex which occurs on the order of milliseconds to seconds and circadian photoentrainment which requires hours of light stimulation to cause an effect. How one genetically-defined cell type mediates effects that vary so greatly in timescale is unknown. Short of the fact that mRGCs have been traced to different brain regions, very few details regarding differences in mRGC axon terminal across brain regions are known.

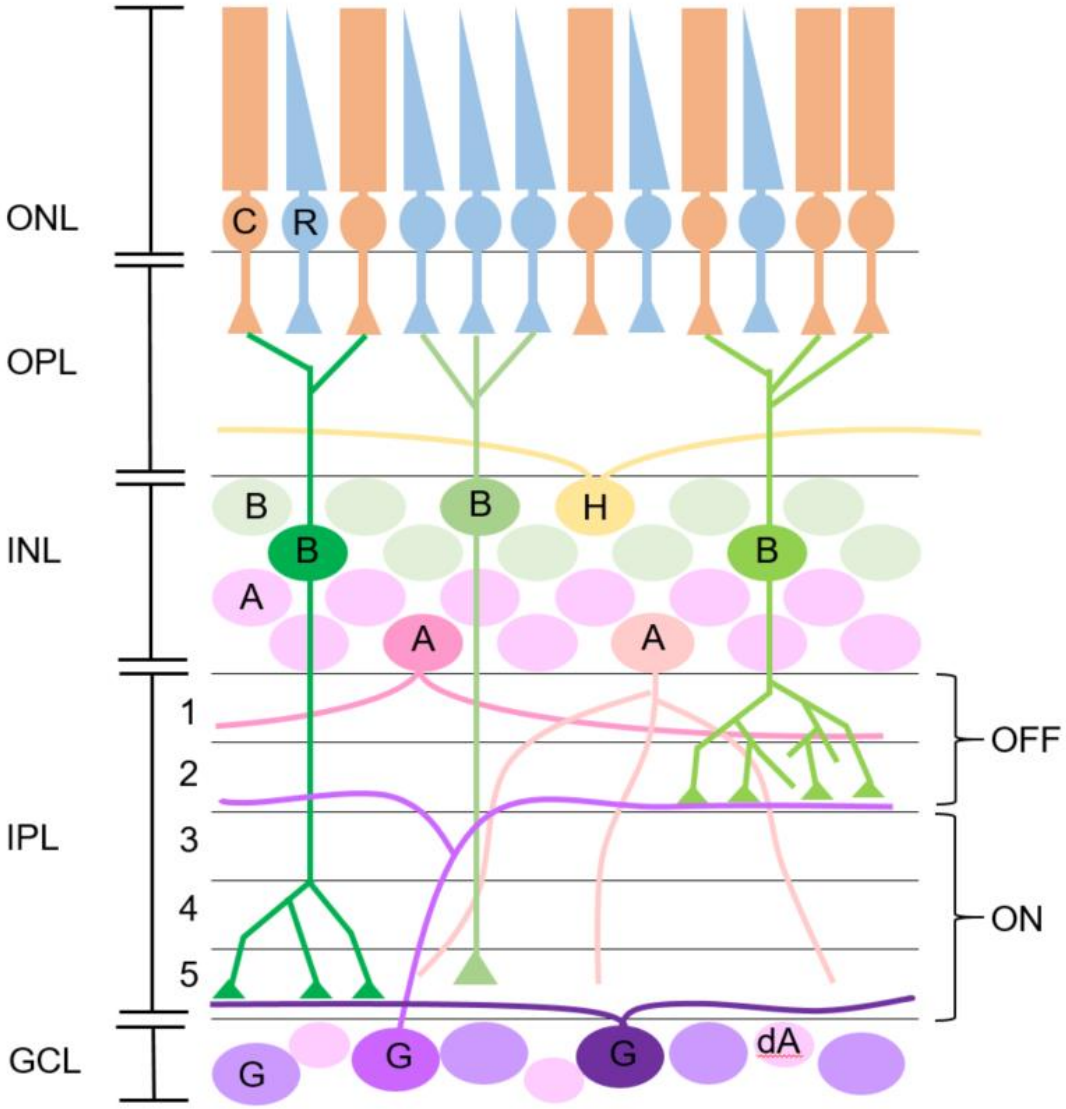

Figure 1.1 Layers of the retina

ONL: outer nuclear layer; OPL: outer plexiform layer; INL: inner nuclear layer; IPL: inner plexiform layer, strata 1-5, OFF sublamina, ON sublamina; GCL: ganglion cell layer; C: cone photoreceptor; R: rod photoreceptor; B: bipolar cell; A: amacrine cell; H: horizontal cell; G: ganglion cell; dA: displaced amacrine cell.

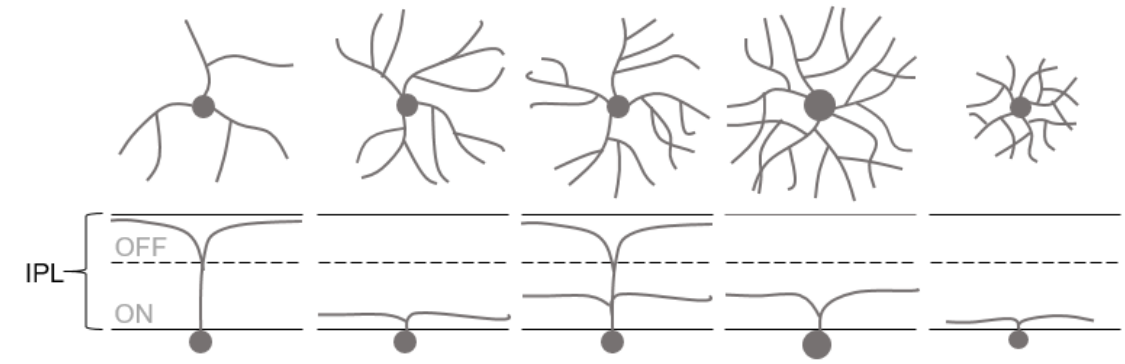

Subtype	M1	M2	M3	M4	M5
Soma Diameter	++	+++	+++	++++	+
Dendritic Field	++	+++	+++	++++	+

Figure 1.2 Morphology of mRGC subtypes

Top row: *En face* schematic of different mRGC subtypes. Second row: Schematic of cross-sectional view showing typical dendritic stratification pattern for each subtype. Bottom: comparisons between soma and dendritic field diameters between mRGC subtypes.

1.3 References

Ayoub, George S., and David R. Copenhagen. 1991. “Application of a Fluorometric Method to Measure Glutamate Release from Single Retinal Photoreceptors.” *Journal of Neuroscience Methods* 37 (1): 7–14.

Balasubramanian, Revathi, and Lin Gan. 2014. “Development of Retinal Amacrine Cells and Their Dendritic Stratification.” *Current Ophthalmology Reports* 2 (3): 100–106.

Baver, Scott B, Galen E Pickard, Patricia J Sollars, and Gary E Pickard. 2008. “Two Types of Melanopsin Retinal Ganglion Cell Differentially Innervate the Hypothalamic Suprachiasmatic Nucleus and the Olivary Pretectal Nucleus.” *The European Journal of Neuroscience* 27 (7): 1763–70.

Belenky, Michael A, Cynthia A. Smeraski, Ignacio Provencio, Patricia J. Sollars, and Gary E. Pickard. 2003. “Melanopsin Retinal Ganglion Cells Receive Bipolar and Amacrine Cell Synapses.” *The Journal of Comparative Neurology* 460 (3): 380–93.

Berson, David M, Felice A Dunn, and Motoharu Takao. 2002. “Phototransduction by Retinal Ganglion Cells That Set the Circadian Clock.” *Science (New York, N.Y.)* 295 (5557): 1070–73.

Bloomfield, Steward A., and Robert F. Miller. 1982. “A Physiological and Morphological Study of the Horizontal Cell Types of the Rabbit Retina.” *The Journal of Comparative Neurology* 208 (3): 288–303.

Brown, Timothy M, Carlos Gias, Megumi Hatori, Sheena R Keding, Ma’ayan Semo, Peter J Coffey, John Gigg, Hugh D Piggins, Satchidananda Panda, and Robert J Lucas. 2010. “Melanopsin Contributions to Irradiance Coding in the Thalamo-Cortical Visual System.” *PLoS Biology* 8 (12): e1000558.

Dumitrescu, Olivia N., Francesco G. Pucci, Kwoon Y. Wong, and David M. Berson. 2009. “Ectopic Retinal ON Bipolar Cell Synapses in the OFF Inner Plexiform Layer: Contacts with Dopaminergic Amacrine Cells and Melanopsin Ganglion Cells.” *Journal of Comparative Neurology* 517 (2): 226–44.

Ecker, Jennifer L, Olivia N Dumitrescu, Kwoon Y Wong, Nazia M Alam, Shih-Kuo Chen, Tara LeGates, Jordan M Renna, Glen T Prusky, David M Berson, and Samer Hattar. 2010. “Melanopsin-Expressing Retinal Ganglion-Cell Photoreceptors: Cellular Diversity and Role in Pattern Vision.” *Neuron* 67 (1). Elsevier Ltd: 49–60.

Estevez, ME, PM Fogerson, MC Ilardi, Bart G Borghuis, E Chan, S Weng, ON

Auferkorte, Jonathan B Demb, and David M. Berson. 2012. “Form and Function of the M4 Cell, an Intrinsically Photosensitive Retinal Ganglion Cell Type Contributing to Geniculocortical Vision.” *Journal of Neuroscience* 32 (39): 13608–20.

Famiglietti, E V, and Helga Kolb. 1976. “Structural Basis for ON and OFF Center Responses in Retinal Ganglion Cells.” *Science* 194 (4261): 193–95.

Foster, R G, I Provencio, D Hudson, S Fiske, W De Grip, and M Menaker. 1991. “Circadian Photoreception in the Retinally Degenerate Mouse (Rd/rd).” *Journal of Comparative Physiology. A, Sensory, Neural, and Behavioral Physiology* 169 (1): 39–50.

Freedman, M. S. 1999. “Regulation of Mammalian Circadian Behavior by Non-Rod, Non-Cone, Ocular Photoreceptors.” *Science* 284 (5413): 502–4.

Ghosh, Krishna K, Sascha Bujan, Silke Haverkamp, Andreas Feigenspan, and Heinz Wässle. 2004. “Types of Bipolar Cells in the Mouse Retina.” *The Journal of Comparative Neurology* 469 (1): 70–82.

Gooley, Joshua J, Jun Lu, Dietmar Fischer, and Clifford B Saper. 2003. “A Broad Role for Melanopsin in Nonvisual Photoreception.” *The Journal of Neuroscience : The Official Journal of the Society for Neuroscience* 23 (18): 7093–7106.

Güler, Ali D, Jennifer L Ecker, Gurprit S Lall, Shafiqul Haq, Cara M Altimus, Wen Liao, Alun R Barnard, Hugh Cahill, Tudor C Badea, Haiqing Zhao, Mark W. Hankins, David M Berson, Robert J Lucas, King-Wai Yau, and Samer Hattar. 2008. “Melanopsin Cells Are the Principal Conduits for Rod/cone Input to Non-Image Forming Vision.” *Nature* 453 (7191): 102–5.

Hatori, Megumi, Hiep Le, Christopher Vollmers, Sheena Racheal Keding, Nobushige Tanaka, Christian Schmedt, Timothy Jegla, and Satchidananda Panda. 2008. “Inducible Ablation of Melanopsin-Expressing Retinal Ganglion Cells Reveals Their Central Role in Non-Image Forming Visual Responses.” *PLoS ONE* 3 (6): e2451.

Hattar, Samer, H.-W. W Liao, M. Takao, D. M. Berson, and K-W W Yau. 2002. “Melanopsin-Containing Retinal Ganglion Cells: Architecture, Projections, and Intrinsic Photosensitivity.” *Science* 295 (5557): 1065–70.

Hattar, Samer, R J Lucas, N Mrosovsky, S Thompson, R H Douglas, M W Hankins, J Lem, M Biel, F Hofmann, R G Foster, and K -W Yau. 2003. “Melanopsin and Rod-Cone Photoreceptive Systems Account for All Major Accessory Visual Functions in Mice.” *Nature* 424 (6944): 76–81.

Jeon, C J, E Strettoi, and R H Masland. 1998. “The Major Cell Populations of the Mouse Retina.” *The Journal of Neuroscience : The Official Journal of the Society for Neuroscience* 18 (21): 8936–46.

Keeler, Clyde E. 1927. “Iris Movements in Blind Mice.” *American Journal of Physiology* 81 (1): 107–12.

Koike, Chieko, Takehisa Obara, Yoshitsugu Uriu, Tomohiro Numata, Rikako Sanuki, Kentarou Miyata, Toshiyuki Koyasu, Shinji Ueno, Kazuo Funabiki, Akiko Tani, Hiroshi Ueda, Mineo Kondo, Yasuo Mori, Masao Tachibana, and Takahisa Furukawa. 2010. “TRPM1 Is a Component of the Retinal ON Bipolar Cell Transduction Channel in the mGluR6 Cascade.” *Proceedings of the National Academy of Sciences* 107 (1): 332–37.

Kolb, Helga. 1977. “The Organization of the Outer Plexiform Layer in the Retina of the Cat: Electron Microscopic Observations.” *Journal of Neurocytology* 6 (2): 131–53.

Kolb, Helga, and E V Famiglietti. 1974. “Rod and Cone Pathways in the Inner Plexiform Layer of Cat Retina.” *Science* 168 (4158): 47–49.

Kolb, Helga, and Jill J. Jones. 1984. “Synaptic Organization of the Outer Plexiform Layer of the Turtle Retina: An Electron Microscope Study of Serial Sections.” *Journal of Neurocytology* 13 (4): 567–91.

Kolb, Helga, Ralph Nelson, and Andrew Mariani. 1981. “Amacrine Cells, Bipolar Cells and Ganglion Cells of the Cat Retina: A Golgi Study.” *Vision Research* 21 (7): 1081–1114.

Kong, Jee-Hyun, Daniel R Fish, Rebecca L Rockhill, and Richard H Masland. 2005. “Diversity of Ganglion Cells in the Mouse Retina: Unsupervised Morphological Classification and Its Limits.” *The Journal of Comparative Neurology* 489 (3): 293–310.

Lehman, Michael N., Rae Silver, W. R. Gladstone, Robert M. Kahn, Marie Gibson, and Eric L Bittman. 1987. “Circadian Rhythmicity Restored by Neural Transplant. Lmmunocytochemical Characterization of the Graft and Its Integration with the Host Brain.” *The Journal of Neuroscience* 7 (June): 1626–38.

Li, Wei, Shan Chen, and Steven H DeVries. 2010. “A Fast Rod Photoreceptor Signaling Pathway in the Mammalian Retina.” *Nature Neuroscience* 13 (4). Nature Publishing Group: 414–16.

MacNeil, Margaret A., and Richard H. Masland. 1998. “Extreme Diversity among Amacrine Cells: Implications for Function.” *Neuron* 20 (5): 971–82.

Masland, Richard H. 2012. “The Neuronal Organization of the Retina.” *Neuron* 76 (2). Elsevier Inc.: 266–80.

Menger, Nicole, David V Pow, and Heinz Wassle. 1998. “Glycinergic Amacrine Cells of the Rat Retina.” *Journal Comparative Neurology* 401 (1): 34–46.

Mills, Stephen L, and Stephen C Massey. 1994. “Distribution and Coverage of A- and B-Type Horizontal Cells Stained with Neurobiotin in the Rabbit Retina.” *Visual Neuroscience* 11 (May). Access paid by the UCSD Libraries: 549–60.

Moore, Robert Y, and Victor B Eichler. 1972. “Loss of a Circadian Adrenal Corticosterone Rhythm Following Suprachiasmatic Lesions in the Rat.” *Brain Research* 42 (1): 201–6.

Nakajima, Y., H. Iwakabe, C. Akazawa, H. Nawa, R. Shigemoto, N. Mizuno, and S. Nakanishi. 1993. “Molecular Characterization of a Novel Retinal Metabotropic Glutamate Receptor mGluR6 with a High Agonist Selectivity for L-2-Amino-4-Phosphonobutyrate.” *The Journal of Biological Chemistry* 268 (16): 11868–73.

Nomura, Akinori, Ryuichi Shigemoto, Yasuhisa Nakamura, Naoyuki Okamoto, Noboru Mizuno, and Shigetada Nakanishi. 1994. “Developmentally Regulated Postsynaptic Localization of a Metabotropic Glutamate Receptor in Rat Rod Bipolar Cells.” *Cell* 77 (3): 361–69.

Østergaard, Jens, Jens Hannibal, and Jan Fahrenkrug. 2007. “Synaptic Contact between Melanopsin-Containing Retinal Ganglion Cells and Rod Bipolar Cells.” *Investigative Ophthalmology and Visual Science* 48 (8): 3812–20.

Panda, Satchidananda, Surendra K Nayak, Brice Campo, John R Walker, John B Hogenesch, and Tim Jegla. 2005. “Illumination of the Melanopsin Signaling Pathway.” *Science (New York, N.Y.)* 307 (5709): 600–604.

Panda, Satchidananda, Ignacio Provencio, Daniel C Tu, Susana S Pires, Mark D Rollag, Ana Maria Castrucci, Mathew T Pletcher, Trey K Sato, Tim Wiltshire, Mary Andahazy, Steve A Kay, Russell N Van Gelder, John B Hogenesch. 2003. “Melanopsin Is Required for Non-Image-Forming Photic Responses in Blind Mice.” *Science* 301: 525–27.

Panda, Satchidananda, Trey K Sato, Ana Maria Castrucci, Mark D Rollag, Willem J De Grip, John B Hogenesch, Ignacio Provencio, and Steve A. Kay. 2002. “Melanopsin (Opn4) Requirement for Normal Light-Induced Circadian Phase Shifting.” *Science* 298 (5601): 2213–16.

Pourcho, Roberta G., and Dennis J. Goebel. 1983. “Neuronal Subpopulations in

Cat Retina Which Accumulate the GABA Agonist, (3H)muscimol: A Combined Golgi and Autoradiographic Study." *Journal of Comparative Neurology* 219 (1): 25–35.

Provencio, Ignacio, Howard M Cooper, and Russell G Foster. 1998. "Retinal Projections in Mice with Inherited Retinal Degeneration: Implications for Circadian Photoentrainment." *The Journal of Comparative Neurology* 395 (4): 417–39.

Provencio, Ignacio, Guisen Jiang, William J De Grip, William Par Hayes, and Mark D Rollag. 1998. "Melanopsin: An Opsin in Melanophores, Brain, and Eye." *Proceedings of the National Academy of Sciences of the United States of America* 95 (1): 340–45.

Provencio, Ignacio, Ignacio R Rodriguez, Guisen Jiang, William Par Hayes, Ernesto F Moreira, and Mark D Rollag. 2000. "A Novel Human Opsin in the Inner Retina." *The Journal of Neuroscience* 20 (2): 600–605.

Provencio, Ignacio, Mark D Rollag, and Ana Maria Castrucci. 2002. "Photoreceptive Net in the Mammalian Retina. This Mesh of Cells May Explain How Some Blind Mice Can Still Tell Day from Night." *Nature* 415: 493.

Ralph, M R, R G Foster, F C Davis, and M Menaker. 1990. "Transplanted Suprachiasmatic Nucleus Determines Circadian Period." *Science (New York, N.Y.)* 247 (4945): 975–78.

Raviola, Elio, and Norton B Gilula. 1973. "Gap Junctions Between Photoreceptor Cells in the Vertebrate Retina." *Proceedings of the National Academy of Sciences* 70 (6): 1677–81.

Schmidt, Tiffany M., Shih-Kuo Chen, and Samer Hattar. 2011. "Intrinsically Photosensitive Retinal Ganglion Cells: Many Subtypes, Diverse Functions." *Trends in Neurosciences* 34 (11). Elsevier Ltd: 572–80.

Schmidt, Tiffany M, and Paulo Kofuji. 2009. "Functional and Morphological Differences among Intrinsically Photosensitive Retinal Ganglion Cells." *Journal of Neuroscience* 29 (2): 476–82.

Schmidt, Tiffany M, and Paulo Kofuji. 2011. "Structure and Function of Bistratified Intrinsically Photosensitive Retinal Ganglion Cells in the Mouse." *The Journal of Comparative Neurology* 519 (8): 1492–1504.

Stephan, F K, and I Zucker. 1972. "Circadian Rhythms in Drinking Behavior and Locomotor Activity of Rats Are Eliminated by Hypothalamic Lesions." *Proceedings of the National Academy of Sciences of the United States of*

America 69 (6): 1583–86.

Tu, Daniel C., Dongyang Zhang, Jay Demas, Elon B. Slutsky, Ignacio Provencio, Timothy E. Holy, and Russell N. Van Gelder. 2005. “Physiologic Diversity and Development of Intrinsically Photosensitive Retinal Ganglion Cells.” *Neuron* 48 (6): 987–99.

Viney, Tim James, Kamill Balint, Daniel Hillier, Sandra Siegert, Zsolt Boldogkoi, Lynn W Enquist, Markus Meister, Constance L Cepko, and Botond Roska. 2007. “Local Retinal Circuits of Melanopsin-Containing Ganglion Cells Identified by Transsynaptic Viral Tracing.” *Current Biology : CB* 17 (11): 981–88.

Volgyi, Bela, Samir Chheda, and Stewart A. Bloomfield. 2009. “Tracer Coupling Patterns of the Ganglion Cell Subtypes in the Mouse Retina.” *Journal of Comparative Neurology* 512 (5): 664–87.

Werblin, Frank S, and John E Dowling. 1969. “Organization of the Retina of the Mudpuppy, Necturus Maculosus. II. Intracellular Recording.” *Journal of Neurophysiology* 32 (3): 339–55.

Wiegand, Staley J., and Ei Terasawa. 1982. “Discrete Lesions Reveal Functional Heterogeneity of Suprachiasmatic Structures in Regulation of Gonadotropin Secretion in the Female Rat.” *Neuroendocrinology* 34 (6): 395–404.

Chapter 2

Ultrastructure of the mRGC Terminal

2.1 Abstract

Melanopsin-expressing retinal ganglion cells (mRGCs) are intrinsically photosensitive retinal ganglion cells that are absolutely essential for non-image forming (NIF) visual processes such as circadian photoentrainment and pupillary light reflex. mRGCs mediate these processes by sending long axons to the physically distinct regions of the brain such as the suprachiasmatic nucleus (SCN), olivary pretectal nucleus (OPN), and intergeniculate leaflet (IGL) that mediate these functions. Circadian photoentrainment, mediated by the SCN and modulated by the IGL, requires minutes to hours of light stimulation to effect a change and pupillary light reflex, mediated by the OPN, operates on the order of milliseconds. mRGCs have also been shown to send axonal projections to the lateral geniculate nucleus (LGN), an area of the brain known to be important for image forming vision. How mRGCs interact with cells in the different target regions to mediate these temporally distinct processes is unknown. Using a novel correlated light and electron microscopy label, mini-Singlet Oxygen Generator (miniSOG), and serial blockface scanning electron microscopy, we generated large volumes of SCN, OPN, IGL, and LGN with labeled mRGC axons. Through manual and automatic segmentation of these volumes we find differences in synaptic bouton size, density, and ultrastructure between mRGC axon terminals in the different mRGC-target regions.

2.2 Introduction

Intrinsically photosensitive retinal ganglion cells (mRGCs) express the photopigment melanopsin (*Opn4*) and are essential for non-image forming visual processes. In response to light, mRGCs fire tonically through the entire duration of light exposure (Berson, Dunn, and Takao 2002; Zhao et al. 2014) and relay rod/cone-initiated light responses (Panda et al. 2002; Güler et al. 2008; Hatori et al. 2008) through long-range axonal projections to numerous anatomically distinct brain centers (Ecker et al. 2010). For example, in the mouse, light information travels ~10 mm through mRGC axons to the suprachiasmatic nucleus (SCN) to facilitate circadian photoentrainment and ~15 mm to reach the olivary pretectal nucleus (OPN) to mediate pupillary constriction in response to bright lights (also known as the pupillary light reflex (PLR)). The length of light exposure necessary to effect changes in photoentrainment is on the order of hours, whereas the length of light exposure to evoke PLR is on the order of milliseconds and seconds. How one genetically-defined cell type facilitates such temporally and spatially diverse functions remains unknown.

M1 mRGCs are morphologically distinct, are the only mRGCs that monostratify in the OFF-sublamina of the IPL, and are known to send axon projections to the SCN, intergeniculate leaflet (IGL), ventral lateral geniculate nucleus (vLGN) and shell of the OPN (Hattar et al. 2002). However, non-M1 mRGCs, in addition the M1 targets, will also send axons to the core of the OPN, the superior colliculus (SC) and the dorsal lateral geniculate nucleus (dLGN). Since all past studies have depended on a transgenic mouse line that happens

to only mark M1s (Hattar et al. 2002), transgenic mouse lines that mark all mRGC subtypes indiscriminately (Hatori et al. 2008), and potentially leaky or mistargeted retrograde labeling (Baver et al. 2008; Estevez et al. 2012) there is a need for an unbiased approach to investigating whether mRGC-subtypes send axons to specific central targets. By understanding the structure of mRGCs, we can hope to understand connectivity and function. Resolving ultrastructural differences in mRGC interactions with mRGC-recipient brain regions would add heft to the idea of mRGC subtype-specific facilitation of NIF visual processes. However, the ability to visualize mRGC synaptic structure in mRGC-target brain regions have been hindered by the facts that 1) melanopsin is variably expressed between mRGC subtypes (Ecker et al. 2010), 2) melanopsin is not expressed beyond the optic disc (Hattar et al. 2002), 3) light microscopy and immunhistochemical approaches do not afford enough resolution to identify definitive synaptic structure. Ultimately, in order to explore the structure-function relationships of mRGCs in the brain, a new technique is needed that allows for labeling all mRGC processes in the retina and brain in a way that is amenable to directed electron microscopy studies.

Mapping synaptic connections between neurons is essential to understanding the neuronal circuits that facilitate the flow and processing of information in the brain. However, the ability to resolve a complete circuit is hindered by the necessity to process large tissue volumes and by the resolution that can be achieved with available microscopy techniques. Serial block-face scanning electron microscopy provides the ultrastructural resolution necessary to

visualize and assess single synapses and the ability to automate the collection of serial sections of large volumes of tissue (Denk and Horstmann 2004) but is currently limited by the inability to genetically label specific cell types for use with EM and by the time needed to annotate the large amount of data generated. To investigate the potential differences that facilitate the differential timing of mRGC-mediated functions we expressed a correlated light and electron microscopy label in mRGCs in the mouse retina and optimized an EM pipeline to label and resolve mRGCs and their processes in the retina and mRGC-recipient brain regions with serial blockface scanning electron microscopy (SBEM). Furthermore, we streamlined image processing and analysis pipelines to quantify the structure of mRGC synapses in central target regions in search of differences in quantity, ultrastructure, and complexity of mRGC synaptic boutons in the major mRGC target brain regions.

While many super resolution light microscopy techniques are pushing the limits of light microscopy resolution to the order of tens of nanometers (Huang, Bates, and Zhuang 2009), these techniques require structures to be labeled by fluorescent probes- meaning that without melanopsin expression in the brain, one would be unable to label mRGC terminals. Also, while it would be feasible to use viral techniques to express fluorescent protein in the mRGCs from the retina, these techniques do not allow for the visualization of non-labeled structures. Since we do not know the unique molecular signatures of the downstream cells in the various brain regions, we would be unable to explore those connections in an unbiased manner. Unfortunately, most electron microscopy techniques are

also not amenable to our goals either. The inability to stain for melanopsin and the fact that mRGC axons make up less than 4% of retinal axons leaving the eye makes the probability of chancing upon mRGC axon terminals in electron microscopy (EM) images of the mRGC-recipient brain regions very low and being able to recognize them as mRGC axon terminals very unlikely. Past studies of mRGCs using electron microscopy have focused on mRGC connections in the retina, where the melanopsin-expression allows for immuno-EM. To date, there are no studies exploring the ultrastructure of mRGC axon terminals in the brain.

Correlated light and electron microscopy (CLEM) is a technique where the same specimen can be imaged with both light and electron microscopy. Light microscopy would allow for the antibody-labeling of the specimen as well as the localization of sparse signals prior to sinking the time into processing and imaging specimens with electron microcopy and electron microscopy would allow for the exploration of ultrastructure and neighboring unlabeled interactors. This sort of multiscale multimodal approach is invaluable to nascent studies involving a morphologically defined cell type and its unknown pre- and post-synaptic partners.

One such CLEM label is mini-Singlet Oxygen Generator (miniSOG). MIniSOG is derived from a 106-amino acid green fluorescent flavoprotein derived from *Arabidopsis* phototropin2 which is particularly useful for CLEM purposes because it releases singlet oxygen when exposed to blue light (Shu et al. 2011). Its small size allows for miniSOG to be fused to many different proteins such that the proteins can still function. In processing specimens with miniSOG labels for

EM, illuminating the specimen with blue light in the presence of DAB causes the released singlet oxygens to very locally polymerize DAB into an electron-dense product that can be stained with osmium tetroxide for use in EM. Also, because singlet oxygen generation is dependent on light exposure and because all players involved are small molecules, thicker slices of tissue can be used since penetrance is less of an issue.

To explore the ultrastructure of mRGC axons in different mRGC-recipient brain regions we used a vector-mediated approach to express miniSOG in all mRGCs in the mouse eye. By photooxidizing tissue specimens that were positive for miniSOG fluorescence to generate an electron-dense precipitate and processing this tissue for subsequent serial blockface scanning electron microscopy (SBEM), large volumes of mRGC-recipient brain regions with easily recognizable mRGC axonal processes were obtained. Consistent with the idea that different mRGC subtypes were sending axons to the five different mRGC-recipient regions, we found significant differences in bouton volume, number of mitochondria, post-synaptic interactions, and axon caliber between mRGCs found in different brain regions.

2.3 Materials and Methods

Animals

Male and female *Opn4*$^{Cre/+}$ mice between 8 wks and 6 months were used.

Vector construction

A farnesyl sequence was cloned into the 3' end of the miniSOG construct and was inserted in an inverted orientation between the lox sites in an AAV2-DIO vector to create AAV2-DIO-miniSOG-f. AAV2-DIO-miniSOG-f and AAV2-DIO-tdTomato-f was produced by the Salk Gene Transfer, Targeting and Therapeutics Viral Vector Core Facility at titers of 1.09×10^{11} TU/ml and 9.41×10^{11} TU/ml, respectively.

Intravitreal injection

To express miniSOG and tdTomato mRGCs, 3 ul of AAV2-EF1α-DIO-miniSOGm and 0.3 ul of AAV2-EF1α-DIO-tdTomato was injected into each eye of *Opn4*$^{Cre/+}$ mice between the ages of 8 weeks and 6 months old. Anesthesia is induced and maintained with isoflurane. 0.5% proparacaine (Bausch and Lomb) was applied to each eye prior to any surgical procedure to provide topical analgesia. The mouse was placed on the stage of a dissection microscope such that the left eye was completely visible in the viewfinder. Curved forceps were used to place gentle pressure around the eye such that the globus of the eye raised slightly out of the orbit and the edge of the sclera was visible. A small incision was made with a 31-gauge insulin needle 0.5 mm posterior to the limbus of the eye (the region where the sclera meets the cornea). Virus was loaded into a Hamilton microliter syringe with a 34-gauge beveled needle mounted on a micromanipulator. Using the micromanipulator, the needle was maneuvered through the incision made by the insulin needle until the tip of the needle was in the middle of eye. Virus was slowly injected over the course of 1 minute and allowed to diffuse through the vitreous for 3 minutes before the needle was slowly

withdrawn. The whole procedure was then repeated on the right side. After both eyes have been injected, GenTeal lubricant eye gel (Novartis) was applied to both eyes and the animal removed from isoflurane anesthesia and placed in a clean cage to recover. When righting reflex was restored after 1-2 minutes, the animal was returned to its home cage.

Circadian wheel running

The daily locomotor activity of mice intravitreally injected with AAV2-EF1α-DIO-miniSOG-f and AAV2-EF1α-DIO-tdTomato, a different GFP expressing AAV2-DIO vector, and age matched uninjected mice was measured following methodology established in Siepka and Takahashi, 2005. Briefly, mice were individually housed in cages with *ad libitum* access to standard mouse chow and a running wheel connected to a counter that reported wheel rotations to a computer. All cages were kept within one ventilated and independently lit light tight box in the vivarium. During the light phase, which began at 6AM and ended at 6PM PST, the mice received ~150 lux white light from a fluorescent light source. Wheel running activity, as number of rotations, was continuously collected as 5 min bins and later analyzed by ClockLab software (Actimetrics, evanston, IL, USA). After 11 days on a strict 12:12 light dark cycle, the lighting conditions were changed to complete darkness for 7 days before resuming the original 12:12 light:dark conditions. All routine animal husbandry care that occurred during the dark phase was performed under dim red light illumination so as not to disrupt circadian light entrainment.

Immunohistochemistry and confocal microscopy imaging

For immunofluorescence labeling, miniSOG and tdTomato traced 100 um thick brain and retina sections were blocked in 10% normal donkey serum (NDS, Jackson ImmunoResearch, West Grove, PA, USA) in PBS for 1 h at room temperature prior to incubation with the following antibodies: Rabbit polyclonal anti-MiniSOG antibody (1:500; Custom order from QED Biosciences, San Diego, CA, USA) and mouse monoclonal anti-Caspr antibody (1:1,000; Neuromab, Davis, CA, USA), in 10% NDS for 16 h at 4 °C. Fluorescence-conjugated secondary antibodies were applied at 1:100 dilution for 4 h at 4 °C and then washed with PBS. For myelin staining, the sections were stained with FluoroMyelin (Invitrogen, Carlsbad, CA, USA). Images were acquired with confocal microscopy (Olympus FluoView1000; Olympus, Tokyo, Japan).

Tissue preparation for SBEM

At least three weeks after intravitreal injection of AAV-miniSOG into *Opn4*^{Cre} mice, the mice were anesthetized with ketamine/xylazine and transcardially perfused with Tyrode's solution followed by 4% formaldehyde/ 0.1% glutaraldehyde in 0.1M phosphate buffered saline (PBS). The retina and brain were dissected and post-fixed with 4% formaldehyde in 0.1 M PBS on ice for 2h and then brain was cut into 100-µm-thick slices. For mini singlet oxygen generator protein (miniSOG) photooxidation, tdTomato-expressing mRGCs and mRGC axons were identified using a Leica SPE II inverted confocal microscope and the retina and brain tissue were fixed with 2.5% glutaraldehyde, 2.5 mM CaCl2 in 0.15 M Sodium Cacodylate buffer (CB) pH 7.4, and the tissue was rinsed with ice cold CB, and blocked for 30 min with 50 mM glycine, 10 mM Potassium

cyanide and 5 mM aminotriazole in CB. Freshly prepared diaminobenzidine (DAB free base, Sigma) in CB was added to the tissue, and mRGCs and axons were illuminated with 450–490 nm light from a Xenon lamp for 20–25 min until a light brown reaction product was observed in place of the green fluorescence of miniSOG. The tissue was then processed for SBEM.

SBEM staining and imaging

Tissue was prepared for SBEM as previously described (Deerinck et al. 2010). Briefly, tissue was washed with 0.15 M CB and then placed into 2% OsO4/1.5% potassium ferrocyanide in 0.15 M CB containing 2 mM CaCl2. The slices were left for 30 min on ice and then 30 min at room temperature (RT). After thorough washing in double distilled water, the slices were placed into 0.05% thiocarbohydrazide for 30 min. The slices were again washed and then stained with 2% aqueous OsO4 for 30 min. The slices were washed and then placed into 2% aqueous uranyl acetate overnight at 4°C. The slices were washed with water at RT and then stained with en bloc lead aspartate for 30 min at 60°C. The slices were washed with water and then dehydrated on ice in 50%, 70%, 90%, 100%, 100% ethanol solutions for 10 min at each step. The slices were then washed twice in dry acetone and then placed into 50:50 Durcupan ACM:acetone overnight. The slices were transferred to 100% Durcupan resin overnight. The slices were then flat embedded between glass slides coated with mould-release compound and left in an oven at 60°C for 72 h. SBEM data was collected with a 3View unit (Gatan Inc., Pleasanton, CA, USA) installed on a Merlin field emission SEM (Carl Zeiss Microscopy, Jena, Germany). The retina and brain volumes

were collected in 2.0 to 2.4 kV accelerating voltages, with a raster size of 20k×20k or 24kx24k and pixel dwell time of 0.5 -1.5 µs. The pixel sizes were 4.0-7.3 nm, depending on the raster size and section thickness was 60-70 nm. Before each volume was collected, a low magnification (~500×) image was collected of the block face to confirm the anatomical location of the volume based on tissue landmarks, such as the RGC, SCN, and the OPN. Once a volume was collected, the histograms for the slices throughout the volume stack were normalized to correct for drift in image intensity during acquisition. Digital micrograph files (.dm4) were normalized using Digital Micrograph and then converted to MRC format. The stacks were converted to eight bit, mosaics were stitched, and volumes were manually or semi automatedly traced for reconstruction and analysis.

Electron microscope tomography

Electron tomography specimens from the SCN and OPN were sectioned with a diamond knife at a thickness of 300 nm. Following glow discharge, 15-nm diameter colloidal gold particles were deposited on each side to serve as fiducial markers. Data were generated with an FEI Titan microscope operating at 300 kV; the micrographs were produced using a 4k × 4k Gatan CCD camera. For reconstruction, double tilt series of images were recorded between −60° and +60° at regular increments of 0.5°. Fine alignment of projections and 3D reconstruction were done using the transform-based tracking, bundle adjustment, and reconstruction package in conjunction with IMOD.

Manual segmentation

3D reconstruction of SCN and OPN neurons. In order to maximize the amount of reconstructed neuronal processes from each neuron traced in the SCN and OPN, neurons were selected from the center of each image in IMOD (University of Colorado, Boulder). Each individual neuron of interest was traced as a separate object by drawing contours around the plasma membrane of each selected cell as it moved through each slice of the image. Individual contours were meshed with *imodmesh* to reveal three-dimensional reconstructions of the neurons of interest. In this way, cell bodies, axons, dendrites, and, in some cases, primary cilia, were identified and represented in the 3D model.

Grid-Based Selection Scheme- All boutons were sampled from the 100 intersection points of an 11X11 grid overlaid on the image stack. Panning down through the image stack, the first labeled bouton to intersect with the grid point, or the closest bouton to it, was sampled. Subsequently, these boutons were backtraced to the limit of the volume to yield a segment of axon and more boutons. This allowed for a comprehensive and unbiased sampling of the tissue.

Synapse quantification. Putative synapses were identified manually by finding areas of the axon that were swelled to diameters at least twice as large as the average diameter of axons. A swelling was deemed a putative synapse if it fulfilled at least two of the following three criteria: presence of a post-synaptic density in the directly apposed membrane, presence of at least one mitochondria, or evidence of synaptic vesicles less than one vesicle diameter's distance from the plasma membrane. In order to count the number of synaptic boutons, each image volume was parsed into a 10 x 10 grid and the miniSOG-labeled boutons

in every other square column was counted. The contours that make up each bouton were traced out and meshed with *imodmesh* to determine bouton volume, and the mitochondria and intrusions from the post-synaptic process into the bouton were counted.

Axon volume. MiniSOG-labeled mRGC axonal processes were identified by the dark miniSOG label and the outlines of the cross section of miniSOG-labeled axon was traced to make contours of the axon in each slice of the image volume. Each individual axon was assigned a unique object number that consisted of all axon contours. Contours were meshed with *imodmesh* to render three-dimensional reconstructions of each axon. The IMOD program *imodinfo* returned the volume of the object.

***Axon length*.** A new open contour object was made for each axon and individual consecutive points of a single open contour were placed in the center of miniSOG-labeled axon cross-sections starting from the first slice in a image volume until the last slice in an image volume. If an axon branched, a new open contour was made for that axon object and another set of consecutive points laid down for the branch. This was repeated until the entire axon was represented by an open contour skeleton line created from consecutive points. *Imodinfo* returned the length of all lines in the object.

Automatic Segmentation

Generation of Ground Truth Data. A 5,000 x 5,000 x 100 voxel sub-volume of the full SBEM dataset was extracted to yield a set of ground truth images. All miniSOG-stained mRGC axons contained within this set were

manually segmented to provide ground truth labels, and the accuracy of these labels was verified independently by two experts. Following observation of the ground truth labels, three classes of mRGC axons were qualitatively identified within the SBEM volume based upon the strength and variation of voxel intensity levels across image planes. In the first class of Densely Stained (DS) axons, the staining was consistently dark throughout all cross-sectional planes of the axon, resulting in low voxel intensity values and low inter-plane variances. For the second class of Sparsely Stained (SS) axons, the staining was consistently light throughout the cross-sectional planes of the axon. The final class, Variably Stained (VS) axons, exhibited staining that was inconsistent, with some regions of dense staining and some regions of sparse staining. The 96 individual axon segments contained within the ground truth labels were automatically classified into one of these three groups via k-means clustering (k = 3) of the mean voxel intensity of the entire axon segment and the range of the mean voxel intensities for all cross-sectional planes.

Cascaded Hierarchical Model Training. A 500 x 500 x 50 set of training images and labels for the DS axon class was generated via manual segmentation. The training images consisted of tiles interspersed throughout the breadth and depth of the full SBEM volume, and decisions on whether each cross-sectional axon profile encountered belonged to the DS class were made qualitatively. The same process was then repeated to yield an equally sized set of training images and labels for the SS axon class. Unique voxel classifiers were trained for the DS and SS classes using the cascaded hierarchical model (CHM)

with two stages and two levels (Seyedhosseini, Sajjadi, and Tasdizen 2013). All CHM processes were run on the SQUIRE web portal (http://cellsegmentation.org).

Semi-automatic Axon Segmentation. Each trained voxel classifier was applied to the full SBEM stack to yield two sets of probability maps, one for DS axons and one for SS axons. All probability maps were segmented by evolving 2D active contours from automatically seeded initial positions, as previously described (Perez et al. 2014). A number of post-processing steps were than performed to enhance segmentation accuracy. A final, combined segmentation stack was generated by taking the voxel-by-voxel logical disjunction of the DS and SS segmentation stacks and running a hole filling operation on the output. Three-dimensionally connected components were computed across the entire segmentation volume using the IMOD (Kremer, Mastronarde, and McIntosh 1996) programs *imodauto* and *imodsortsurf*. The output connected components were then morphologically filtered using the PyImod set of Python modules for manipulating IMOD binary model files (https://github.com/alexjperez/pyimod). Two rounds of filtering were performed; first, components with any cross-sectional area greater than 6 μm^2 were removed to reduce the occurrence of common false positives such as non-labeled myelin sheaths and regions of charging within cell nuclei and blood vessels. Second, components that did not persist across the depth of the stack for greater than 2 μm were removed to reduce the prevalence of common false positives such as densely stained lysosomes. Surface renderings of the filtered results were produced using

imodmesh, converted to the VRML format, and displayed in Amira (FEI Company, Hillsboro, OR).

Segmentation quality was assessed by comparison of the final results to the manually generated ground truth labels over the 5,000 x 5,000 x 100 voxel ground truth sub-volume.

The semi-automated segmentation workflow yielded an F-value of 0.66537 over the region of ground truth tested. By comparison, the same workflow applied to only the results from the DS axon segmentation produced an F-value of 0.51479. Therefore, as expected, the process of training separate DS and SS axon models and combining their results via logical disjunction dramatically improved final segmentation quality. Seventy-eight percent of the axon segments within the ground truth volume that persisted for more than a few sections were at least partially annotated in the final segmentation.

2.4 Results

2.4.1 Vector-mediated expression of miniSOG in mRGCs

To target the *in vivo* expression of miniSOG to mRGCs we genetically engineered an adeno-associated viral vector, AAV-EF1a-DIO-miniSOG-f, which expresses a c-terminus farnesyl-tagged miniSOG EM reporter in the presence of Cre-recombinase and intravitreally co-injected the AAV2.2 serotyped EF1-DIO-miniSOG-f (1.01 x 10^{11} GC/ml by qPCR) and EF1-DIO-TdTomato-f (9.43 x 10^{11} GC/ml by qPCR) vectors to both eyes of 6 week old *Opn4*$^{Cre/+}$ mice (Figure 2.1) (as described in Hatori et al., 2008). Expression of reporters in the weeks

following vector transduction did not adversely affect the function of these cells as the mice maintained their circadian rhythm entrained to the ambient light dark cycle, appropriately consolidated their activity to the dark phase, and had circadian period lengths that were not significantly different from control injected and control age-matched non-injected mice in both 12:12 Light:Dark (LD) and 12:12 Dark:Dark (DD) conditions (Figure 2.2). Furthermore, miniSOG was appropriately expressed in Cre-expressing cells as immunostaining of the retina with anti-miniSOG antibody was correlated with expression of Cre-dependent vector-mediated tdTomato in mRGCs in the retina and in brain regions known to receive mRGC inputs (Figure 2.1). Given that mRGCs are sparsely (accounting for less than 4% of all retinal ganglion cells, or <0.1% of all nuclei in the mouse retina) but evenly distributed throughout the retina, the number of mRGCs labeled in a given area of retina is representative of the overall density of mRGCs in the whole retina (Berson, Castrucci, and Provencio 2010). The number of mRGC somas labeled, as identified by light microscopy, was 174+25 mm^{-2} (average + s.d; n=6), which is equivalent to the estimated mRGC density in mouse retina. Hence the strategy comprehensively labels nearly all mRGCs in the *Opn4*$^{Cre/+}$ retina.

2.4.2 Photooxidation of miniSOG reveals label amenable to SBEM

To resolve the ultrastructure of mRGCs and their processes in the retina and brain, tissue from the retina and mRGC target brain regions of AAV-EF1a-DIO-miniSOG-f injected mice were processed for SBEM. SBEM imaging requires

intense staining of biological specimens with heavy metals to allow sufficient back-scatter electron signal and also to render specimens sufficiently conductive to control charging artifacts. These extreme heavy metal staining protocols make it much more difficult to track and identify regions of interest (ROIs) for SBEM imaging process. Because each volume of data requires significant investment of time and resources, the regions of interest (ROI) must be carefully selected. Fluorescent images of miniSOG-labeled tissues were taken prior processing for EM and used to guide ROI selection for SBEM. To process miniSOG-labeled tissues for SBEM, tissues that contained at least one ROI from the retina and 100 um thick coronal sections through mRGC axon-recipient regions including the optic nerve (ON), suprachiasmatic nucleus (SCN), dorsal and ventral lateral geniculate nuclei (dLGN, vLGN), intergeniculate leaflet (IGL) and olivary pretectal nucleus (OPN) were photooxidized in the presence of diaminobenzadine (DAB) under blue light irradiation (450-490 nm) for ~20 minutes until a brown precipitate formed in the mRGC cell bodies and neurites. In response to blue light stimulation, miniSOG releases singlet oxygens which polymerize DAB. In the EM tissue processing-pipeline, polymerized DAB is then stained with osmium tetroxide to form electron-dense precipitates that are resolvable by EM (Figure 2.3).

Horizontal retina sections and optic nerve and brain tissue sections were imaged on a Zeiss Merlin scanning electron microscope (Carl Zeiss Microscopy, Jena, Germany) equipped with a Gatan 3View with a step size of 40 to 60 um. Large-scale montaged images of retina and axon-target regions were collected

and stitched together for reconstructing neural circuitry by SBEM imaging. The membrane-delimited miniSOG delineated the plasma membrane in the mRGC soma as compared to neighboring non-mRGCs. In relatively thinner mRGC neurites in retinal and brain tissue photooxidation often resulted in dense labeling of the membrane and diffusion of the DAB reaction product into the cytosolic space which filled the process with a grey precipitate and facilitated easy identification of the neurites. The interior portion of mitochondria and other membrane-delimited organelles in the neurites were not filled with DAB reaction product. This specific labeling of mRGC somas and processes in the retina and brain of *Opn4*$^{Cre/+}$ mice for use with electron microscopy is the first time that miniSOG has been used as a correlated light and electron microscopy label *in vivo* to label a genetically-defined cell type.

2.4.3 MiniSOG label fills mRGC soma and processes

In the retina, photooxidation of miniSOG-laden mRGC somas and processes densely stained mRGCs with characteristic large cell bodies, wide dendritic fields, and beaded dendrites (Hattar et al. 2002). In total, we identified 11 mRGC cell bodies from 4 total retina volumes that amount to 4,736,509.17 um3 of SBEM data. Comparison of mRGC cell bodies with adjacent RGCs revealed several characteristic features of the mRGCs. As shown earlier in light microscopy, the mRGCs have large somas (15.31 um ± 3.62 um diameter, n=14). The larger somas were accompanied with relatively larger nuclei and elevated numbers of mitochondria in the soma (volume fraction; 16.7 ± 4.21 %, vs.

neighboring cells 12.45 ± 2.63 % n=12) (Figure 2.4). The increased mitochondrial volume in the mRGC soma was also accompanied by increased mitochondria in the dendrites. This periodic mitochondria-filled dendritic swellings correspond to the beads-on-a-string appearance of mRGCs dendrites (Hattar et al. 2002) and might correspond to the COX stained RGCs described earlier (Jen and Ghau 1990). The dendrites of the mRGCs also arborized primarily in the on- or off-sublamina of the IPL allowing easy identification of mRGC subtypes. All mRGC subtypes (M1 through M5) were identified in the 4 total retina volumes (4,736,509.17 um3) processed.

The intrinsic green fluorescence of miniSOG was clearly visible and evenly distributed in the cross section of the proximal optic nerve (ON) (Figure 2.5). MiniSOG-labeled mRGC axons were found to be encased within myelin staining. Co-staining for myelin showed almost all miniSOG-positive axons were myelinated, which was further verified in SBEM images of miniSOG-labeled optic nerve cross section. Conversely, there were many unmyelinated axons within the ON, none of which were labeled with miniSOG, thus suggesting that mRGC axons in the ON are primarily myelinated. mRGC axon thickness (as calculated by finding the diameter of a circle with the same enclosed area as the miniSOG labeled axons) within the ON varied between 113 nm and 1455 nm, with a median of 632 nm. The distribution of axon diameters reflects the bimodal distribution of mRGC soma diameters (Figure 2.4 top left vs. Figure 2.5 G) which correlates with the idea that axon caliber varies with soma size (Williams and Chalupa 1983)

and verifies that we were able to follow axons of the labeled mRGCs as they coursed towards central targets in the brain (Figure 2.5).

miniSOG immunostaining as well as brown photooxidation products were detectable in the primary mRGC target regions of the SCN and OPN which mediate photoentrainment of the circadian rhythm and pupillary light reflex, respectively (Figure 2.3 middle and right). In the SCN, the VIP-expressing neurons, which are presumed to receive light input from the mRGCs, have their soma in the ventromedial SCN and extend their neurites throughout the SCN extending to the dorsal aspect of the SCN (Ibata et al. 1989; Tanaka et al. 1993). However, light induced c-FOS expression in the SCN is first throughout SCN, not just in the ventrolateral aspects (Colwell and Foster 1992). Light microscopy (LM) of genetically-labeled mRGC axons have shown mRGC axons cover most of the SCN with no specific preference for any subregion (Hattar et al. 2006). However, LM cannot be used to separate passing neurites from synaptic contacts which makes it difficult to ascribe where mRGCs make synaptic contacts within the SCN. SBEM image stacks of the dorsomedial SCN showed miniSOG-labeled axons dispersed throughout the image stack, corroborating LM results. Both automatic segmentation followed by manual inspection and manual segmentation were done to volume segment the mRGC axons. Our SBEM volumes of SCN and OPN revealed key features of region-specific mRGC axons and putative synapses that may underlie the diversity of timing observed in mRGC-mediated functions.

2.4.4 mRGC interactions in the OPN and SCN

The dense miniSOG labeling of plasma-membrane and cytoplasm in the axonal processes of mRGCs within the SCN core and the lack of myelination in the SCN facilitated the automatic segmentation of mRGC axon segments in the SCN core region (Figure 2.6). The automatic segmentation algorithm recapitulated at least a portion of 78% of axon segments within a thoroughly manually segmented ground truth volume of SCN. Manual correction of automatically segmented SCN volumes and manual segmentation of all other volumes using the IMOD software (University of Colorado, Boulder) allowed for quantification of mRGC processes and ultrastructure in SBEM volumes of mRGC-recipient brain regions (OPN, IGL, vLGN, and dLGN). In total, we segmented 121 SCN neurons (23 of which were annotated for synapses to the full extent of volume boundaries), 287 miniSOG-labeled mRGC boutons, and 37 axon segments which comprised 3200µm of total miniSOG-labeled axonal length from a 403,556 μm^3 volume of SCN. In the OPN, we segmented and annotated 18 neurons, 284 mRGC boutons, and 25 mRGC axon segments comprising 5400µm of total miniSOG-labeled axon length in a 539,044 μm^3 volume of OPN. 130, 100, and 124 miniSOG-labeled mRGC boutons were segmented from IGL, vLGN, and dLGN respectively.

In comparing the fully segmented cluster of neurons from the center of SCN (n=23) and OPN (n= 18) volumes (Figure 2.7), the total number of mRGC boutons that made putative synaptic contacts with SCN or OPN neurons per 100,000μm^3 in the two regions were similar (SCN 633 ± 73; OPN: 748 ± 102)

even though neurons in the SCN were 2.3 times more densely organized than the OPN (SCN: 60.5; OPN: 26.3 neurons, per 100,000μm³). Consequently, the ratio of mRGC synaptic boutons to neurons is 3 times greater in the OPN than in the SCN. Accordingly, mRGC contacts per 100μm of dendritic length was 3 times greater in the OPN (SCN: 3.3 ± 0.8; OPN: 10.8 ± 1.9) and contacts per soma were 6.5 times greater (SCN: 0.91 ± 0.31; OPN: 5.8 ± 1.6). Although OPN neurons have 3.8 times as many synapses per 1000μm² cell surface area in general (SCN: 47.0 ± 5.3; OPN: 143.7 ± 37.8), in the OPN a larger proportion of these synaptic boutons are from mRGCs (SCN: 7.8% ± 1.4%; OPN: 19.3% ± 2.7%). While all examined OPN neurons had mRGC input, 26% (6 of 23) of SCN neurons had no synaptic contacts with an mRGC axon proximal enough to the cell body to be captured within our sample block (minimum of 25μm of available dendrite).

2.4.5 mRGC boutons in the OPN and SCN

mRGC boutons randomly sampled (Figure 2.8) from throughout the tissue block were 81% larger in the OPN (SCN: 0.53±0.05μm³; OPN: 0.91μm³ ± 0.07μm³) and had more mitochondria per bouton (SCN: 1.21 ± 0.04; OPN: 2.13 ± 0.20). 91% of boutons in the SCN had a single mitochondria compared to only 44% in the OPN. 58% of boutons in the OPN formed deep invaginations that engulfed dendritic spines and glial processes.19% of boutons in the OPN engulfed multiple processes with an average of 1.4 ± 0.2 invaginations per bouton. Terminal boutons were no larger than *en passant* boutons in either

region. Non-labeled boutons in the SCN were larger than their labeled counterparts, 1.04μm³ ± 0.09μm³, and exhibited numerous spine engulfment sites. Non-labeled boutons in the OPN were of comparable size and structure to their labeled counterparts (0.91μm³ ± 0.10μm³) (Figure 2.9).

2.4.6 mRGC axons in the OPN and SCN

Randomly sampled miniSOG-labeled axon segments were longer and more complex in the OPN. This is evident by the total segment length of connected axonal branches within a 500,000μm³ sample space, which was almost 2 times as great in the OPN (SCN: 107.0μm ± 9.2μm; OPN: 197.8μm ± 44.8μm) This allowed for more branch points per axon segment in the OPN (SCN: 2.2 ± 0.5; OPN: 4.3 ± 1.4). The axons in the OPN also had 45% more boutons per 100μm axon length (SCN: 10.8 ± 0.6; OPN: 15.7 ± 0.7). Basal axon diameter, or the diameter in sections of axon with no vesicles or mitochondria, was larger in the OPN (SCN: 182nm ± 1.5nm; OPN: 211nm ± 1.9nm) indicating not only larger boutons but an overall larger axon caliber. Axons in the OPN were often myelinated unlike in the SCN, where no myelinated mRGC axons were observed. The terminal branch length, defined as the distance from a terminal bouton and a branch point, is similar in OPN and SCN (SCN: 8.3μm ± 1.1μm; OPN: 9.6μm ± 1.3μm). However, inter-branch distance, defined as the distance between two branch nodes, is larger in the OPN (SCN: 10.2μm ± 1.6μm; OPN: 15.9μm ± 1.7μm), resulting in a larger overall axonal arbor (Figure 2.10).

2.4.7 mRGC boutons in the LGN

While we were primarily focused on mRGC boutons in the SCN and OPN because of the vast differences in timescale of SCN/OPN-mediated processes, we also analyzed mRGC synaptic boutons in the dLGN, vLGN, and IGL. The IGL plays a role in circadian photoentrainment and is known to receive inputs from mRGCs and to send afferent projections back to the SCN (Hattar et al. 2002; Brown et al. 2010). The dLGN and vLGN are traditionally thought of as areas involved in image-forming vision and are also known to receive mRGC inputs (Brown et al. 2010). The miniSOG-labeled mRGC synaptic boutons in the IGL were, on average, similar in volume (0.99 ± 0.08 μm^3, n=130) compared to those seen in the OPN with bouton density measured at 1076 ± 182 boutons per 100,000μm^3 tissue volume with a ratio of 40.9 boutons per neuron. The increase in IGL bouton volume was independent of differences in mitochondria per bouton and actually in spite of a decrease in spine intrusions (56% of boutons) as compared to mRGC synaptic boutons observed in the OPN. While thought only to send sparse projections to the LGN, miniSOG-labeled mRGC synaptic boutons in the vLGN were yet larger than those seen in the OPN and miniSOG-labeled boutons in the dLGN were larger still than those seen in the vLGN and on average 3 times larger than those seen in the OPN (dLGN: 3.00 ± 0.52 μm^3, n=124; vLGN: 1.51 ±0.17 μm^3, n=100; OPN: 0.91 ± 0.07 μm^3, n=284) (Figure 2.11).

2.5 Discussion

Our miniSOG-mediated technique has allowed us to use EM to follow the axons of a genetically-defined cell type in the retina over many millimeters to its central targets in the mouse brain and to reconcile the differential timing of two different mRGC-mediated functions. By being able to easily identify mRGC axons and boutons in SBEM images of the SCN and OPN, we have discovered differences in the ultrastructure of mRGC axons and boutons in the SCN and OPN that may account for the vastly differential timing of the mRGC-mediated responses in each of those areas. The myelinated mRGC axons conveying light intensity information to the OPN and the large synaptic boutons on the convoluted mRGC axonal processes in the OPN may facilitate the rapid and robust transfer of light information necessary to effect PLR in a matter of milliseconds. In the same vein, the simpler and narrower non-myelinated mRGC axons with smaller *en passant* boutons that innervate the SCN necessarily pass light information slower than the OPN which may explain why mRGC-mediated photoentrainment occurs on the time scale of minutes to hours. We find that the total volume of mRGC processes in the SCN accounts for 0.6% of the total volume of the SCN studied, which is counter to the 14.4% determined from the ALPP light microscopy images of single M1 mRGC projections to the SCN in Fernandez, Chang, Hattar, & Chen, 2016.

The vastly different bouton sizes in the five central mRGC targets in this study add to the evidence that the different non-image forming visual processes are served by specific subtypes of mRGCs. Morgan, et al. (2016) found that the

boutons along stretches of individual RGC axons in the thalamus (as long as 100 um) had similarly sized boutons regardless of which thalamocortical cells they were synapsing with. Furthermore, they found that individual RGC axons were more likely to synapse on postsynaptic processes that displayed specific postsynaptic features. Thus, RGC bouton structure is a defining feature of an RGC type and RGCs appeared to have some role in setting the pre- and postsynaptic structural features associated with its axon terminal. Some evidence of that within our studies lies in the fact that the quantified boutons in the dLGN, a region that is thought to receive input from M4 mRGCs (Estevez et al. 2012)-which have the biggest somas and hence the biggest axon calibers (Williams ansd Chalupa 1983), had the biggest bouton volumes as compared to all other mRGC-recipient regions. Also, the M1 subtype is thought to predominantly send axons to the SCN and OPN shell whereas M2 mRGCs are thought to send more axons to the OPN core (Chen, Badea, and Hattar 2011). The significant differences between mRGC axon caliber, bouton sizes, and flat vs. invaginated synapses between the SCN and OPN may reflect the subtype-specific projections of M1 and M2 mRGCs.

The optimized protocols for vector-mediated expression of miniSOG, miniSOG photooxidation, SBEM image collection, and automated segmentation form a unique pipeline that can be used to efficiently study the connectivity and ultrastructure of genetically-defined cell types. The image volumes collected thus far are a rich and invaluable resource of high-resolution information that have yet to be mined. Future directions will aim to elucidate the ultrastructure of mRGC

axons in other brain regions targeted by mRGCs so as to better understand the circuitry of mRGC-mediated functions; as well as to delve deeper into the retina volumes to answer some long-standing questions regarding mRGC intraretinal interactions.

Chapter 2 is currently being prepared for submission for publication of the material. Kim, Keunyoung; Liu, Cindy Yu Hsin; Rios, Luis; Perez, Alex; Phan, Sebastien; Garcia, Guadalupe C.; Ju, Suyeon; Ellisman, Maya; Ellisman, Mark; Panda, Satchidananda. I am the primary investigator and will be co-first author on this paper with Keunyoung Kim who performed and optimized all of the tissue processing, electron microscopy, and image processing. Luis Rios contributed significant segmentation and quantifiacation. Alex Perez contributed the autosegmentation results. Mark Ellisman and Satchidananda Panda directed and supervised the research.

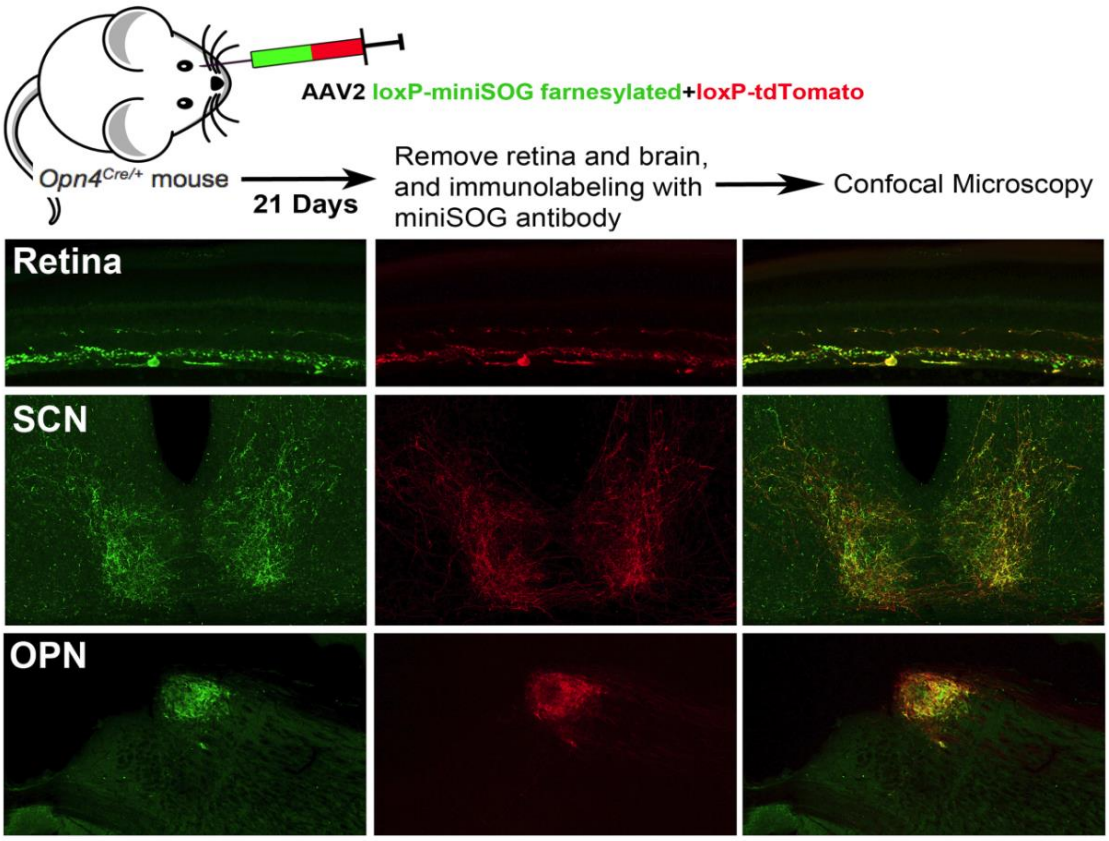

Figure 2.1 Vector-mediated expression of miniSOG in mRGCs

Vector-mediated Cre-dependent expression of miniSOG is localized to mRGCs in Opn4Cre mice. MiniSOG is expressed throughout the mRGC soma, dendrites, and axons.

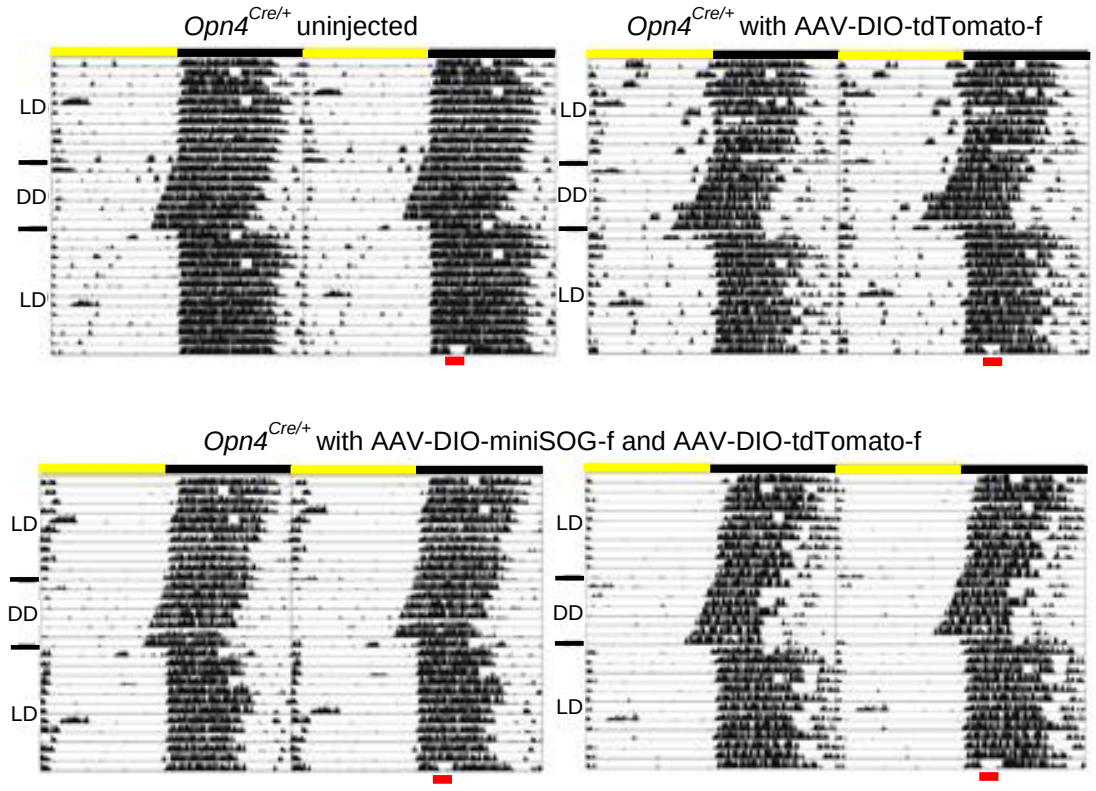

Figure 2.2 Circadian photoentrainment is intact miniSOG-injected mice

Actograms from 3 groups of mice uninjected (top left), injected control DIO construct (top right), and miniSOG-injected (bottom row), showing entrainment of activity rhythms to 12:12 Light:Dark (LD) conditions, normal free-running period in the Dark:Dark (DD) lighting conditions, and intact negative masking to 2 hours bright light stimulus during the early dark period (red bar).

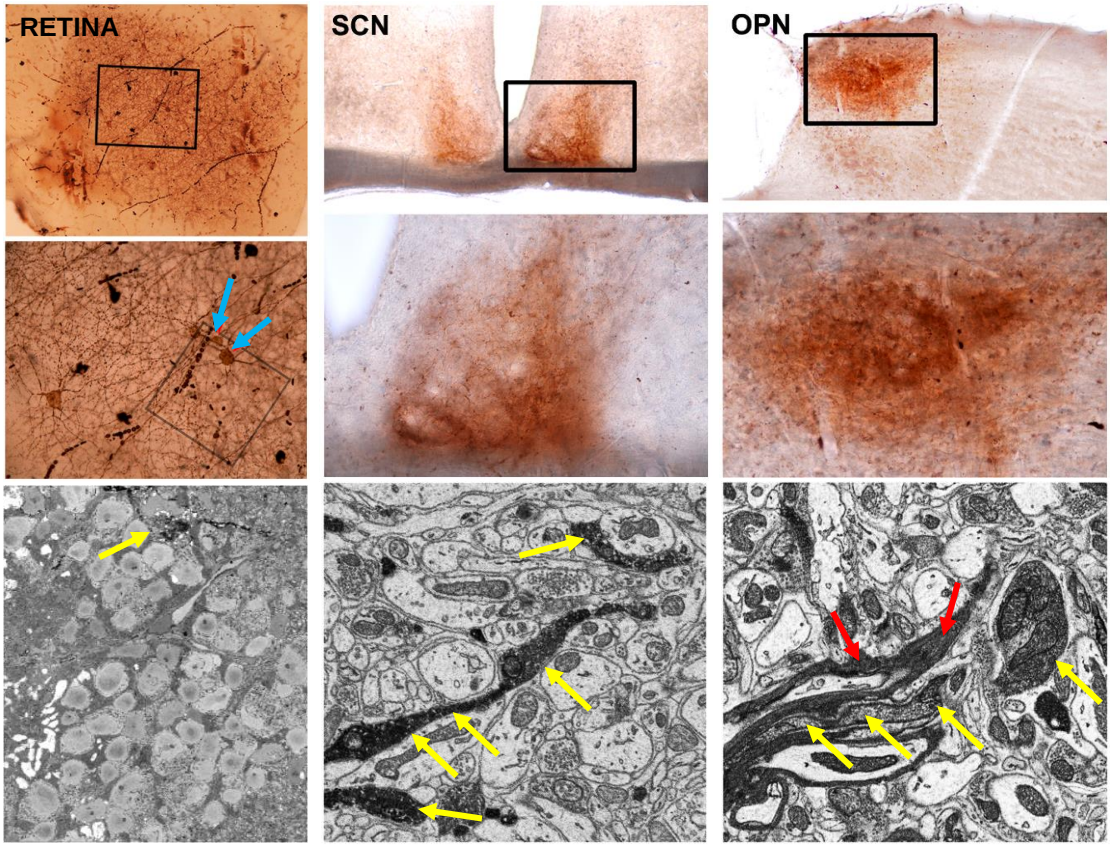

Figure 2.3 Photooxidation of miniSOG-labeled tissues

Photooxidation results in formation of dark brown polymerized DAB product in retina (left), suprachiasmatic nucleus (SCN, middle), and olivary pretectal nucleus (OPN, right). Second row shows the boxed areas in the top row enlarged; in the enlarged view of retina, blue arrows show the miniSOG-labeled mRGCs. Staining the polymerized DAB with osmium tetroxide results in a dark electron-dense precipitate (yellow arrows) that is easily identifiable in EM (bottom row). EM images of OPN reveal that mRGC axonal processes are myelinated (red arrows).

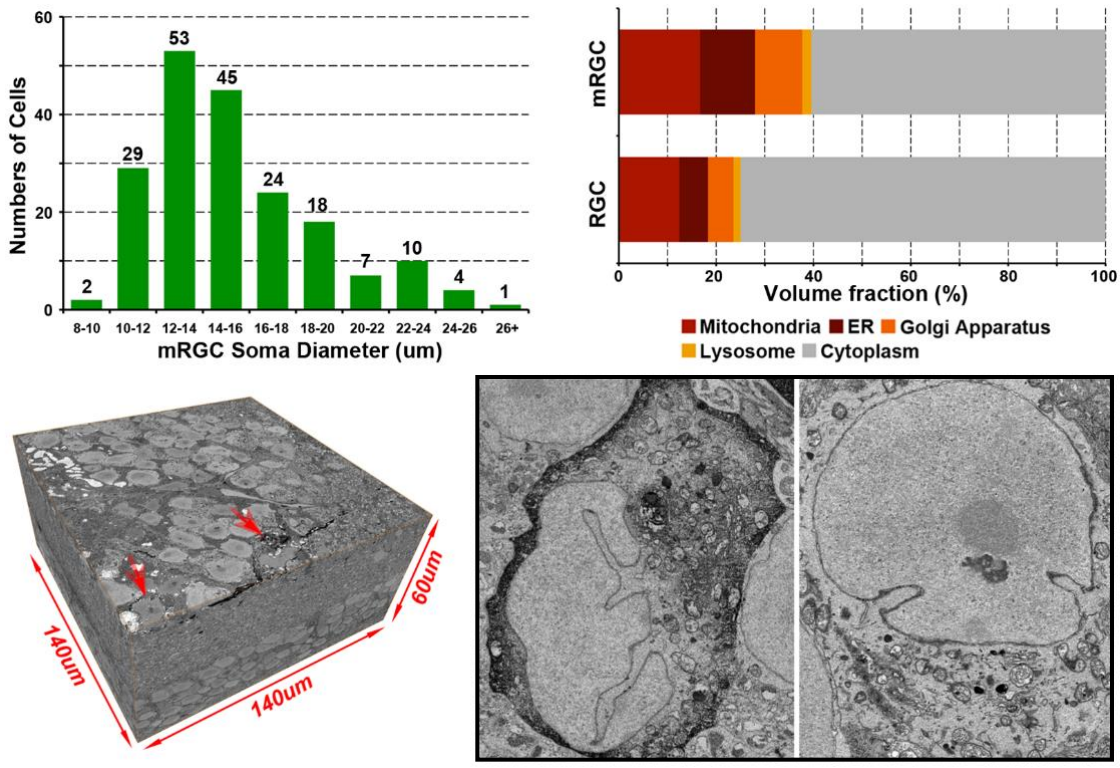

Figure 2.4 MiniSOG label fills mRGC soma

MiniSOG labels mRGCs with soma diameters that are within the ranges of those reported in literature (top left). EM resolution with miniSOG label allows for the calculation of volume fraction occupied by various organelles in mRGCs vs other RGCs (top right). A representative image of a volume of retina tissue (bottom left). A representative image of a miniSOG-labeled mRGC (bottom right, left) and a non-miniSOG-labeled RGC (bottom right, right).

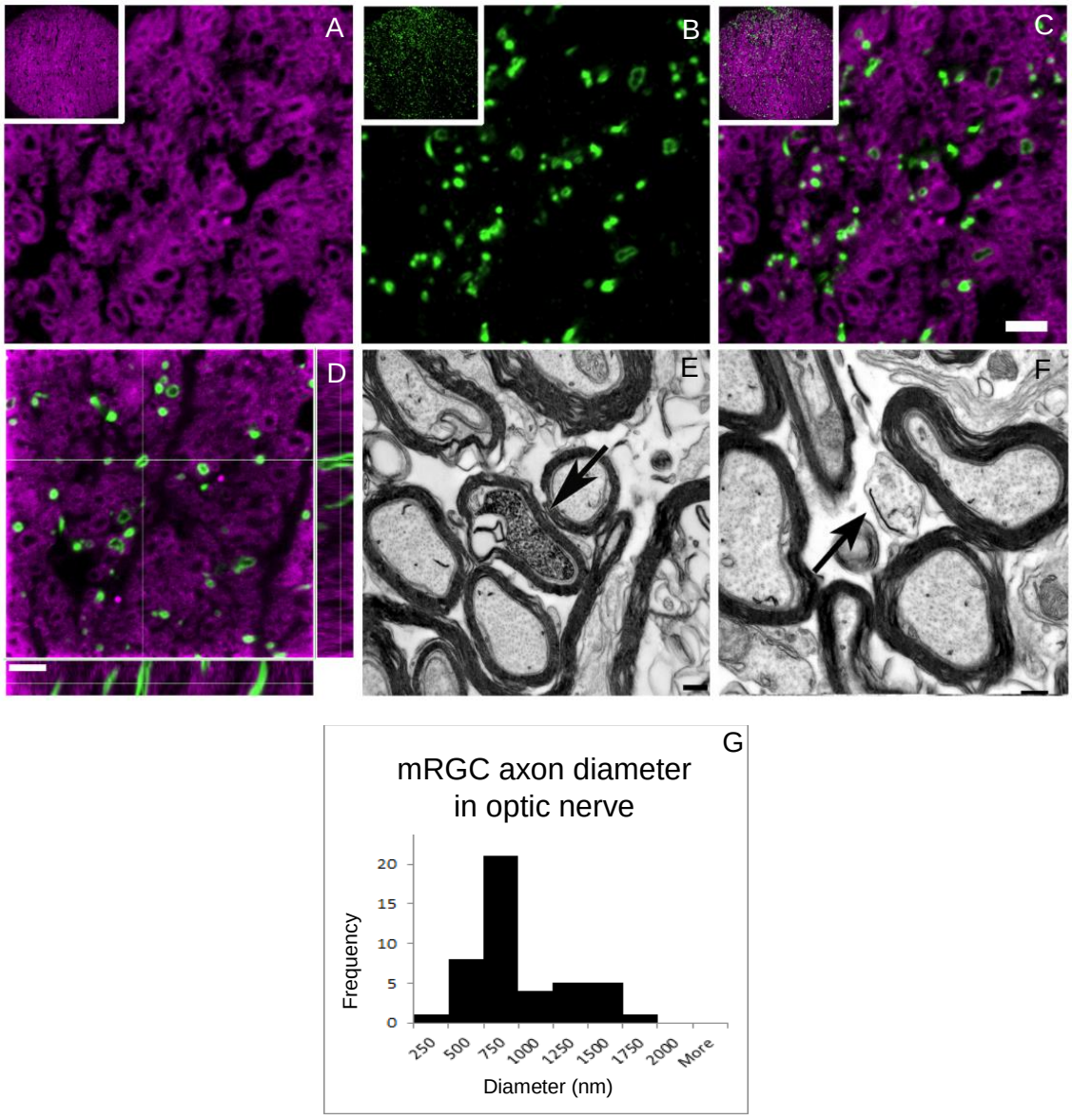

Figure 2.5 MiniSOG labels mRGC axons

Cross-sections of proximal optic nerve from mice with miniSOG-labeled mRGCs (A-D) that are stained for myelin (purple, A,C,D) and miniSOG (B-D); scale bar is 5 um. Inset (A-C) shows wider field of view. EM image of miniSOG-labeled RGC axon sheathed in myelin (E) and non-myelinated RGC axon; Scale bar 10 nm. G: mRGC axon diameters.

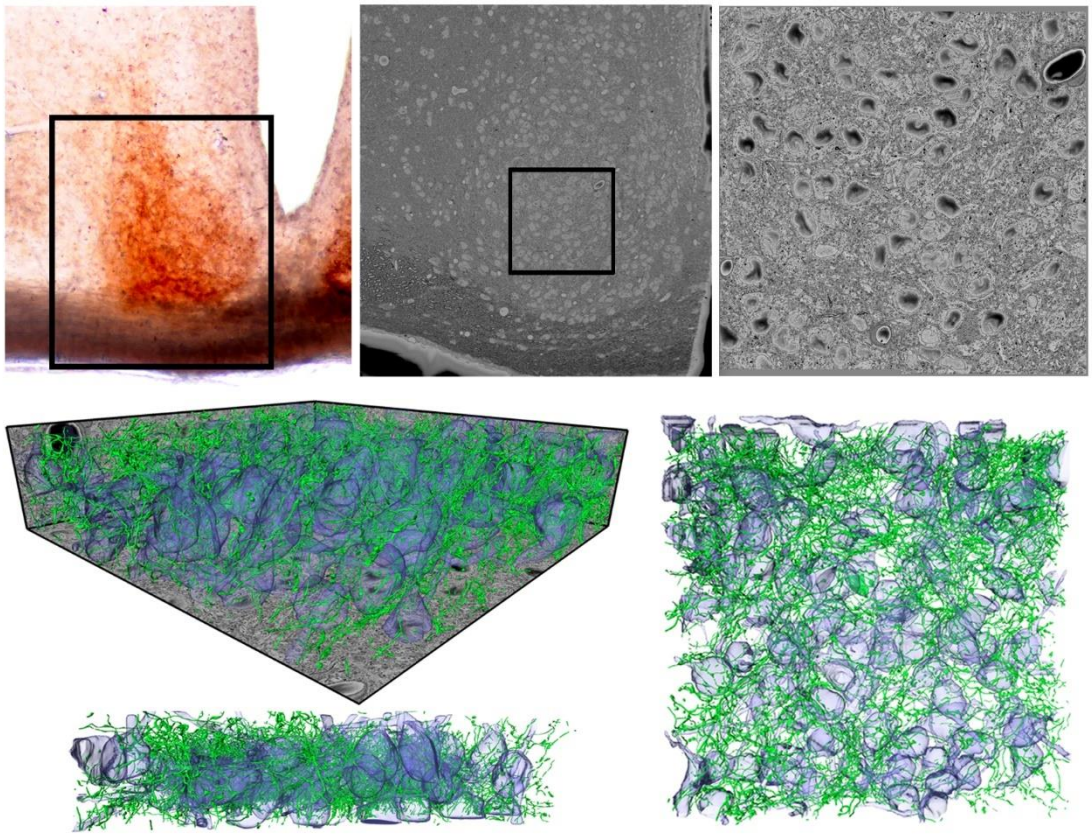

Figure 2.6 Autosegmentation of miniSOG label

MIniSOG label allows for the autosegmentation of mRGC axons in the SCN. Top left: photooxidized mRGC axonal processes in the SCN. Top middle: EM of miniSOG-labeled SCN. Top right: enlarged view of boxed area from Top middle. Bottom left: volume (top) and cross-sectional (bottom) view of automatically segmented mRGC processes (green) and SCN nuclei (blue) from the SCN. Bottom right: *en face* view of automatically segmented mRGC axonal processes and SCN nuclei in SCN.

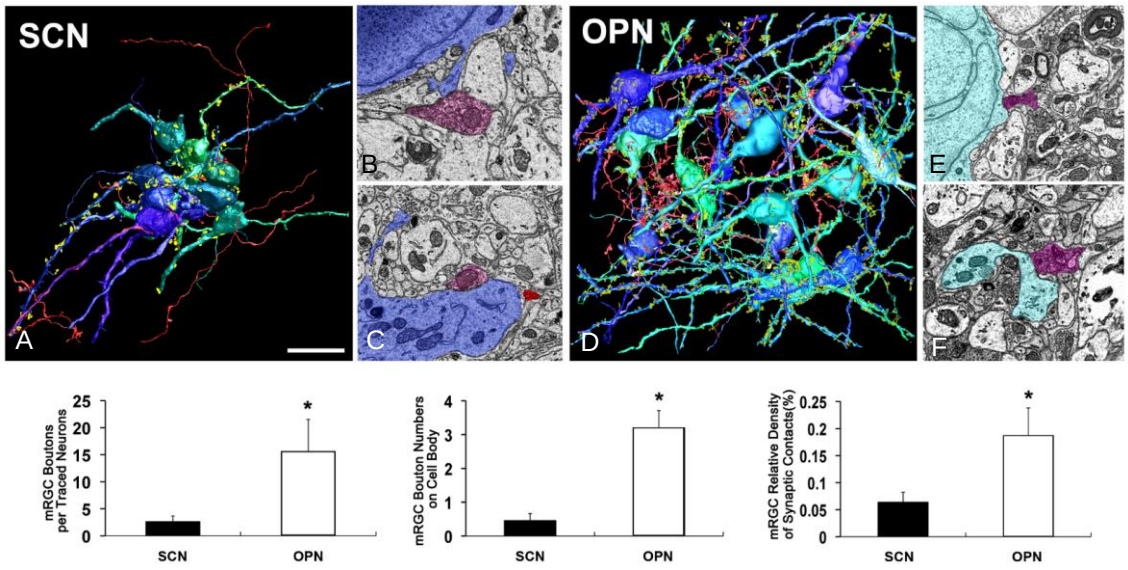

Figure 2.7 mRGC interactions in the SCN and OPN

3D reconstructions of mRGC axons (red) and neurons (shades of green and blue) in SCN (A) and OPN (D) with synapses on select neurons marked in yellow; scale bar is 10 um. EM view of interactions between mRGC axons (shaded purple) and neurons (shaded blue) in SCN (B,C) and OPN (E,F). Bottom left: number of mRGC boutons per traced SCN/OPN neuron. Bottom middle: number of mRGC boutons that synapse with the cell body of a SCN/OPN neuron. Bottom right: mRGC boutons as percentage of all synaptic contacts on a SCN/OPN neuron.

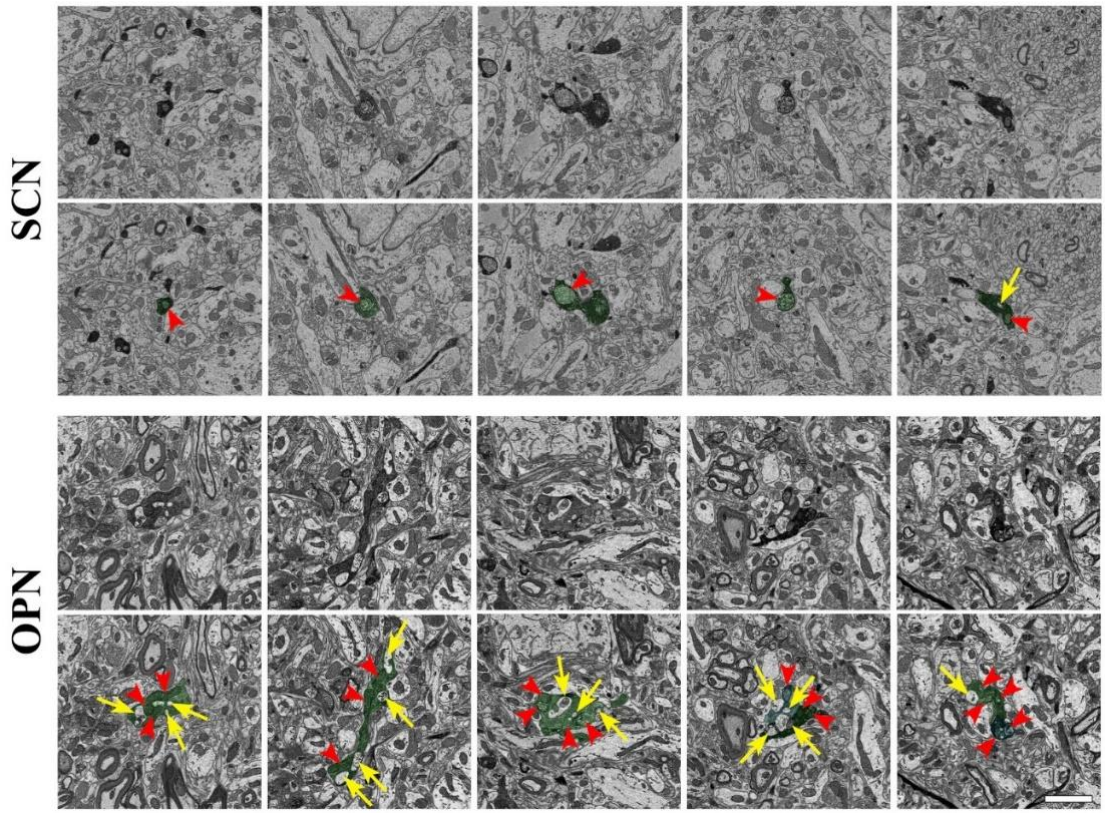

Figure 2.8 Sample mRGC boutons in SCN and OPN

Examples of 5 boutons in SCN and OPN. First row of each set is the raw data. Second row shows green tinted mRGC bouton with mitochondria (red arrowheads) and synaptic intrusions (yellow arrows). Scale bar is 1 um.

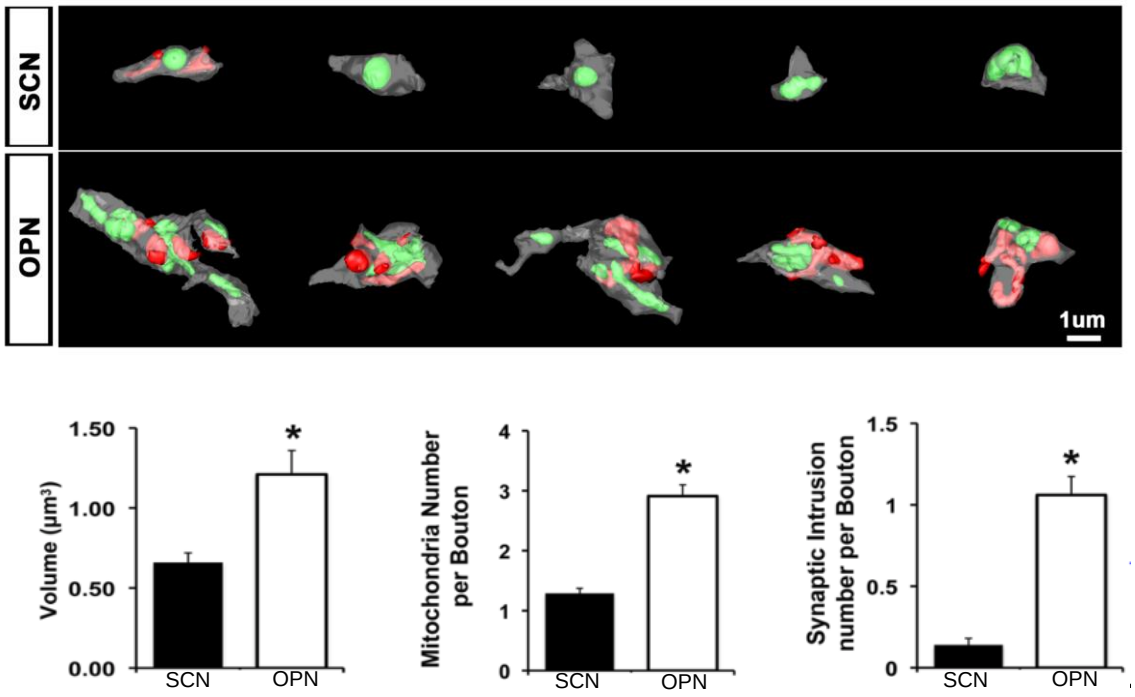

Figure 2.9 mRGC boutons in SCN and OPN

3D reconstructions of boutons in SCN and OPN with mitochondria (green) and post-synaptic intrusions (red).

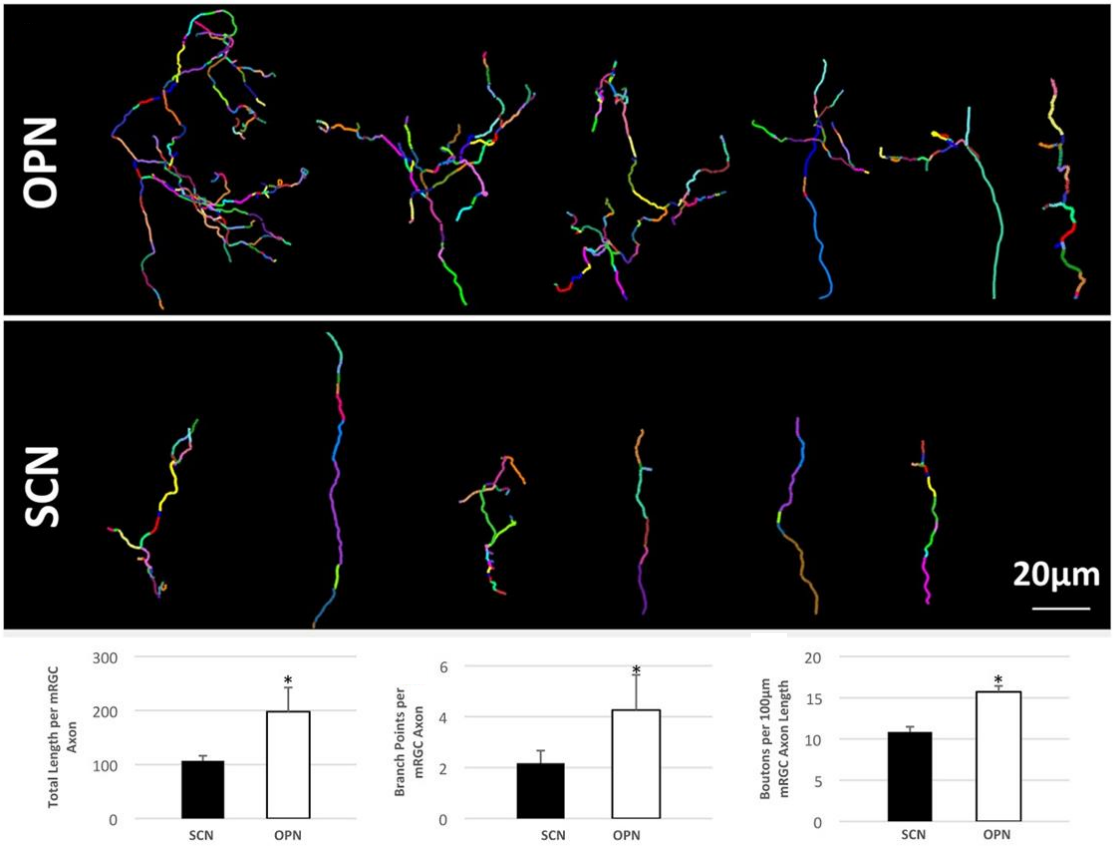

Figure 2.10 mRGC axons in SCN and OPN

mRGC axons in the OPN make more synapses with local neurons and have more branches and boutons than in the SCN. Top: for SCN and OPN, six sample line drawings representing terminal mRGC axons in each region. Each color on the line drawings represents a length of axon between aa synaptic bouton. Axons in the OPN have more branches and more boutons per length of axon.

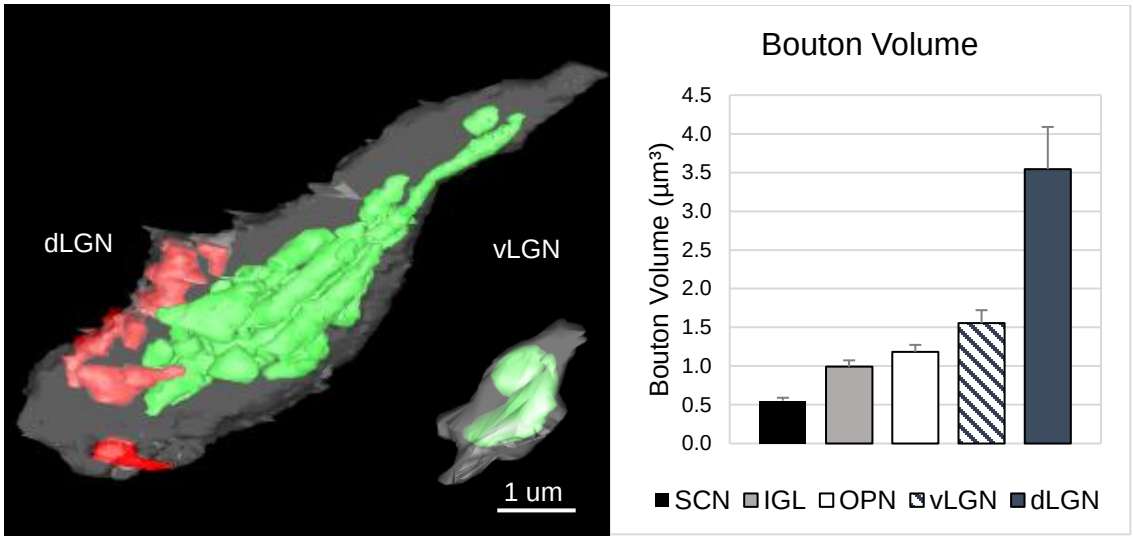

Figure 2.11 mRGC boutons in LGN

Left: Representative 3D reconstructions of one mRGC bouton from dorsal lateral geniculate nucleus and one from ventral lateral geniculate nucleus showing mitochondria (green) and post-synaptic intrusions (red). Right: comparing bouton volume from 5 different mRGC-recipient regions.

2.6 References

Baver, Scott B, Galen E Pickard, Patricia J Sollars, and Gary E Pickard. 2008. "Two Types of Melanopsin Retinal Ganglion Cell Differentially Innervate the Hypothalamic Suprachiasmatic Nucleus and the Olivary Pretectal Nucleus." *The European Journal of Neuroscience* 27 (7): 1763–70.

Berson, David M., Ana Maria Castrucci, and Ignacio Provencio. 2010. "Morphology and Mosaics of Melanopsin-Expressing Retinal Ganglion Cell Types in Mice." *The Journal of Comparative Neurology* 518 (13): 2405–22.

Berson, David M, Felice A Dunn, and Motoharu Takao. 2002. "Phototransduction by Retinal Ganglion Cells That Set the Circadian Clock." *Science (New York, N.Y.)* 295 (5557): 1070–73.

Brown, Timothy M, Carlos Gias, Megumi Hatori, Sheena R Keding, Ma'ayan Semo, Peter J Coffey, John Gigg, Hugh D Piggins, Satchidananda Panda, and Robert J Lucas. 2010. "Melanopsin Contributions to Irradiance Coding in the Thalamo-Cortical Visual System." *PLoS Biology* 8 (12): e1000558.

Chen, S.-K., T. C. Badea, and S Hattar. 2011. "Photoentrainment and Pupillary Light Reflex Are Mediated by Distinct Populations of ipRGCs." *Nature* 476 (7358). Nature Publishing Group: 92–95.

Colwell, C S, and R G Foster. 1992. "Photic Regulation of Fos-like Immunoreactivity in the Suprachiasmatic Nucleus of the Mouse." *The Journal of Comparative Neurology* 324 (2): 135–42.

Deerinck, Thomas J, Eric A Bushong, Andrea Thor, and Mark H Ellisman. 2010. "NCMIR METHODS FOR 3D EM : A NEW PROTOCOL FOR PREPARATION OF BIOLOGICAL SPECIMENS FOR SERIAL BLOCK FACE SCANNING ELECTRON MICROSCOPY," 6–8.

Denk, Winfried, and Heinz Horstmann. 2004. "Serial Block-Face Scanning Electron Microscopy to Reconstruct Three-Dimensional Tissue Nanostructure." *PLoS Biology* 2 (11).

Ecker, Jennifer L, Olivia N Dumitrescu, Kwoon Y Wong, Nazia M Alam, Shih-Kuo Chen, Tara LeGates, Jordan M Renna, Glen T Prusky, David M Berson, and Samer Hattar. 2010. "Melanopsin-Expressing Retinal Ganglion-Cell Photoreceptors: Cellular Diversity and Role in Pattern Vision." *Neuron* 67 (1). Elsevier Ltd: 49–60.

Estevez, ME, PM Fogerson, MC Ilardi, Bart G Borghuis, E Chan, S Weng, ON Auferkorte, Jonathan B Demb, and David M. Berson. 2012. "Form and Function of the M4 Cell, an Intrinsically Photosensitive Retinal Ganglion Cell Type Contributing to Geniculocortical Vision." *Journal of Neuroscience* 32 (39): 13608–20.

Fernandez, Diego Carlos, Yi-Ting Chang, Samer Hattar, and Shih-Kuo Chen.

2016. “Architecture of Retinal Projections to the Central Circadian Pacemaker.” *Proceedings of the National Academy of Sciences*, 201523629.

Güler, Ali D, Jennifer L Ecker, Gurprit S Lall, Shafiqul Haq, Cara M Altimus, Wen Liao, Alun R Barnard, Hugh Cahill, Tudor C Badea, Haiquing Zhao, Mark W Hankins, David M Berson, Robert J Lucas, King-Wait Yau, and Samer Hattar. 2008. “Melanopsin Cells Are the Principal Conduits for Rod/cone Input to Non-Image Forming Vision.” *Nature* 453 (7191): 102–5.

Hatori, Megumi, Hiep Le, Christopher Vollmers, Sheena Racheal Keding, Nobushige Tanaka, Christian Schmedt, Timothy Jegla, and Satchidananda Panda. 2008. “Inducible Ablation of Melanopsin-Expressing Retinal Ganglion Cells Reveals Their Central Role in Non-Image Forming Visual Responses.” *PLoS ONE* 3 (6): e2451.

Hattar, Samer, Monica Kumar, Alexander Park, Patrick Tong, Jonathan Tung, King-wai Yau, and David M Berson. 2006. “Central Projections of Melanopsin- Expressing Retinal Ganglion Cells in the Mouse.” *The Journal of Comparative Neurology* 497 (3): 326–49.

Hattar, Samer, H.-W. W Liao, M. Takao, D. M. Berson, and K-W W Yau. 2002. “Melanopsin-Containing Retinal Ganglion Cells: Architecture, Projections, and Intrinsic Photosensitivity.” *Science* 295 (5557): 1065–70.

Huang, Bo, Mark Bates, and Xiaowei Zhuang. 2009. “Super-Resolution Fluorescence Microscopy.” *Annual Review of Biochemistry* 78 (1): 993–1016.

Ibata, Yasuhiko, Yukio Takahashi, Hitoshi Okamura, Fumio Kawakami, Hirofumi Terubayashi, Toshikazu Kubo, and Noboru Yanaihara. 1989. “Vasoactive Intestinal Peptide (VIP)-like Immunoreactive Neurons Located in the Rat Suprachiasmatic Nucleus Receive a Direct Retinal Projection.” *Neuroscience Letters* 97 (1–2): 1–5.

Jen, Ls, and Rmw Ghau. 1990. “Retinal Ganglion Cells of High Cytochrome Oxidase Activity in the Rat.” *Cell Research* 1 (2): 173–80.

Kremer, J R, D N Mastronarde, and J R McIntosh. 1996. “Computer Visualization of Three-Dimensional Image Data Using IMOD.” *Journal of Structural Biology* 116 (1): 71–76.

Morgan, Josh Lyskowski, Daniel Raimund Berger, Arthur Willis Wetzel, and Jeff William Lichtman. 2016. “The Fuzzy Logic of Network Connectivity in Mouse Visual Thalamus.” *Cell* 165 (1). Elsevier Inc.: 192–206.

Panda, Satchidananda, Trey K Sato, Ana Maria Castrucci, Mark D Rollag, Willem J De Grip, John B Hogenesch, Ignacio Provencio, et al. 2002. “Melanopsin (Opn4) Requirement for Normal Light-Induced Circadian

Phase Shifting.” *Science (New York, N.Y.)* 298 (5601): 2213–16.

Perez, Alex J., Mojtaba Seyedhosseini, Thomas J. Deerinck, Eric A. Bushong, Satchidananda Panda, Tolga Tasdizen, and Mark H. Ellisman. 2014. “A Workflow for the Automatic Segmentation of Organelles in Electron Microscopy Image Stacks.” *Frontiers in Neuroanatomy* 8 (November): 1–13.

Seyedhosseini, Mojtaba, Mehdi Sajjadi, and Tolga Tasdizen. 2013. “Image Segmentation with Cascaded Hierarchical Models and Logistic Disjunctive Normal Networks.” *Proceedings of the IEEE International Conference on Computer Vision*, 2168–75.

Shu, Xiaokun, Varda Lev-Ram, Thomas J Deerinck, Yingchuan Qi, Ericka B Ramko, Michael W Davidson, Yishi Jin, Mark H Ellisman, and Roger Y Tsien. 2011. “A Genetically Encoded Tag for Correlated Light and Electron Microscopy of Intact Cells, Tissues, and Organisms.” *PLoS Biology* 9 (4): e1001041.

Tanaka, Masaki, Yukio Ichitani, Hitoshi Okamura, Yoshifumi Tanaka, and Yasuhiko Ibata. 1993. “The Direct Retinal Projection to VIP Neuronal Elements in the Rat SCN.” *Brain Research Bulletin* 31 (6): 637–40.

Williams, R W, and L M Chalupa. 1983. “An Analysis of Axon Caliber within the Optic Nerve of the Cat: Evidence of Size Groupings and Regional Organization.” *The Journal of Neuroscience : The Official Journal of the Society for Neuroscience* 3 (8): 1554–64.

Zhao, X, B K Stafford, A L Godin, W M King, and K Y Wong. 2014. “Photoresponse Diversity among the Five Types of Intrinsically Photosensitive Retinal Ganglion Cells.” *J Physiol* 592 (Pt 7): 1619–36.

Chapter 3

Subtype- and Stratification-Specific Connections of mRGCs

3.1 Abstract

Melanopsin-expressing retinal ganglion cells (mRGCs) express the opsin-class photopigment melanopsin (gene name *Opn4*) and are intrinsically photosensitive cells in the mammalian retina that are essential for non-image forming (NIF) visual processes. Rod and cone photoreceptor signals funnel through mRGCs to reach regions of the brain that mediate NIF visual processes but in the absence of rods and cones, mRGCs are sufficient to drive NIF visual processes such as circadian photoentrainment and pupillary light reflex. Of the five subtypes of mRGCs, the M1 subtype is identified by its dendritic stratifications only in the OFF-sublamina of the inner plexiform layer (IPL). As such, it is intriguing that the M1 subtype shows a dramatic and sustained ON-light response. The fact that all subtypes of mRGCs are identifiable from one another based on morphological differences and that there is some evidence that different subtypes of mRGCs project to different regions of brain raises the question of whether the different mRGC subtypes receive input from different retinal cells. We use a correlated light and electron microscopy label, miniSOG, to label all mRGCs in the mouse retina and serial blockface scanning electron microscopy to explore mRGC subtype-specific circuitry and the ultrastructural differences that set mRGC-subtypes apart.

3.2 Introduction

Retinal ganglion cells are a heterogeneous population of cells that consist of about 30 different types. They are heterogeneous in their retinal inputs, physiology, and their central projections (Østergaard, Hannibal, and Fahrenkrug 2007). Of the known retinal ganglion cells, there are a small subset- making up 2-4% of all RGCs- that express the photopigment melanopsin (mRGCs) which renders them intrinsically photosensitive (Hattar et al. 2002; Berson, Dunn, and Takao 2002; Ecker et al. 2010). mRGCs project to regions of the brain such as the suprachiasmatic nucleus (SCN) and olivary pretectal nucleus (OPN) that are known to mediate non-image forming (NIF) visual processes such as circadian photoentrainment and pupillary light reflex (PLR), respectively (Baver et al. 2008; Ecker et al. 2010; Gooley et al. 2003; Güler et al. 2008; Hatori et al. 2008).

mRGCs can be divided into 5 subpopulations based on morphology- specifically their dendritic ramification in the inner plexiform layer (IPL) and dendritic branching pattern (Figure 1.2). M1 cells have sparse dendrites that only stratify in the OFF-sublamina. M2, M4, and M5 cells all have dendrites that only stratify in the ON-sublamina. However, M4 cells have twice as many dendrites and a larger dendritic field size as compared to M2 cells and M5 cells had uniquely small dendritic fields with dense branching patterns (Hu, Hill, and Wong 2013). M3 cells have dendrites that stratify in both the OFF- and the ON-sublaminae (Ecker et al. 2010; Viney et al. 2007; Schmidt and Kofuji 2009). Furthermore, the five subtypes of mRGCs have significantly different soma

sizes. In one study, M1s were shown to have soma diameters of 15.7 ± 0.4 um, M2s were shown to have soma diameters around 18.9 ± 0.6 um, and M3s were shown to have soma diameters of 17.8 ± 0.6 um (Schmidt and Kofuji 2011). In another study, M1s had soma diameters of 13.9 ± 0.5 um, M2s had soma diameters of 15.7 ± 0.4 um and M4s had soma diameters of 21.0 ± 0.4 um (Estevez et al. 2012). The soma diameter of M5 cells have not been significantly quantified, but it is generally appreciated that M5 soma diameters are smaller than M1 cells (Ecker et al. 2010; Schmidt, Chen, and Hattar 2011). While it seems that the exact measurements of soma diameters differ between studies, the general consensus is that for soma diameters is that M5 < M1 < M3 ≤ M2 < M4.

The mRGC subtypes also differ in their intrinsic responses to light and whether they tile the retina. M1 cells exhibit much larger and more sensitive light responses than M2 cells (Schmidt and Kofuji 2009). For the most part, M3 and M2 photoresponses were very similar, despite their differing stratification patterns (Hu, Hill, and Wong 2013; Schmidt and Kofuji 2011). M4 cells have photoresponse properties that are very different from M1, M2, and M3 cells but very similar to M5 cells- despite having very different dendritic field diameters (Hu, Hill, and Wong 2013). While M1, M2, and M4 mRGCs independently tile the retina, M3s have not been shown to tile the retina and nothing is known about whether M5s tile the retina (Estevez et al. 2012; Schmidt and Kofuji 2011).

Considering all these differences in mRGC subtype morphology, it is

somewhat surprising that all mRGCs, despite M1 and M3 cells' IPL stratification in the OFF-sublamina, show an ON-response. Taken with the fact that the M1s are thought to serve different NIF visual functions by projecting to different brain region than the other subtypes, it is possible that another distinction that sets mRGCs apart from each other is their intra-retinal partners. Various approaches such as pseudorabies virus retrograde labeling and immunoEM have shown that mRGCs are postsynaptic to amacrine cells and bipolar cells in the IPL and that OFF-stratifying M1 dendrites receive ectopic synaptic input from ON-bipolar cell axons and dopaminergic amacrine cells, but no further details looking into mRGC subtype-specific input exists (Dumitrescu et al. 2009; Jusuf et al. 2007; Belenky et al. 2003; Østergaard, Hannibal, and Fahrenkrug 2007).

To identify the pre-synaptic players involved with different subtypes of mRGCs and the structural differences between them, we use a Cre-dependent vector-mediated approach to express a correlated light and electron microscopy label, mini-Singlet Oxygen Generator (miniSOG, (Shu et al. 2011)), exclusively in the mRGCs of *Opn4*^{Cre} mice. Delivered thus, the miniSOG label fills all mRGCs and their processes with a dark, electron-dense, easily identifiable label. Using automatic and manual segmentation of serial blockface scanning electron microscopy (SBEM) volumes of miniSOG-labeled retina, we reconstruct miniSOG-labeled mRGCs and mRGC processes to identify mRGC subtypes and the structural features that define them. Furthermore, the ultrastructural resolution of SBEM allows us to mark all synapses with mRGCs and segment the cells presynaptic to mRGCs. In this study, we have quantified

the dendritic branching and beading patterns based on mRGC subtype and mRGC dendritic stratification, and have discovered that mRGCs receive inputs from nearly all bipolar cell types and over 5 morphologically distinct amacrine cell types.

3.3 Materials and Methods

Tissue for these experiments came from the same animals and were processed at the same time as tissue that was used for the experiments described in Chapter 2. The relevant overlapping materials and methods relating to the animal work, tissue preparation, and imaging is reproduced here in brief.

Animals

Male and female *Opn4*$^{Cre/+}$ mice between 8 wks and 6 months were used.

Vector construction

A farnesyl sequence was cloned into the 3' end of the miniSOG construct and was inserted in an inverted orientation between the lox sites in an AAV2-DIO vector to create AAV2-DIO-miniSOG-f. AAV2-DIO-miniSOG-f and AAV2-DIO-tdTomato-f was produced by the Salk Gene Transfer, Targeting and Therapeutics Viral Vector Core Facility at titers of 1.09 x 10^{11} TU/ml and 9.41x10^{11} TU/ml, respectively.

Intravitreal injection

3 ul of AAV2-EF1α-DIO-miniSOGm and 0.3 ul of AAV2-EF1α-DIO-

tdTomato was injected into each eye of *Opn4*$^{Cre/+}$ mice between the ages of 8 weeks and 6 months old. Anesthesia is induced and maintained with isoflurane. 0.5% proparacaine (Bausch and Lomb) was applied to each eye prior to any surgical procedure to provide topical analgesia. An initial incision was made in the limbus with a 31-guage insulin needle and virus was injected into the center of the eye through a micromanipulator-mounted 34-guage beveled needle on a 10ul Hamilton syringe. Virus slowly injected over the course of 1 minute and allowed to diffuse through the vitreous for 3 minutes before the needle was slowly withdrawn. GenTeal lubricant eye gel (Novartis) was applied to both eyes and the animal removed from isoflurane anesthesia and placed in a clean cage to recover before returning to its home cage.

Tissue Preparation for SBEM

At least three weeks after intravitreal injection of AAV-miniSOG into *Opn4*^{Cre} mice, the mice were anesthetized with ketamine/xylazine and transcardially perfused with Tyrode's solution followed by 4% formaldehyde/ 0.1% glutaraldehyde in 0.1M phosphate buffered saline (PBS). The retina was dissected and post-fixed with 4% formaldehyde in 0.1 M PBS on ice for 2h. For mini singlet oxygen generator protein (miniSOG) photooxidation, tdTomato-expressing mRGCs were identified using a Leica SPE II inverted confocal microscope and the retinal tissue was fixed with 2.5% glutaraldehyde, 2.5 mM CaCl2 in 0.15 M Sodium Cacodylate buffer (CB) pH 7.4. Tissue was then rinsed with ice cold CB, and blocked for 30 min with 50 mM glycine, 10 mM Potassium cyanide and 5 mM aminotriazole in CB. Freshly prepared diaminobenzidine

(DAB free base, Sigma) in CB was added to the tissue, and mRGCs were illuminated with 450–490 nm light from a Xenon lamp for 20–25 min until a light brown reaction product was observed in place of the green fluorescence of miniSOG. The tissue was then processed for SBEM.

SBEM Staining and Imaging

Tissue was prepared for SBEM as previously described (Deerinck et al. 2010). Briefly, tissue was washed with 0.15 M CB and then placed into 2% OsO4/1.5% potassium ferrocyanide in 0.15 M CB containing 2 mM CaCl2. The slices were left for 30 min on ice and then 30 min at room temperature (RT). After thorough washing in double distilled water, the slices were placed into 0.05% thiocarbohydrazide for 30 min. The slices were again washed and then stained with 2% aqueous OsO4 for 30 min. The slices were washed and then placed into 2% aqueous uranyl acetate overnight at 4°C. The slices were washed with water at RT and then stained with en bloc lead aspartate for 30 min at 60°C. The slices were washed with water and then dehydrated on ice in 50%, 70%, 90%, 100%, 100% ethanol solutions for 10 min at each step. The slices were then washed twice in dry acetone and then placed into 50:50 Durcupan ACM:acetone overnight. The slices were transferred to 100% Durcupan resin overnight. The slices were then flat embedded between glass slides coated with mould-release compound and left in an oven at 60°C for 72 h. SBEM data was collected with a 3View unit (Gatan Inc., Pleasanton, CA, USA) installed on a Merlin field emission SEM (Carl Zeiss Microscopy, Jena, Germany). The retina volumes were collected in 2.0 to 2.4 kV accelerating

voltages, with a raster size of 20k×20k or 24kx24k and pixel dwell time of 0.5 - 1.5 µms. The pixel sizes were 4.0-7.3 nm, depending on the raster size and section thickness was 60-70 nm. Before each volume was collected, a low magnification (~500×) image was collected of the block face to confirm the anatomical location of the volume based on tissue landmarks, such as the RGCs and blood vessels. Once a volume was collected, the histograms for the slices throughout the volume stack were normalized to correct for drift in image intensity during acquisition. Digital micrograph files (.dm4) were normalized using Digital Micrograph and then converted to MRC format. The stacks were converted to eight bit, mosaics were stitched, and volumes were manually or semi automatedly traced for reconstruction and analysis.

Manual segmentation

3D reconstruction of mRGCs and mRGC processes. The miniSOG label fills labels mRGC-membranes and fills mRGC processes with a dark, easily-recognizable label. Using IMOD software (University of Colorado, Boulder, (Kremer, Mastronarde, and McIntosh 1996)), mRGCs were identified by finding miniSOG-labeled cell bodies in the ganglion cell layer of the SBEM volumes. mRGC processes were identified by finding miniSOG-labeled cross sections in the inner plexiform layer of the SBEM volumes. mRGC somata or mRGC processes of interest were assigned a unique object number and followed through the SBEM volume. Using the drawing tools in IMOD, contours were drawn around contiguous miniSOG-labeled cross sections of the object as its processes branched and spread across the volume such that there was

always some overlap in the x,y coordinates of the contours across slices. The miniSOG-labeled processes of any object were followed to the fullest extent of the volume. The IMOD routine *imodmesh* was used to render the segmented objects in 3D.

For Volume_3, all miniSOG-labeled processes were segmented in a 92.4 x 92.4 x 51.0 um block that consisted of the IPL from the majority of Volume_3's surface area. The block was broken into grids of 9.24 x 9.24 x 51.00 um and all miniSOG-labeled processes in individual grids were manually segmented by 4 different observers. The models for all the grids were then joined back together using the IMOD routine *imodjoin* and obviously connected objects were combined into one object. This two-step manual segmentation and post-processing approach guarantees that all segmented objects are checked by at least two observers- one who segmented the grid and another who joined the objects together.

Dendrite/ mRGC volume. Objects representing miniSOG-labeled mRGC processes or mRGCs were meshed with the IMOD routine *imodmesh.* The IMOD routine *imodinfo* returned the volume of each object.

mRGC synaptic density. Putative synapses were identified as sites where the presynaptic membrane came in contact with contiguous miniSOG-labeled processes for at least 4 vertical sections or 240 linear nanometers and where vesicles were docked at or within one vesicle's diameter of the pre-synaptic plasma membrane directly opposed to a miniSOG-labeled mRGC cross section. All putative synapses were marked and counted for each mRGC

with dendritic arbors in the three retina volumes (nine of ten total mRGC somata) by two experienced researchers to give the total number of putative synapses. To calculate dendritic length, using the point function of IMOD's drawing tools, open contours were used draw a skeleton along the dendritic processes of the nine arbored-mRGCs such that each branch was recapitulated by a separate contour. All skeletons were checked by two separate observers. The IMOD routine *imodinfo* returned the length of the contours. Synaptic density was calculated by dividing the number of putative synapses along a length of dendrite by the length of the dendrite.

Bead-Expansion Ratio. For each segmented unique object, the "measure" drawing tool in IMOD was used to measure the length of a line drawn perpendicular to the direction of travel of the dendrite and across the widest part of a dendritic bead or stretch of dendrite halfway between two beads. For each object, all beads and inter-bead dendrites were measured and the corresponding layer of stratification (strata 1 through 5, 1 being the stratum closest to the inner nuclear layer) in the inner plexiform layer was recorded. Bead-expansion ratios were calculated by dividing the average bead diameter by the average dendrite diameter.

Identification and backtracing of cell types presynaptic to mRGCs. For all identified putative synapses to mRGC dendrites, the marked presynaptic terminal was manually followed through the image stack. To backtrace the presynaptic cells, continuous open contour points were laid in the center of the presynaptic cell's cross sections to represent the branching pattern of the

presynaptic cell. Each time a process branched, a new contour would be used to mark the new branch. The resulting skeleton would capitulate the layers in which the presynaptic cell stratified its dendrites/axons, branching pattern of the presynaptic cell, location of the presynaptic cell's soma, and inputs to the presynaptic cell. The skeletonized presynaptic cell is identified by comparing its morphology to the known morphologies of identified bipolar cell types as described in Ghosh et al. 2004 and the amacrine cell types described in Macneil et al. 1999. In some cases, full closed contour 3D reconstructions of presynaptic cells were made by tracing the plasma membrane of as many presynaptic cell cross-sections as were necessary reconstruct the cell in 3D using the IMOD routine *imodmesh*.

Automatic segmentation

Using IMOD, for retina Volume_2, the threshold-based routine, *imodauto,* was used to draw contours around pixels with intensity higher than a defined threshold. *Imodmesh* was used to reconstruct and obtain 3 dimensional models of the miniSOG-labeled structures in the EM datasets. Finally, 3-dimensional connected objects were separated into different objects using the IMOD routine *imodsortsurf*. False positives were removed from the model and relevant objects of interest were combined manually.

For retina Volume_1, we used Ilastik (Sommer et al. 2011) to execute a processing step before post-processing with IMOD. In Ilastik, we used a pixel classification workflow and then an object-level classification step to generate binary masks for the axons and neurons labeled with miniSOG. Both classifiers

are learned from training data provided by the user using labels to separate object types (two labels are used, one for the axons or neurons and the other for the background). The output of Ilastik is then converted to an IMOD compatible format for further analysis. In IMOD, contours are drawn around the binary masks, as stated above before, using the routine *imodauto*. All the subsequent steps of processing are similar to the first procedure.

3.4 Results

3.4.1 Retina volumes

Four retina volumes were generated for these studies, but only three of the volumes, Volume_1, Volume_2, and Volume_3, were of sufficient quality, in terms of resolution and imaging/processing artifacts, for segmentation (Figure 3.1). Because mice lack a fovea or visual streak (Carter-Dawson and LaVail 1979), all retinal cell types, including mRGCs (Berson, Castrucci, and Provencio 2010) are largely equally distributed across the retina. All imaged retinal volumes were taken from regions of the retina that were not damaged and not immediately adjacent to the optic disc or the virus injection site.

Volume_1 contained 3 mRGC cell bodies (2.2% of all cells in GCL; Figures 3.1, 3.2), covered the greatest surface area of retina (dimensions: 136 x 133 x 60 um; total volume = 1,085,280 um^3), had the least amount of alignment and charging artifacts, and spanned the region between the outer edge of the ganglion cell layer (GCL) and the inner edge of the outer plexiform layer (OPL).

Volume_2 contained 4 mRGC cell bodies (3.6% of all cells in GCL;

Figures 3.1 and 3.3), 3 of which had significant dendrites, encompassed a total volume of 749,000 um^3 (dimensions: 140 x 107 x 50 um), and spanned the region between the outer edge of the GCL and the inner edge of the INL. The variable charging artefacts in the bottom 20% of the volume and the fact that the INL was not encompassed in this volume precluded this volume from backtracing for presynaptic cells.

Volume_3 contained 3 mRGC cell bodies (3.7% of all cells in GCL; Figures 3.1 and 3.4), covered the smallest amount of retinal surface area (dimensions: 103 x 106 x 127_um; total volume = 1,386,586 um^3), and spanned the full thickness of the retina from GCL to the outer segments of the photoreceptors. Despite some alignment artefacts along the midline in the vertical and horizontal directions where four smaller volumes were stitched together in a 2 x 2 block, the capitulation of the full-thickness retina made this volume enticing for complete segmentation.

The distribution of mRGCs within the three volumes agrees with existing literature on mRGC density in the GCL (Berson, Castrucci, and Provencio 2010). All 5 morphologically-defined subtypes of mRGCs could be identified from the 9 mRGCs in these three volumes that had significant dendrites. In total, 10,524.12 um (2,826.78 um from Volume_1, 2,322.15 um from Volume_2, and 5,375.19 um from Volume_3) of dendritic length was measured from the 9 mRGCs in all of the volumes (Figure 3.5). Based off of the soma size and dendritic stratification of the segmented mRGCs, Volume_1 contains an M1, M4, and M5, Volume_2 contains an M2, M3, and M4, and Volume_3 contains

an M2, M3, and M5. (Figure 3.6).

3.4.2 mRGC processes cover the majority of the retina surface area

Despite some alignment artefacts along the midline in the vertical and horizontal directions, the capitulation of the full-thickness retina made Volume_3 particularly enticing for complete segmentation of miniSOG-labeled processes. In Volume_3, all miniSOG-labeled processes were manually segmented from a 92.42 x 92.42 x 51.00 um block of tissue (total volume = 435,614.28 um^3) that encompassed the entire ganglion cell layer (GCL) and inner plexiform layer (IPL).

The miniSOG-labeled processes revealed a total of 332 unique miniSOG-labeled objects in the volume which included 3 mRGC cell bodies and their dendritic and axonal processes, 61 miniSOG-labeled axonal processes, and 268 other unique objects representing separate dendritic processes in the IPL (Figure 3.7). MiniSOG-labeled processes occupied 0.4% of the whole IPL volume (total IPL volume 384,490.31 um^3; 92.42x92.42x45um (sections 100-850)) and mRGCs made up 3.7% of all GCL cell bodies. In total, the miniSOG-labeled processes and cell bodies covered 56.50% (Figure 3.8) of the retinal surface area and spanned the full thickness of the IPL with 82.34% of all miniSOG-labeled processes (consisting of 280 unique objects) within strata 4 and 5 (occupying 1.22% of strata 4 and 5 volume). 13.29% of the processes (consisting of 22 unique objects) occupying strata 1 and 2 of the OFF-sublamina (occupying 0.20% of strata 1 and 2 volume), and 4.37% of the

processes (consisting of 16 unique objects) occupying strata 3 (occupying 0.11% of strata 3) (Figure 3.9).

Some objects in the volume do not stratify to just the ON- or OFF-sublamina and instead span the full thickness of the IPL (Objects 101, 265, 41, and the mRGC “V3_left”. One of these processes is an ectopic branch off of an axon, one is a primary dendrite of an M1 mRGC, one is the M3 mRGC from the center of the volume, and others are M3-like processes (Figure 3.10). The three miniSOG-labeled mRGCs in this volume were completely segmented to the fullest extent of the volume in order to try to capture as much information about the mRGCs as possible. Due to the dimensions of the volume, only the proximal dendritic field (up to ~50 um from the center of the cell body) could be segmented. Within the volume, the proximal dendritic processes (50 um radius from center of the cell body) and the cell bodies of the three mRGCs covered 19% of the retinal surface area and occupied 0.02 % of the volume of the IPL, which is 5.39% of all segmented mRGC processes within the fully segmented block.

3.4.3 Dendritic morphology of mRGC processes

For all segmented objects that were longer than 10 um, including those from the mRGCs with somata in the volume, the branching and bead pattern was quantified in terms of branch length and number of beads per branch. From the fully segmented mRGC dendritic processes in Volume_3, mRGC dendrites that stratified in the ON-sublamina had shorter internal branch lengths

(average 11.58) than those that stratified in the OFF-sublamina (average 12.28); as measured by the average lengths of dendrite between branchpoints (*Figure 3.11*, top). As comparison, the internal branch lengths of a single bistratified mRGC (V3_middle, an M3 subtype mRGC from Volume_3) showed a similar pattern where the internal branch lengths of the ON-stratifying dendrites (average 9.00 um) were shorter than those of the OFF-stratifying dendrites (average 10.79 um) (Figure 3.11, bottom). When comparing the internal branch lengths of all ON-stratifying proximal dendrites (dendrites that are connected to a cell body in the volume, and hence, within 50 um of the cell body) and distal dendrites (dendrites that do not have cell bodies within the volume), the internal branch lengths of ON-stratifying proximal processes are shorter than those of the ON-stratifying distal processes (Figure 3.12, top). Of the ON-stratifying dendrites, those that belong to the ON-stratifying dendrites of V3_middle are shorter (average 9.00 um) than those of all other ON-stratifying mRGC processes (average 14.06 um) (Figure 3.12 bottom).

To characterize the bead-like varicosities, for all mRGCs greater than 10 um, all the beads along a length of dendrite were counted. The length of the dendrite divided by the number of beads on the dendrite gives the interbead distance. ON-stratifying mRGC processes had smaller distances between beads than OFF-stratifying mRGC processes (average 3.42 vs 4.86 um, respectively) (Figure 3.13, top left) whereas the interbead distances between proximal (within 50 um of cell body) and distal dendrites (average 3.36 vs 3.42 um, respectively) (Figure 3.13, top right) and between the proximal dendrites of

each of the three mRGCs in Volume_3 (average 3.55, 3.33, and 3.22 um for V3_left, V3_middle, and V3_right, respectively), were roughly the same (Figure 3.13, bottom).

We measured the diameter for every bead and an adjacent stretch of dendrite as the longest line perpendicular to the direction of dendritic projection. Dividing the bead diameter by the dendrite diameter gives a “bead-expansion ratio” that describes how many times greater the diameter of a bead is than the surrounding dendrite. The bead expansion ratio for each object was positively correlated with axon diameter. Bead-expansion ratios were greater in the ON-sublamina vs the OFF-sublamina (Figure 3.14).

3.4.4 Synaptic density of mRGCs

Synaptic density, synapses per 10 um dendritic length, was calculated for all mRGCs in all volumes. Figure 3.15 shows the synaptic map of the M2 subtype mRGC V3_right from Volume_3 with all synapses on the V3_right skeleton (purple lines) marked with green contours and orange contours denoting the synapses that could be traced back to a cell body. Putative synapses were identified based off of docked, or near-docked (within one vesicle’s diameter of the membrane) and significant membrane to membrane contact between the presynaptic terminal and the miniSOG-labeled process. In Volume_1, the synaptic density of the M4 (total dendritic length = 1,302.10 um), M1 (total dendritic length = 595.13 um), and M5 (total dendritic length = 929.55 um) was 4.03, 3.66, and 4.12, respectively. In Volume_2, the synaptic density

of the M2 (total dendritic length = 534.54 um), M3 (total dendritic length = 1,514.84 um), and M4 (total dendritic length = 282.77 um) was 3.33, 2.65, and 4.17, respectively. In Volume_3, the synaptic density of the M2 (total dendritic length = 1,596.25 um), M3 (total dendritic length = 3,075.14 um), and M5 (total dendritic length = 703.80 um) was 1.41, 2.20, and 3.00, respectively (Figure 3.5).

In marking all synapses on the segmented mRGCs, an interesting feature of the M4 mRGC, V1_green, in Volume_1 was noted. Occurring at a frequency of 0.95 every 10 um, there was a unique synapse ultrastructure where very fine tendrils of miniSOG-labeled membrane would bud off of the mRGC dendrite and engulf a small protrusion from a presynaptic terminal forming a tight cap (Figure 3.16). These cap synapses were occasionally seen on other ON-stratifying mRGC subtypes across volumes.

Though bipolar cell synapses are classically thought to contain ribbon synapses. Very few putative axodendritic synapses between bipolar cells and mRGCs were ribbon synapses. The vast majority of putative axodendritic synapses between bipolar cells and mRGCs were conventional synapses where neurotransmitter vesicles were found docked at the bipolar cell terminal membrane directly opposed to miniSOG-labeled mRGC processes (Figure 3.17).

3.4.5 mRGC subtype determines intra-retinal interactions

In Volume_1 and Volume_3, cells presynaptic to segmented mRGCs in

those volumes were reconstructed by starting at an identified putative synapse and backtracing or segmenting the cell that contains the presynaptic contour backtracing. Both full contours segmentations and open-contour skeleton tracings were used to follow and mark the processes of presynaptic cells back to a cell body in the INL. The skeletons were elaborated to include as many dendritic or axonal branches as possible- to flesh out the dendrites of amacrine cells for better classification, and to follow bipolar cell processes back to a rod spherule or cone pedicle to confirm bipolar cell type. Over 100 bipolar and amacrine cells were backtraced from various mRGCs that encompassed all mRGC subtypes. Both bipolar cells (Figure 3.18) and amacrine cells (Figure 3.19) were identified from backtraced cells. Figure 3.20 summarizes the cell types presynaptic to the different mRGCs segmented from Volume_1 and Volume_3.

Rod bipolar cells (RBC), which are not thought to directly synapse onto ganglion cells (Kolb 1979) were shown to directly come in contact and make putative synapses with miniSOG-labeled mRGC processes. In one case, the RBC terminal made direct and persistent contact to the soma of the M1 mRGC in Volume_1 (Figure 3.21). In another case, an RBC made ectopic axonal *en passant* to OFF-stratifying mRGC dendrites.

Dendritic stratification in the IPL generally dictates the inputs that an mRGC dendrite would receive, however because mRGC dendrites do not solely ramify in a narrow band in the IPL, but instead undulate within the IPL, mRGCs receive inputs from a remarkable diversity of presynaptic partners. The

exceptions to the dendritic-stratification-dependent view of presynaptic inputs to mRGCs is that OFF-stratifying M1 and M3 dendrites receive input from *en passant* synapses off of the axons of ON-bipolar cells. This has been documented for OFF-stratifying dendrites of M1 cells (Hoshi et al. 2009; Dumitrescu et al. 2009; Lauritzen et al. 2013) especially in the area of the IPL directly up against the INL, but has yet to be described for the M3 (Figure 3.22)

3.5 Discussion

3.5.1 Subtype- or stratification- specificity

mRGCs can be divided morphologically into 5 subtypes. When factoring connectivity into studying the structure of mRGC subtypes, it is important to know which characteristics are intrinsic to the cell and which characteristics are a result of outside local influence. Which features of the mRGC's structure are subtype-dependent and which features are stratification-dependent? Identifying the stratification- or connection-dependent features gives greater insight into the function of the cell.

It was originally thought that the stratification of all retinal ganglion cell (GC) dendrites in the IPL defined its connectivity. GC dendrites that stratified in the outer IPL, or the OFF-sublamina, received glutamatergic inputs from OFF-bipolar cells in response to the cessation of light. GC dendrites that stratified in the inner IPL, or the ON-sublamina, received glutamatergic inputs from ON-bipolar cells which release glutamate in the presence of light (Kolb 1979). Following this stratification rule, one would expect the M1 mRGCs, with their

dendrite that stratify in the OFF-sublamina, to exhibit an OFF-response, M2, M4, and M5 mRGCs with their dendrites in the ON-sublamina to have an ON-response and M3 mRGCs with their dendrites in both the ON- and OFF-sublaminae to have a more complex response as dictated but the input from two different light signals. However, M1 and M3 mRGCs break this rule by exhibiting a sustained ON-response (Zhao et al. 2014). This reveals gaps in our understanding of intraretinal connectivity and adds emphasis on the need to consider connectivity in defining function.

Branch length is a stratification-dependent feature. Analysis of branch length in the Volume_3 miniSOG-labeled mRGC processes showed that ON-sublamina-stratifying dendrites had shorter branches (Figure 3.13, top left) compared to OFF-stratifying dendrites. This suggests that branching pattern may be a stratification-dependent feature. In fact, when we look at the internal branch lengths (branches that are not terminal branches and that do not project beyond the bounds of the volume) of the M3 in Volume_3, the average internal branch length of dendrites stratifying in the ON-sublamina and OFF-sublamina are 9.00 and 10.79 um, respectively. If branch length were subtype-dependent, the branch lengths of the three levels of M3 dendrite would likely have all had a similar internal branch lengths. Instead, the branch length pattern within this M3 shows a gradient in branch length that mirrors the gradient seen in all other miniSOG-labeled mRGC processes. However, proximal dendrites have shorter internal branch lengths than distal dendrites, suggesting that internal branch lengths may vary within one subtype depending on how far from the cell-body

measurements are being made.

Interbead distance, the distance between beads, is also a stratification dependent feature, and bead expansion ratio, the relationship between diameters of dendritic beads to the base diameter of dendrites, are also stratification-dependent. ON-stratifying dendrites have shorter interbead distances than OFF-stratifying dendrites (3.42 vs 4.86 um, respectively, Figure 3.13 top left); whereas all ON-stratifying dendrites have very similar interbead distances regardless of whether they are proximal or distal dendrites (Figure 3.13, top right and bottom). The bead expansion ratio is much larger in ON-stratifying mRGC processes than in OFF-stratfying mRGC processes. Further break-down of the bead expansion ratio within the ON-sublamina shows that bead expansion ratio in strata 4 is less than that of strata 5 (Figure 3.23).

In terms of dendritic morphology, we gather an overall picture where dendrites that stratify in the ON-sublamina, have shorter branches with more frequent and more prominent beads than the dendrites that stratify in the OFF-sublamina (Figure 3.24).

Although we measured synaptic density on all mRGCs, there are not enough mRGCs of each subtype to determine with any sort of certainty whether synaptic density is a stratification- or subtype- specific feature. While comparing values across volumes and between mRGCs of the same subtype, the most striking relationship is between the M4 in Volume_1 and the M4 in Volume_2. Both of these M4s had similar synapse densities (4.03 s 4.17) and similar bead densities (0.94 and 0.95). The lack of convergence between similar subtypes

across volumes may be due to the fact that all other mRGC subtypes have finer processes that the M4 mRGCs. The finer the process, the higher the likelihood of being unable to follow it though the volume which would ultimately result in an underestimation of mRGC total dendritic length. Furthermore, the variation in resolution across volumes makes it difficult to trace all mRGCs in each volume with the same fidelity.

3.5.2 Pre-synaptic players in mRGC circuitry

Our catalog of over 100 bipolar and amacrine cells that have been backtraced from putative synapses with miniSOG-labeled dendritic process is the broadest study of mRGC pre-synaptic cell types to date. Bipolar cells are classically identified by the presence of ribbon synapses- electron dense structures anchored to the presynaptic membrane to which are docked hundreds of synaptic vesicles (Kolb, 1979; reviewed in LoGiudice & Matthews, 2009). However, bipolar cells are also known to have ribbon-free synapses that are driven by PKC activation (Midorikawa et al. 2007). Circadian studies of synaptic ribbons in ON-bipolar cell terminals in goldfish revealed that there were 65% fewer ribbons in the bipolar cell terminal at night. Concurrent with that decrease in ribbon number, recordings of membrane capacitance showed a significant reduction in exocytosis due to fast depolarization (20 ms light stimulus) during the night but a similar exocytic response to 200-ms depolarization between night and day. This suggests that the synaptic ribbons may be involved in fast, synchronous release and that longer depolarizations

released non-ribbon-associated docked vesicles (Hull et al. 2006). The fact that exocytic response under longer light stimulation did not change in longer light exposures regardless of ribbon synapse content, may explain why the majority of synapses between backtraced bipolar cells and segmented mRGCs did not contain a ribbon synapse. mRGCs are known to show sustained ON-responses in response to light (Hu, Hill, and Wong 2013). This slow and sustained response may be directly related to receiving synapses from non-ribbon associated docked vesicles from bipolar cells.

Bipolar cells are the second order neurons in the retina and play an important role in parallel processing because light information from rod and cone photoreceptors immediately get split into all bipolar cell types and sent through the IPL to converge on the GCL. The IPL is structured such that the bipolar cells that stratify closest to the Inner nuclear layer have slow OFF-responses and those that stratify closest to the GCL have slow ON-responses- with decreasing excitatory synaptic currents from the upper and lower bounds of the IPL towards the border between the ON- and OFF-sublaminae such that Type 5 cone bipolar cells, which stratify in strata 3 just proximal to the boundary of the OFF-sublamina shows a fast ON response (Baden et al. 2013). Since M4 mRGCs are more likely to stratify in strata 4 of the IPL, closer to the ON- OFF-sublaminae boundary, as compared to M2 and M5 mRGCs which tend to stratify in strata 5 of the IPL (Estevez et al. 2012), they likely receive faster ON-bipolar cell signals than M2s and M5s. Considering their implicated role in pattern forming vision due to their axonal projections to the dLGN, the faster

bipolar excitatory synaptic signals may allow the weakly intrinsically photosensitive M4 mRGCs to play a role pattern forming vision (Ecker et al. 2010).

In our survey of presynaptic cells, we have one instance of a rod bipolar cell synapsing directly onto the soma of an M1 mRGC. We have many more instances where rod bipolar cell terminals contact ON-stratifying dendrites of all other mRGC subtypes. This is in line with electrophysiology data showing that all five mRGC subtypes generated rod-mediated light responses (Zhao et al. 2014). This direct rod bipolar cell to ganglion cell input has been suggested in immunohistochemical studies (Østergaard, Hannibal, and Fahrenkrug 2007) but here in our volume we have the ultrastructural resolution to actually see the synapse (Figure 3.21). The direct RBC to M1 cell body input may provide light information in low light conditions to facilitate the mRGC's role in circadian photoentrainment.

3.5.3 Limitations

The vector-mediated expression of our miniSOG label fills all dendritic and axonal processes with a dark, electron-dense label. This dark label makes auto-segmentation possible and the mRGC processes easy to follow through the retinal volume. However, this dark label also obscures post-synaptic densities (PSD) and organelles within the dendritic processes. While in certain more lightly photooxidized sections, the contrast of the image can be adjusted

such that the PSD is apparent (Figure 3.25), most non-ribbon synapses from presynaptic bipolar cells terminals cannot be verified by visualization of the PSD in miniSOG-labeled dendrites. The miniSOG label also precludes the accurate counting of mitochondria within mRGC processes. Preliminary evidence showed that mRGCs have a greater volume fraction of mitochondria than other retinal ganglion cells (Figure 2.4, top right). Given that the mitochondria are located predominantly in the soma and the dendritic beads, being able to segment the mitochondria in our completely segmented Volume_3 block would have offered some valuable insight into whether there were subtype-specific differences in mitochondria position or volume.

Despite the excellent miniSOG label, all volumes were imaged with a 60 nm z-step size. This step size is largely sufficient for segmentation, however, because the step size is so small, miniSOG-labeled mRGC processes or bipolar/amacrine cell processes that are moving tangentially through the volume can often be lost. Similarly, very fine processes are also difficult to follow through the volume. As such, all measures of dendritic length for the 9 mRGCs in the 3 volumes might all be underestimations. The discrepancy between the measured dendritic length and the actual dendritic length might be even bigger for mRGCs in Volume_2 since the variable resolution of Volume_2 made some processes extremely difficult to follow.

Although miniSOG-labeled processes may be difficult to follow, tremendous effort was made to follow all processes from mRGC cell bodies to their fullest extent within the volume and to mark all synapses on those mRGC

processes. Since dendritic length might be underestimated, and since this method does not allow for a functional assessment of whether a presynaptic terminal with vesicles docked near the membrane are actually synapses or not, it is possible that synaptic density measurements are overestimated.

Lastly, because of how large mRGC dendritic field sizes are and how small our volumes are in relation to the mRGC dendritic field size, all subtype-specific quantifications were generated by measuring only the proximal dendrites (<50 um from the center of the mRGC soma). Since the ON-sublamina of the IPL is densely packed with mRGC processes from up to four different mRGC subtypes, it is impossible to pull subtype-specific information out of these miniSOG-labeled distal mRGC dendrites that course through the volume but are not attached to cell bodies within the volume.

3.5.4 Autosegmentation

The complete segmentation of miniSOG-labeled mRGC processes to calculate mRGC volume is extremely time consuming. The complete segmentation of all miniSOG-labeled processes in Volume_3 (totaling 11,491.74 um in length, 5,375.19 um from the 3 mRGCs in the volume and 6,116.55 um from all other miniSOG-labeled dendrites) required over 1500 hours split between 4 observers working part-time explicitly on this task over the course of 4 months. This level of detail has been invaluable for calculating mRGC volume (and all other quantifications dependent on this), bead volume, and dendrite diameter. However, in terms of reconstructing the branching

pattern of the mRGCs, it is unnecessary to fully segment all miniSOG-labeled processes. Instead, using open-contour lines to skeletonize mRGC processes would only take ~100 hours, or one observer working full time on this task for two weeks.

In terms of just acquiring the general outline of mRGCs in a volume, auto-segmentation can greatly accelerate the reconstruction of the miniSOG-labeled mRGCs found in those volumes (Figure 3.26). For example, combining the contiguous auto-segmented objects pertaining to a single mRGC only takes about 20 hours for an experienced observer. However, the compiled auto-segmented mRGC is unusable for volume calculations. Depending on what structures, like blood vessels and other miniSOG-labeled processes, lie in the path of the blue light used to photo-oxidize miniSOG during tissue preparation, the miniSOG label in mRGCs can be variable. Since all auto-segmentation protocols are built around thresholding pixels for darkness and then filtering auto-segmented contours for size (too big and the finer processes are not segmented, too small and there are too many false positives), the auto-segmented objects are irregularly shaped (which affects surface area and volume measurements and requires time to manually correct) and very disjointed (requiring many additional manually traced contours to connect auto-segmented objects). The time required to manually correct an auto-segmented miniSOG-labeled mRGC is currently greater than manually segmenting alone.

Considering the even distribution of all cell types across the mouse retina, future use of the miniSOG-label in mRGCs for SBEM should consider

dividing the surface area of the volume into grids and completely segmenting all miniSOG-labeled processes in only an evenly-spaced sampling of grids with open-contour skeletons throughout the entire volume to reconstruct all mRGC processes. Alternatively, one can imagine an improved auto-segmentation protocol that adds additional post-processing steps of smoothing all contours and/or warping auto-segmented contours into convex shapes that are bounded by locally-detected edges.

3.5.5 The past, present, and future

Our efforts to reconstruct mRGCs and their presynaptic partners in 3D have yielded 9 segmented mRGCs, over 100 presynaptic bipolar and amacrine cells, and a 0.44 mm^3 block of IPL that has been fully segmented for mRGC processes. Since we were not able to follow all marked synapses on every mRGC, the catalog of presynaptic partners that we have gathered for each mRGC subtype represents the minimum cell types that a particular mRGC subtype interacts with in the retina.

Our reconstructions of presynaptic partners verifies all claims that ON-bipolar cells make ectopic *en passant* synapses with OFF-stratifying mRGC synapses and allows us to extend that claim to M3 mRGCs. Our reconstructions also verify that OFF-stratifying mRGC dendrites synapse with dopaminergic amacrine cells (Joo et al. 2013). Also, we show that rod bipolar cells do, indeed, make direct connections with mRGCs in the ON-sublamina, like seen in Østergaard, Hannibal, and Fahrenkrug 2007, but also sometimes

from their axons in the OFF-sublamina.

More important than corroborating immune-EM or immunohistochemistry papers from the past, our studies identify the exact bipolar cell types and identify some amacrine cell types for each subtype of mRGC. Thus far, our findings show that M1 mRGCs receive input from all bipolar cell types (except for type 9 cone bipolar cells), dopaminergic amacrine cells, AII amacrine cells, and many other narrow field amacrine cells. In total, we segmented 20 bipolar cells and 12 amacrine cells that were presynaptic to V1_blue, the M1 mRGC.

Although we made an attempt to follow back each contour presynaptic to the M2, we were only able to reconstruct 6 bipolar cells (3 rod, 3 type 6) and 1 amacrine cell that we believe to be an A13.

From the bistratified M3 mRGC, we backtraced 16 bipolar cells representing cone bipolar types 2, 3, 5, 6, and 7, and rod bipolar cells. We also backtraced 10 amacrine cells, some of which show similar morphology to Flag/NO type, A1, and A5 amacrine cells.

M4 mRGCs receive input from all type 6, 7, 8, and rod ON-bipolar cell types. In total, we reconstructed 24 bipolar cells that make synapses with V1_green, the M4 subtype mRGC. Because M4 dendrites never make their way to the OFF- sublamina, no OFF-cone bipolar cells synapse with the M4. Unfortunately, we were unable to trace any amacrine cells back to a cell body. Since the reconstructed neurons represent the minimum number of retinal cell types that synapse with the M4, our lack of identifying an amacrine cell that interacts with M4 does not necessarily mean that M4 mRGCs do not receive

input from amacrine cells. In fact, many fine mono-stratifying processes, unlike those found on bipolar cells, were found making synapses on the M4. However, because of the depth at which M4 processes ramify in the IPL and the fine caliber of these putative amacrine cell processes, the amacrine cell processes are lost before being able to be connected to an amacrine cell body.

Similar to the M4, we were also unable to connect contours presynaptic to V3_left, the M5 mRGC, back to amacrine cell bodies. In total, we reconstructed 28 bipolar cells and 18 amacrine cell processes from the terminals presynaptic to the M5 mRGC. Among the 28 bipolar cells, 10 were rod bipolar cells, 8 were type 6, 6 were type 7, 4 were type 8. Here we can see a nice example of the stratification-dependent input from bipolar cells in that M4 mRGCs stratify in strata 4 of the ON-sublamina and M5 mRGCs stratify in strata 5, which is closer to the GCL. Type 8 cone bipolar cells stratify in strata 5. As such, the M4 is post-synaptic to fewer type 8 cone bipolar cells than the M5 which fasciculate in the same strata as the type 8 cone bipolar.

Future directions for these studies may be to use different correlated light and electron labels that will allow for the visualization of the plasma membrane in so that post-synaptic densities can be visualized. Also, marking synapses, calculating synaptic density, and backtracing presynaptic cells from the miniSOG-labeled mRGC processes in the fully segmented block will allow for comparisons of synaptic density and presynaptic players in distal dendrites to the synaptic densities and presynaptic players thus reported here for the proximal dendrites of an mRGC.

Chapter 3 is currently being prepared for submission for publication of the material. Liu, Cindy Yu Hsin; Kim, Keunyoung; Rios, Luis; Garcia, Guadalupe; Ellisman, Mark; Panda, Satchidananda. I am the primary investigator and first author of this material. Keunyoung Kim performed the tissue preparation, electron microscopy, and image processing. Luis Rios contributed some help with the data analysis. Guadalupe Garcia was a tremendous help with the automatic segmentation. Mark Ellisman and Satchidananda Panda directed and supervised the research.

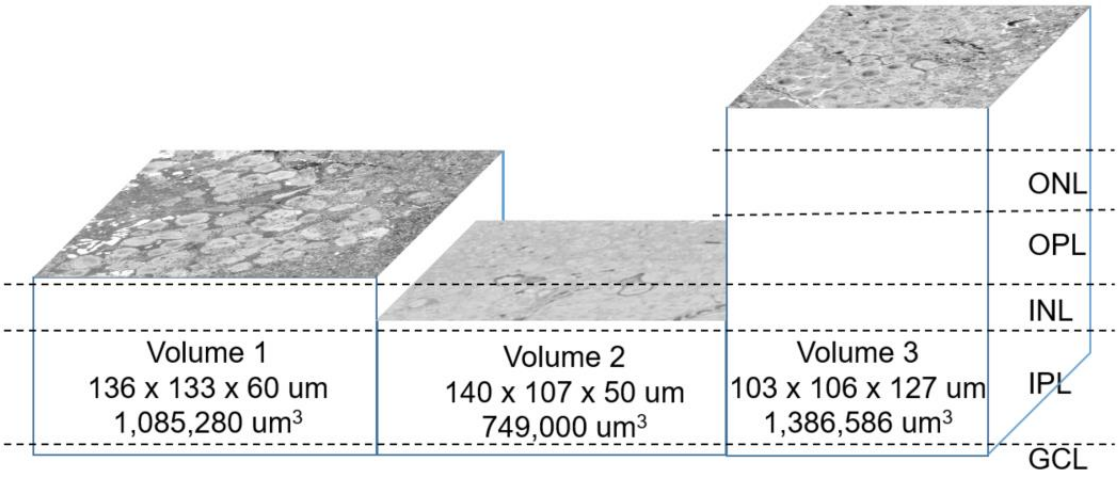

Figure 3.1 Retinal volumes used in this study

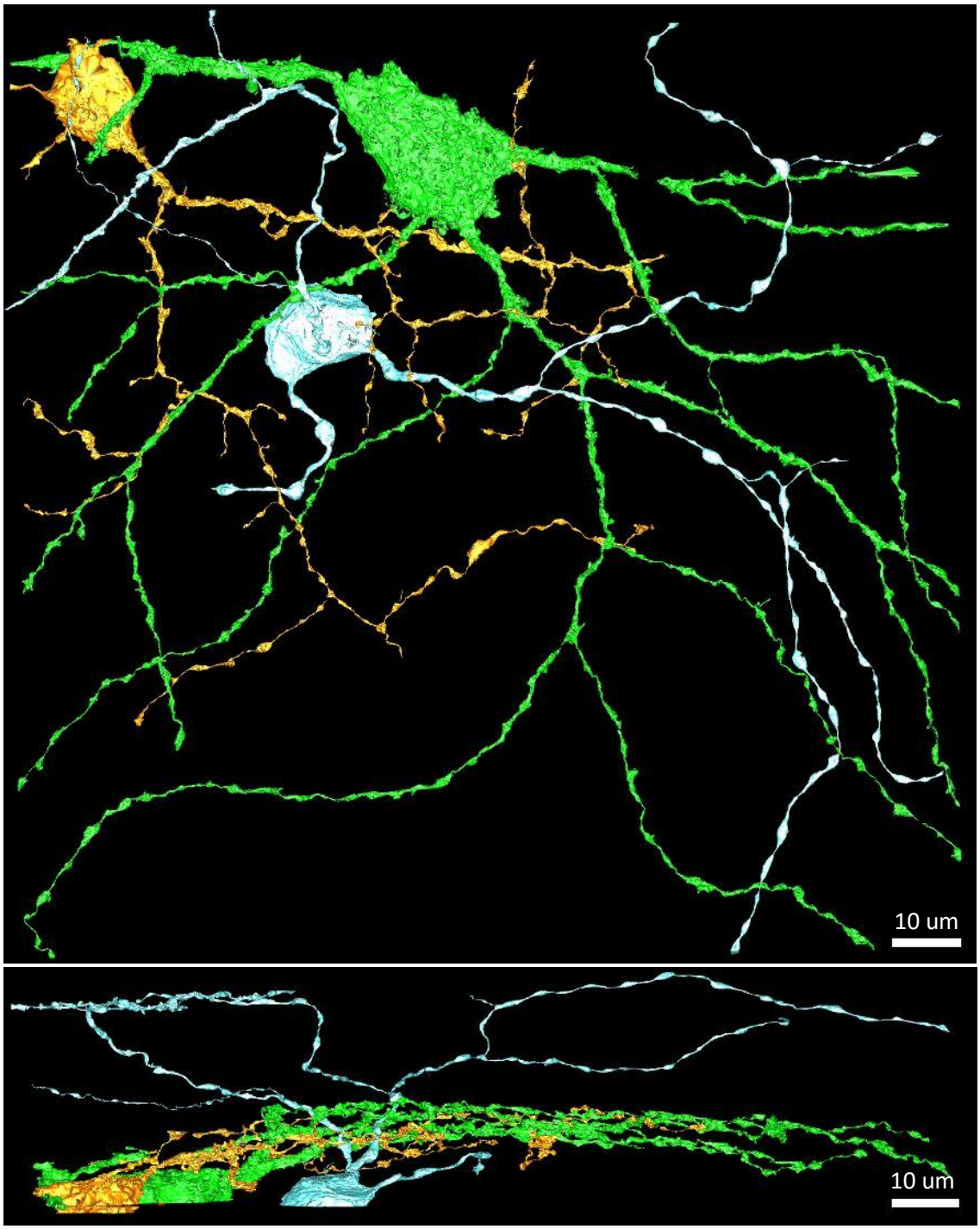

Figure 3.2 Volume_1

Top: *En face* view of retinal surface area showing segmented mRGCs from Volume_1. Bottom: Cross-sectional view showing dendrites stratifying in IPL.

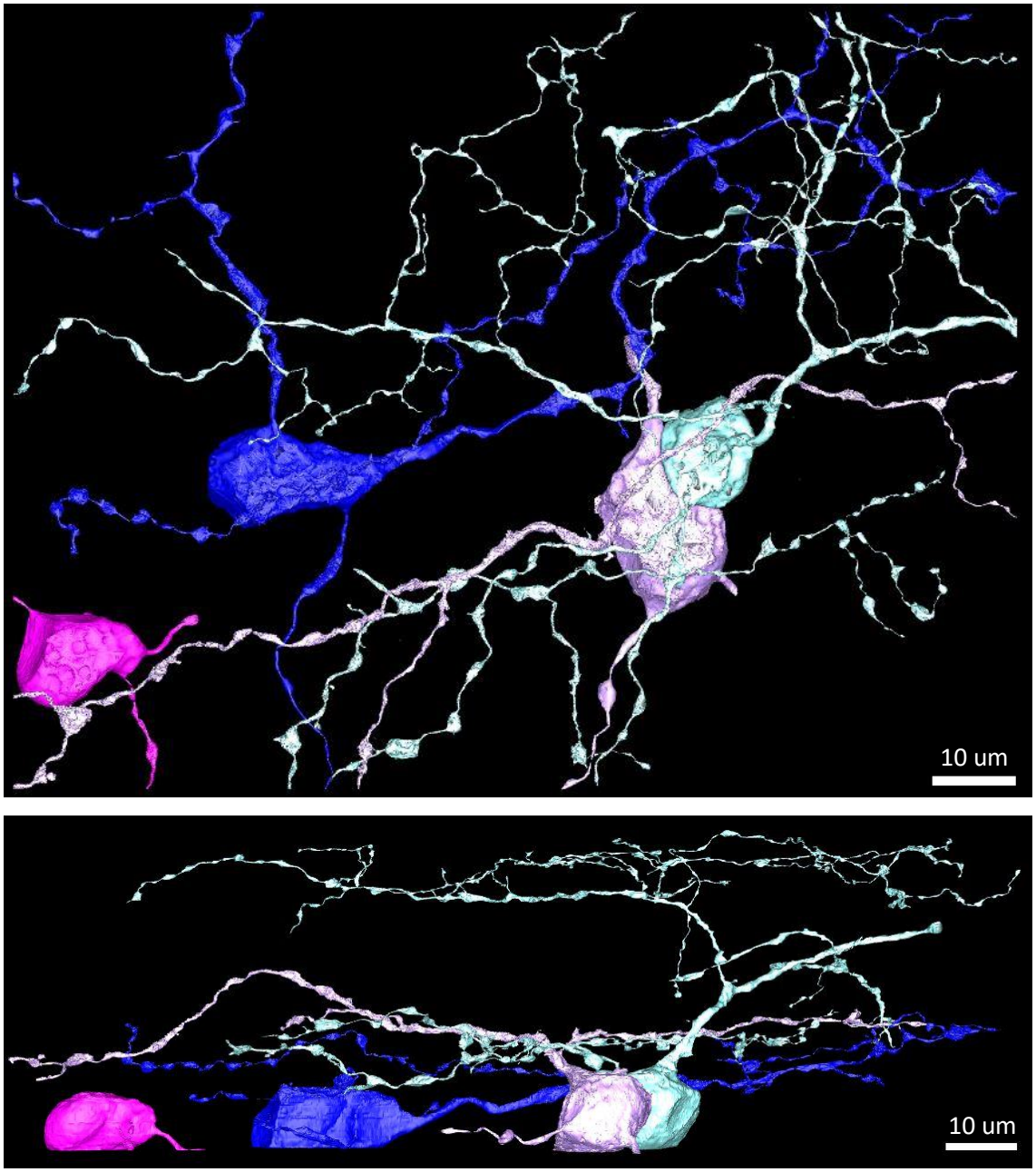

Figure 3.3 Volume_2

Top: *En face* view of retinal surface area showing segmented mRGCs from Volume_2. Bottom: Cross-sectional view showing dendrites stratifying in inner plexiform layer.

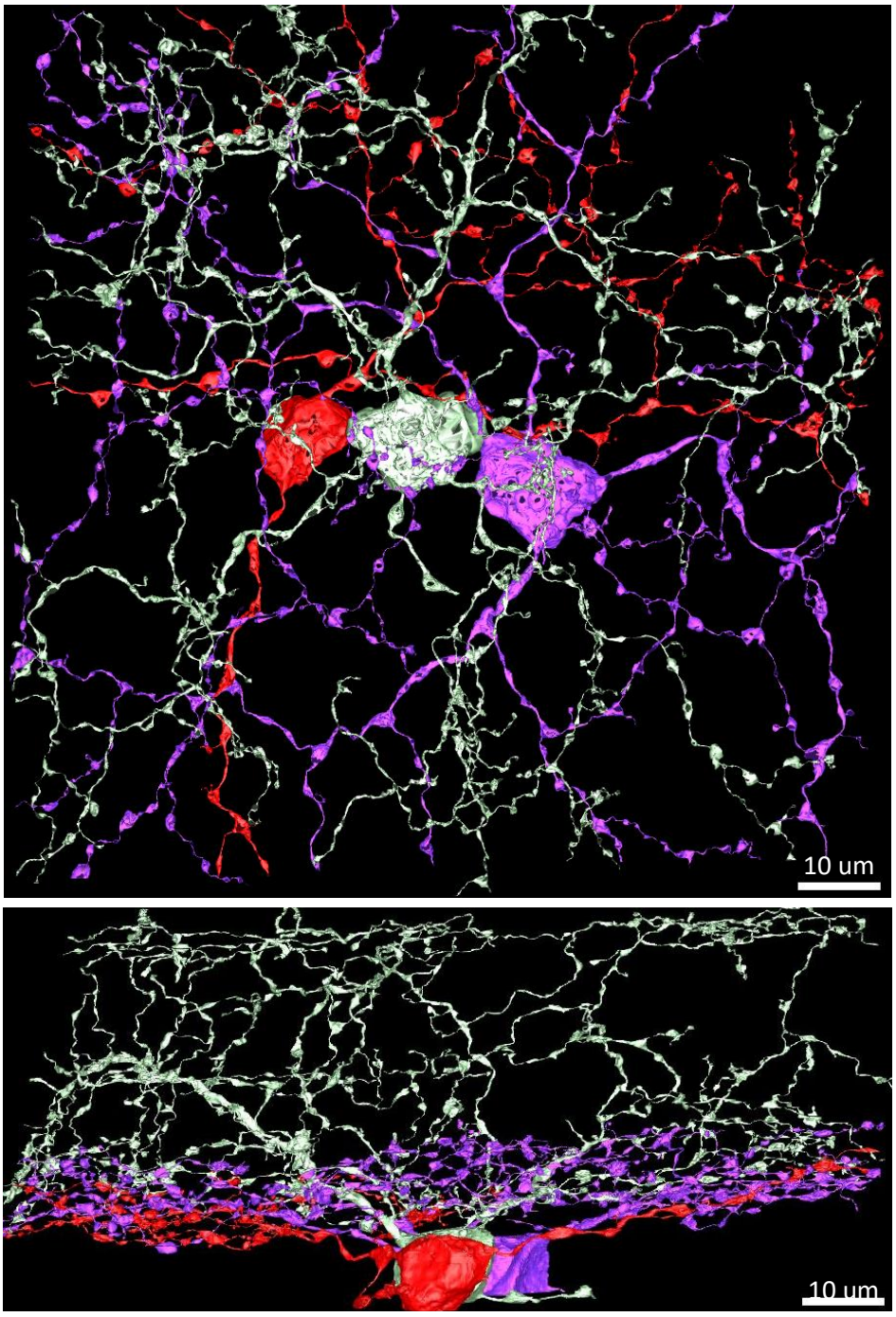

Figure 3.4 Volume_3

Top: *En face* view of retinal surface area showing segmented mRGCs from Volume_3. Bottom: Cross-sectional view showing dendrites stratifying in inner plexiform layer.

	V1_ green	V1_ blue	V1_ orange	V2_ dBlue	V2_ lavender	V2_ lBlue	V3_ left	V3_ mid	V3_ right
subtype	M4	M1	M5	M2	M4	M3	M5	M3	M2
diameter	23.79	13.97	13.81	16.80	17.27	11.55	10.83	14.81	14.25
synapses	525	218	383	178	118	402	155	924	225
synapses/ 10 um	4.03	3.66	4.12	3.33	4.17	2.65	2.20	3.00	1.41
beads	122	76	131	68	27	181	152	918	416
beads/ 10 um	0.94	1.28	1.41	1.27	0.95	1.19	2.16	2.99	2.61
synapses: beads	4.30	2.87	2.92	2.62	4.37	2.22	1.02	1.01	0.54
number of branches	18	11	41	11	8	70	37	236	91
branches/ 100 um	1.38	1.85	4.41	2.06	2.83	4.62	5.26	7.67	5.70

Figure 3.5 Quantification of mRGC morphology

From mRGCs segmented from the three retinal volumes.

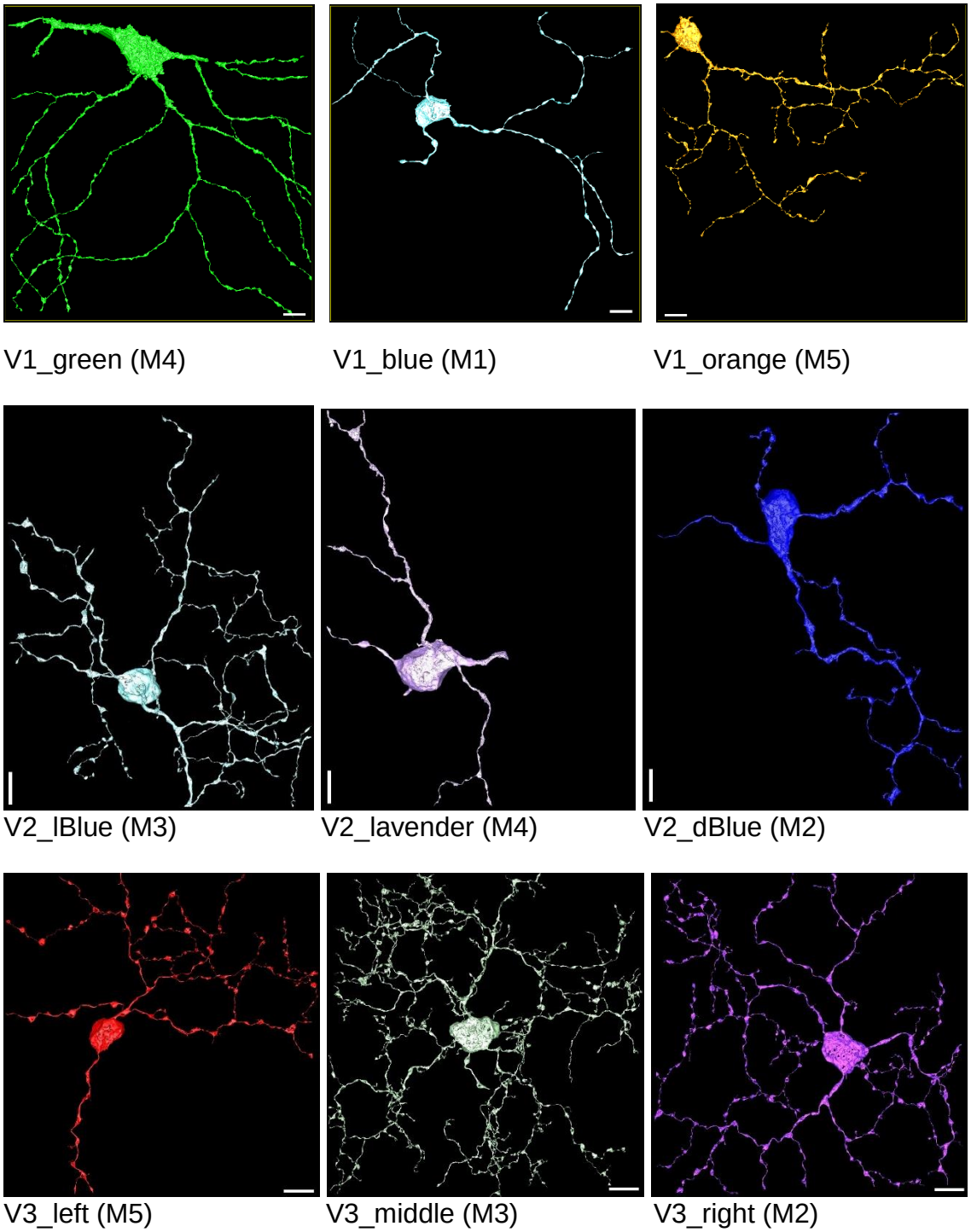

Figure 3.6 mRGCs segmented from the three retinal volumes

Top: mRGCs segmented from Volume_1. Middle: mRGCs segmented from Volume_2. Bottom: mRGCs segmented from Volume_3. Scale bar is 10 um.

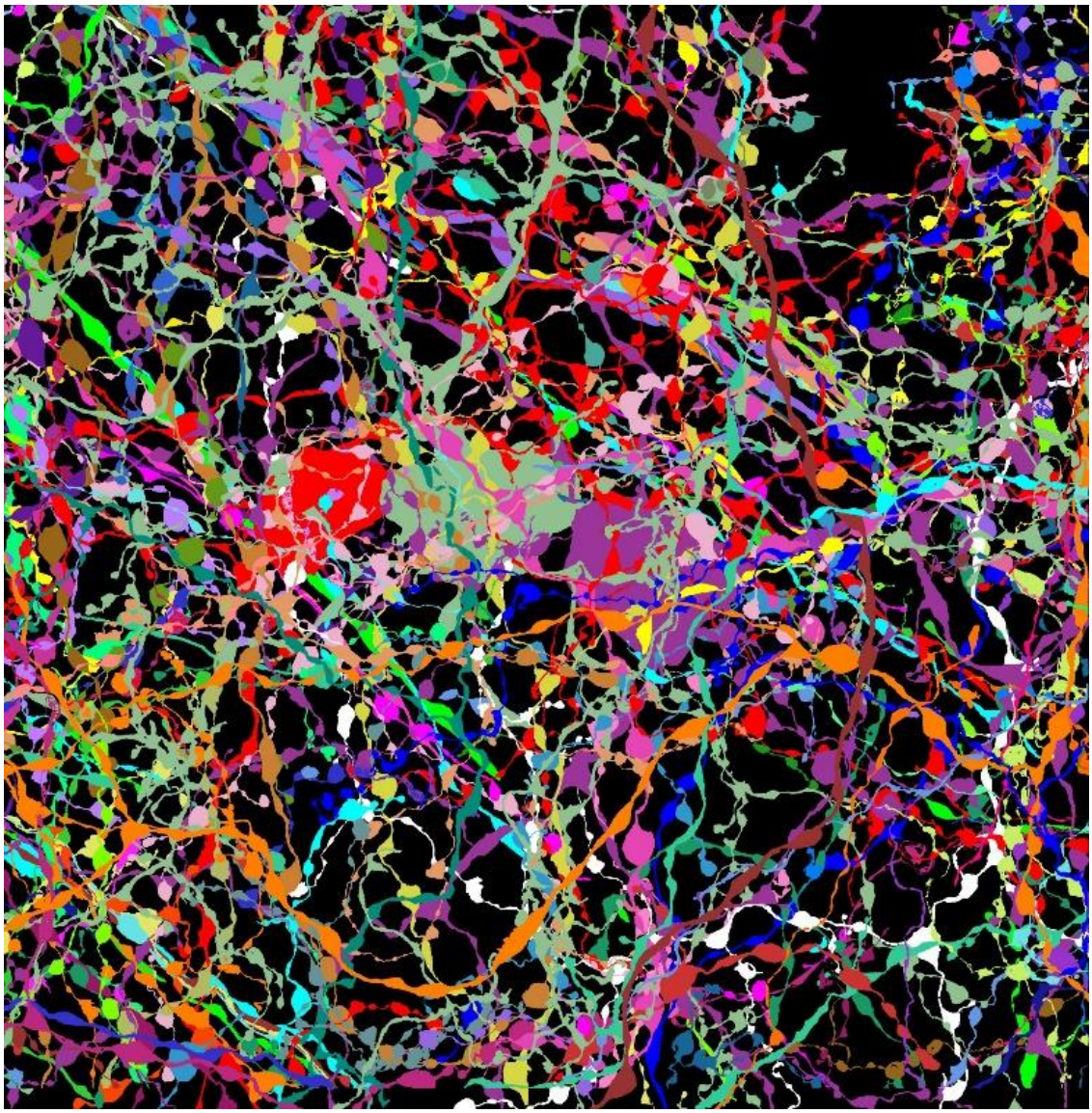

Figure 3.7 Fully segmented miniSOG-labeled mRGC processes

En face view of fully segmented miniSOG-labeled mRGC processes from 92 x 92 x 51 um thick block of retinal tissue. Each color represents a separate mRGC process.

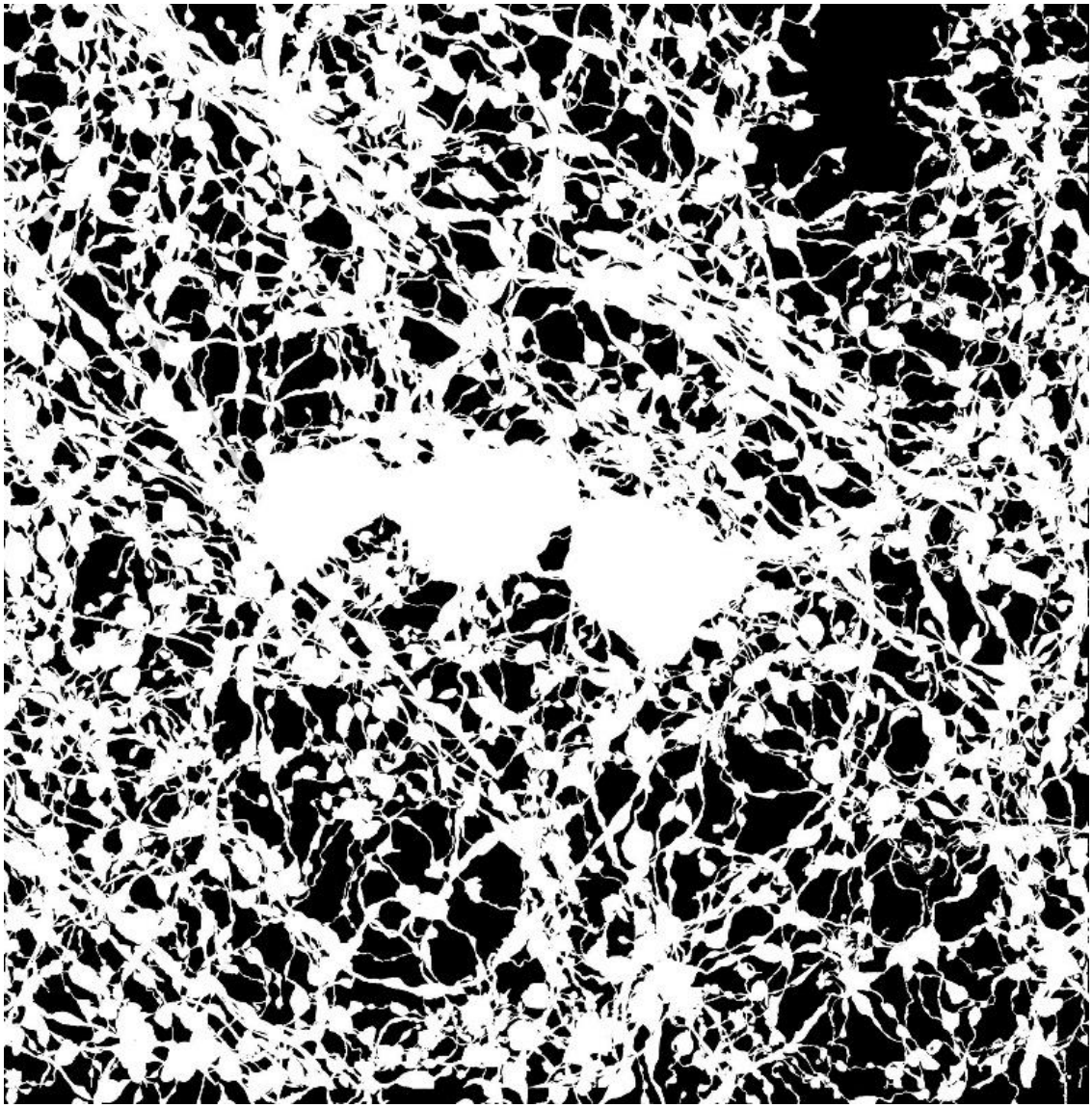

Figure 3.8 Retinal surface area covered by mRGCs

Completely segmented Volume_3 with all objects set to white color; total pixels = 3,800,340, white pixels = 2,147,464. % surface area covered by mRGCs= 56.5%

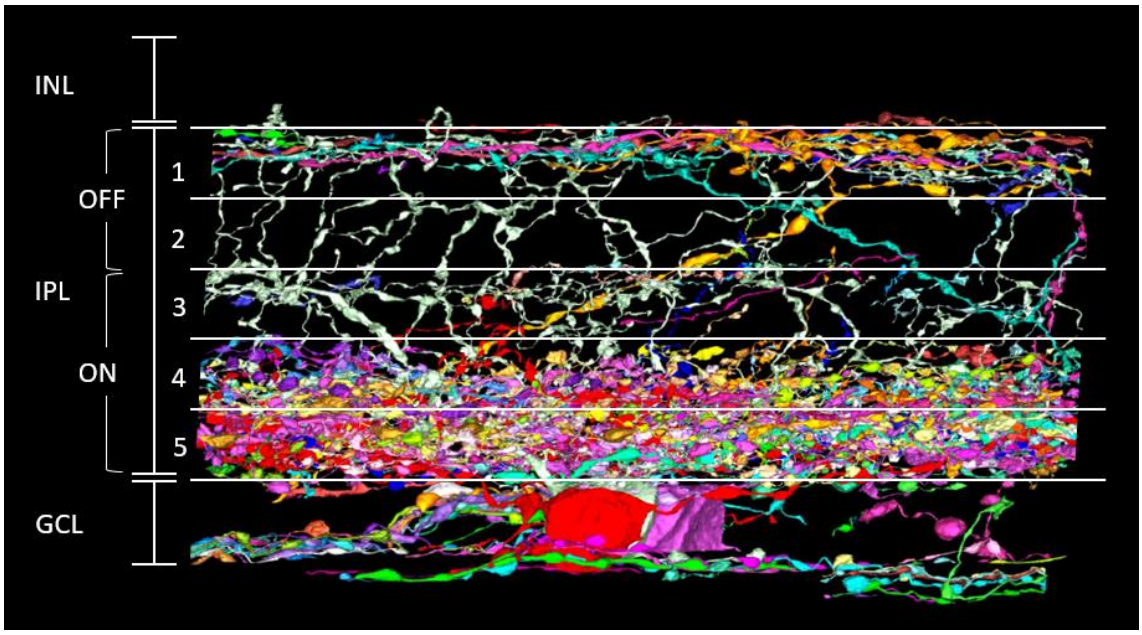

Figure 3.9 Cross-sectional view of fully segmented mRGC processes

Cross-sectional view. Block dimension is 92 x 92 x 51 um. There are no miniSOG-labeled mRGC processes in the inner nuclear layer (INL). All miniSOG-labeled dendritic processes stratify in the inner plexiform layer (IPL) with 84% of processes stratifying in strats 4 and 5 of the ON-sublamina (ON) and only 6.6% of all processes stratifying in the OFF-sublamina (OFF). The cell bodies of the three mRGCs in this volume are located in the ganglion cell layer (GCL).

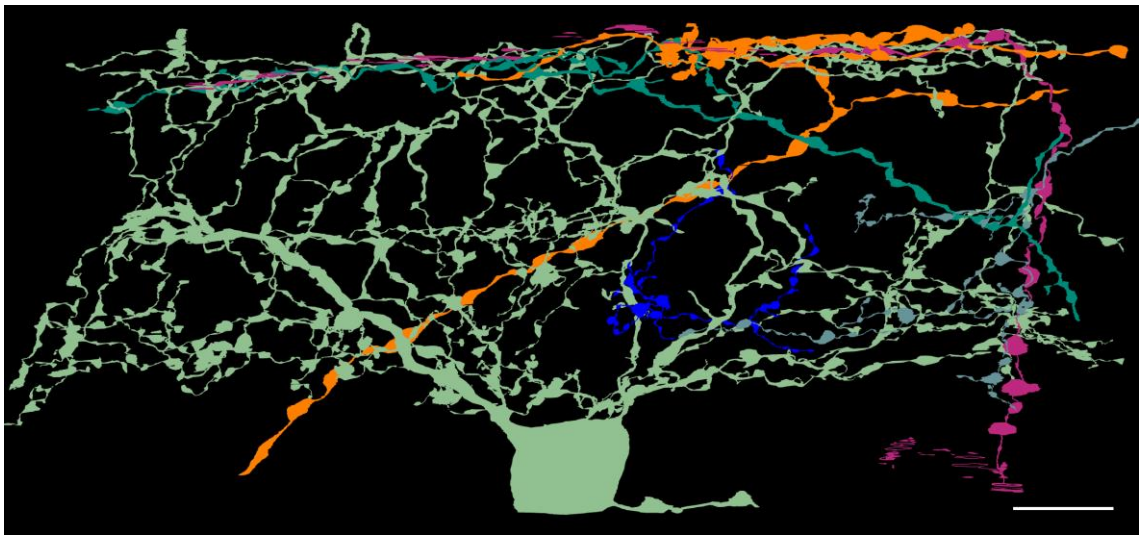

Figure 3.10 mRGC processes that span IPL

Green: M3 mRGC. Orange: M1 dendritic process. Magenta: ectopic axonal projection.

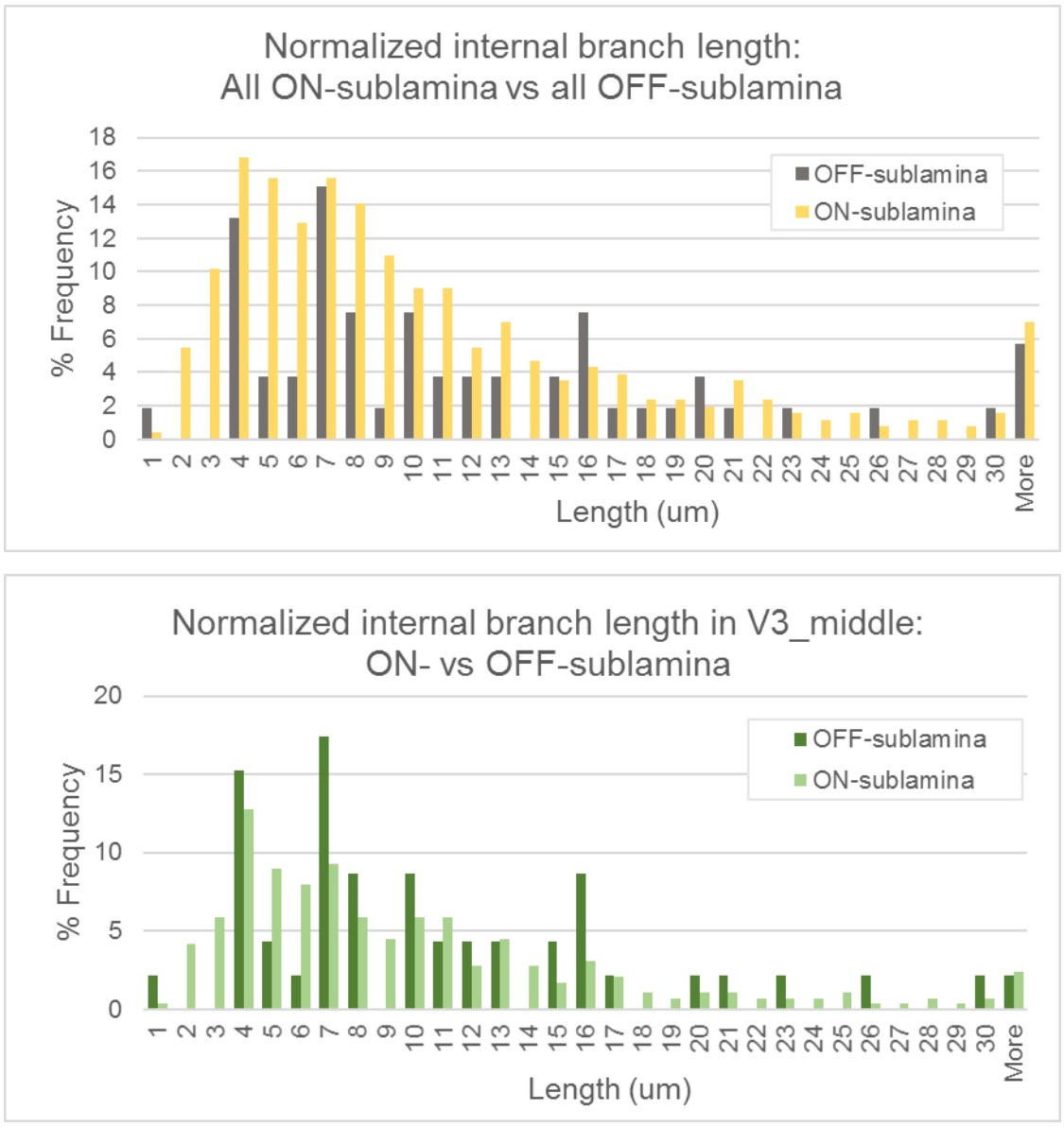

Figure 3.11 Internal branch length, ON- vs. OFF-sublamina

Top: Internal branch lengths of all mRGC processes in ON- vs. OFF-sublamina. Bottom: Internal branch lengths of mRGC V3_middle in ON- vs OFF-sublamina.

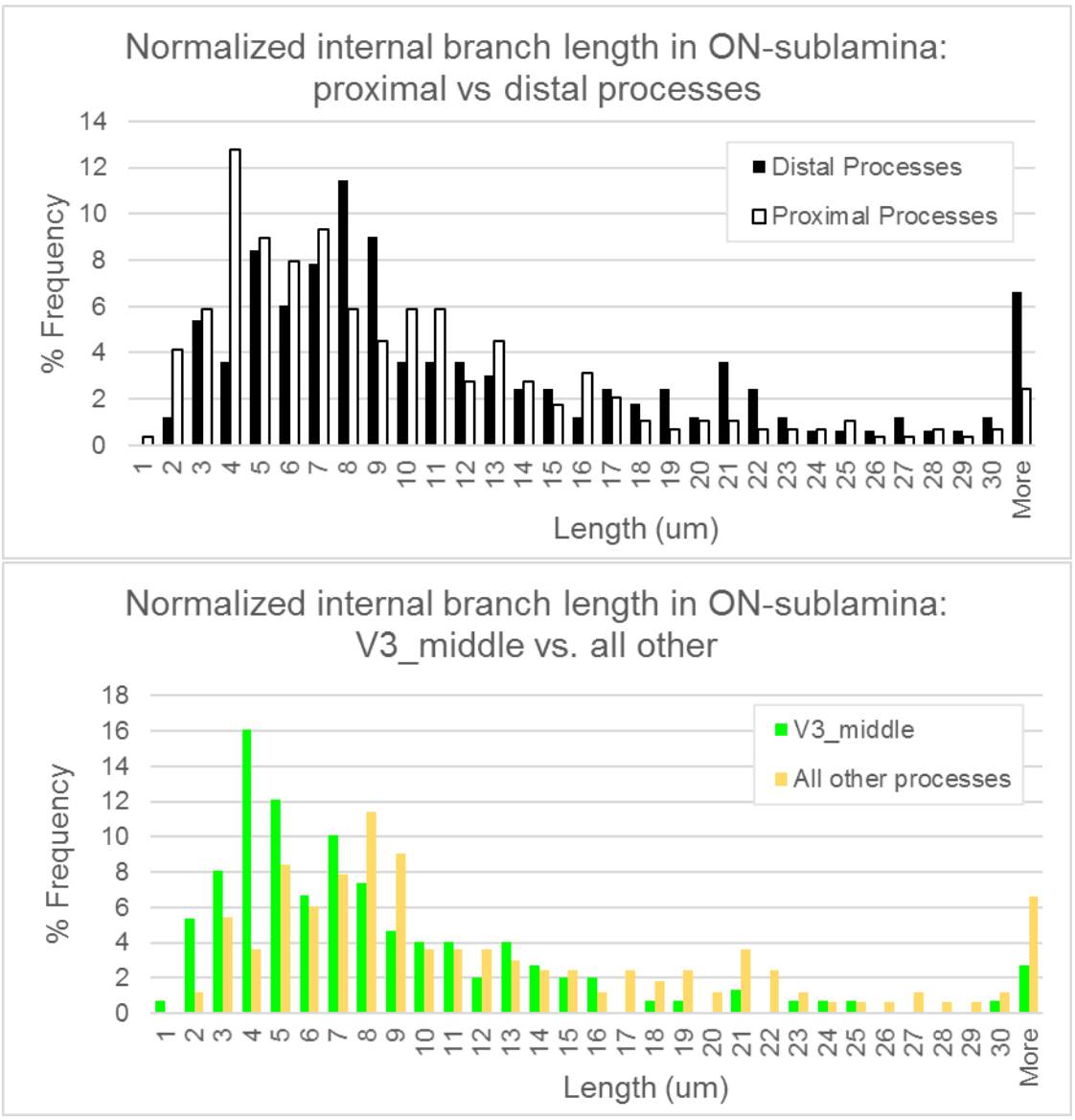

Figure 3.12 Internal branch length, ON-sublamina

Top: Internal branch lengths of distal (all processes not connected to a cell body in Volume_3) vs proximal processes (those connected to a cell body in Volume_3) in ON-sublamina. Bottom: Internal branch lengths of mRGC V3_middle processes vs all other mRGC processes in ON-sublamina.

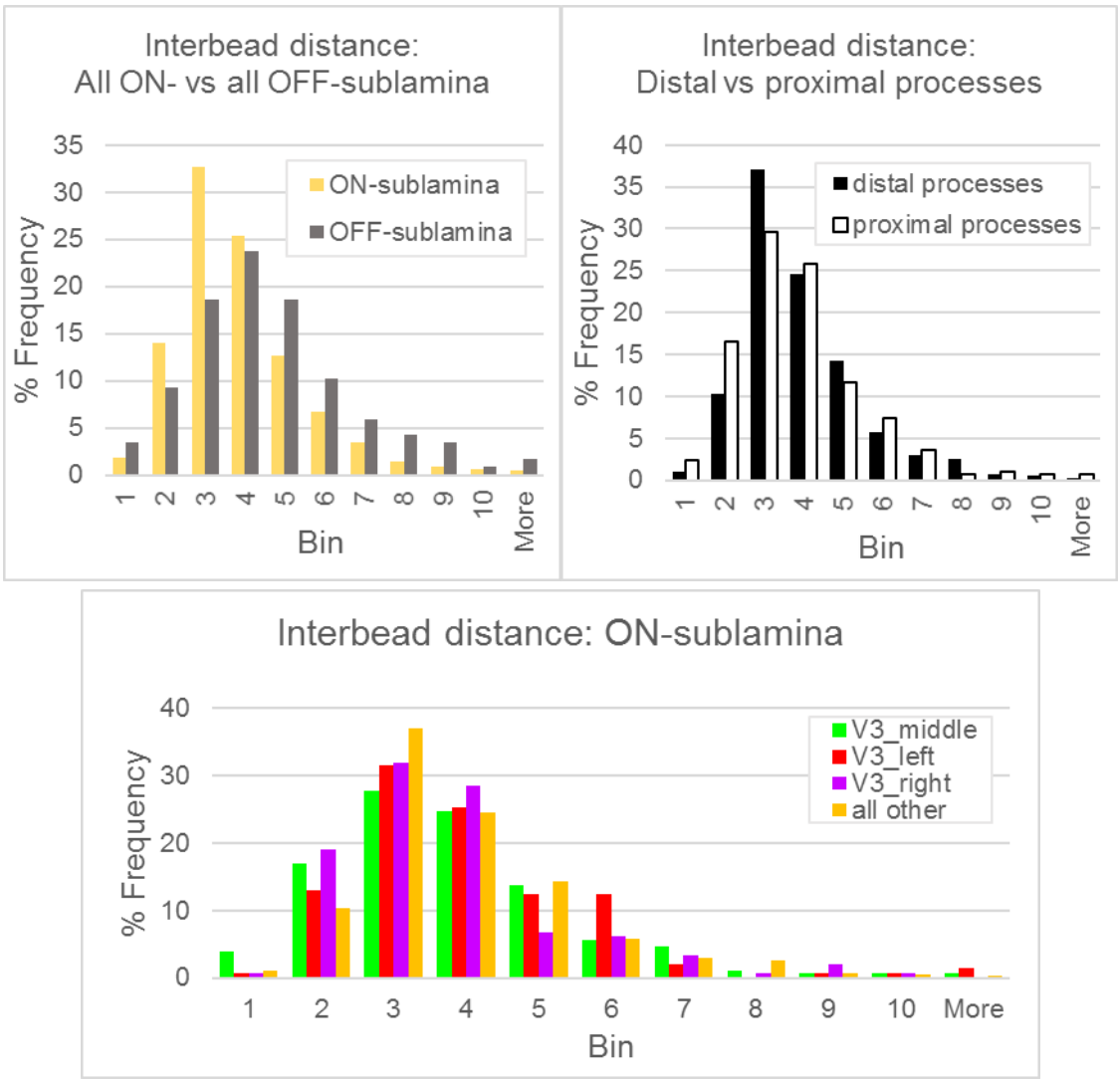

Figure 3.13 Interbead distance

Average distances between beads. Top, left: Interbead distances of all mRGC processes in ON- vs OFF-subalmina. Top, right: Interbead distances of all distal (all processes not connected to a cell body in Volume_3) vs proximal processes (those connected to a cell body in Volume_3) in ON-sublamina. Bottom: Interbead distances of mRGC processes in ON-sublamina comparing mRGC subtypes to all processes in ON-sublamina

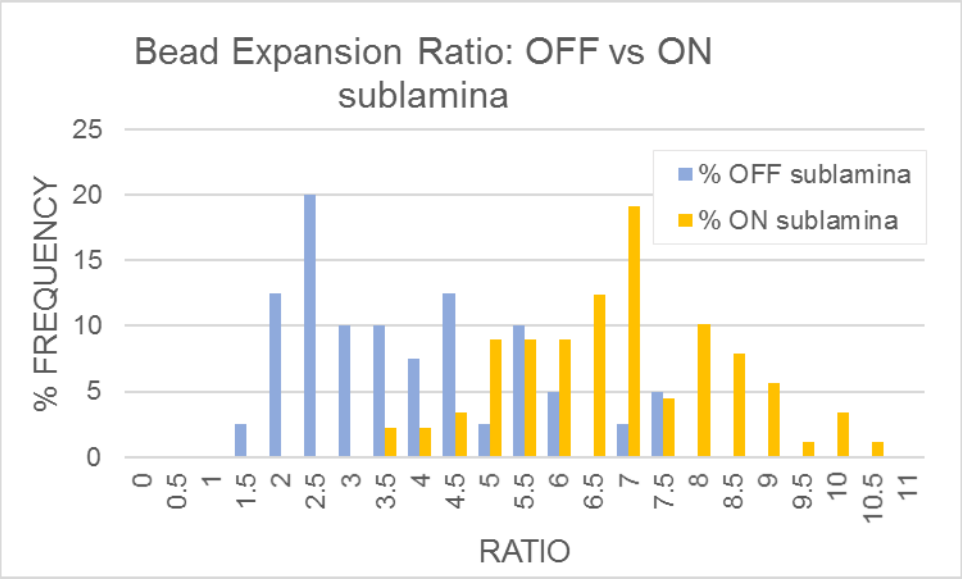

Figure 3.14 Bead-expansion ratio, ON- vs. OFF-sublamina

Bead-expansion ratio (ratio of bead diameter to base dendrite diameter) of mRGC processes in ON- vs. OFF-sublamina.

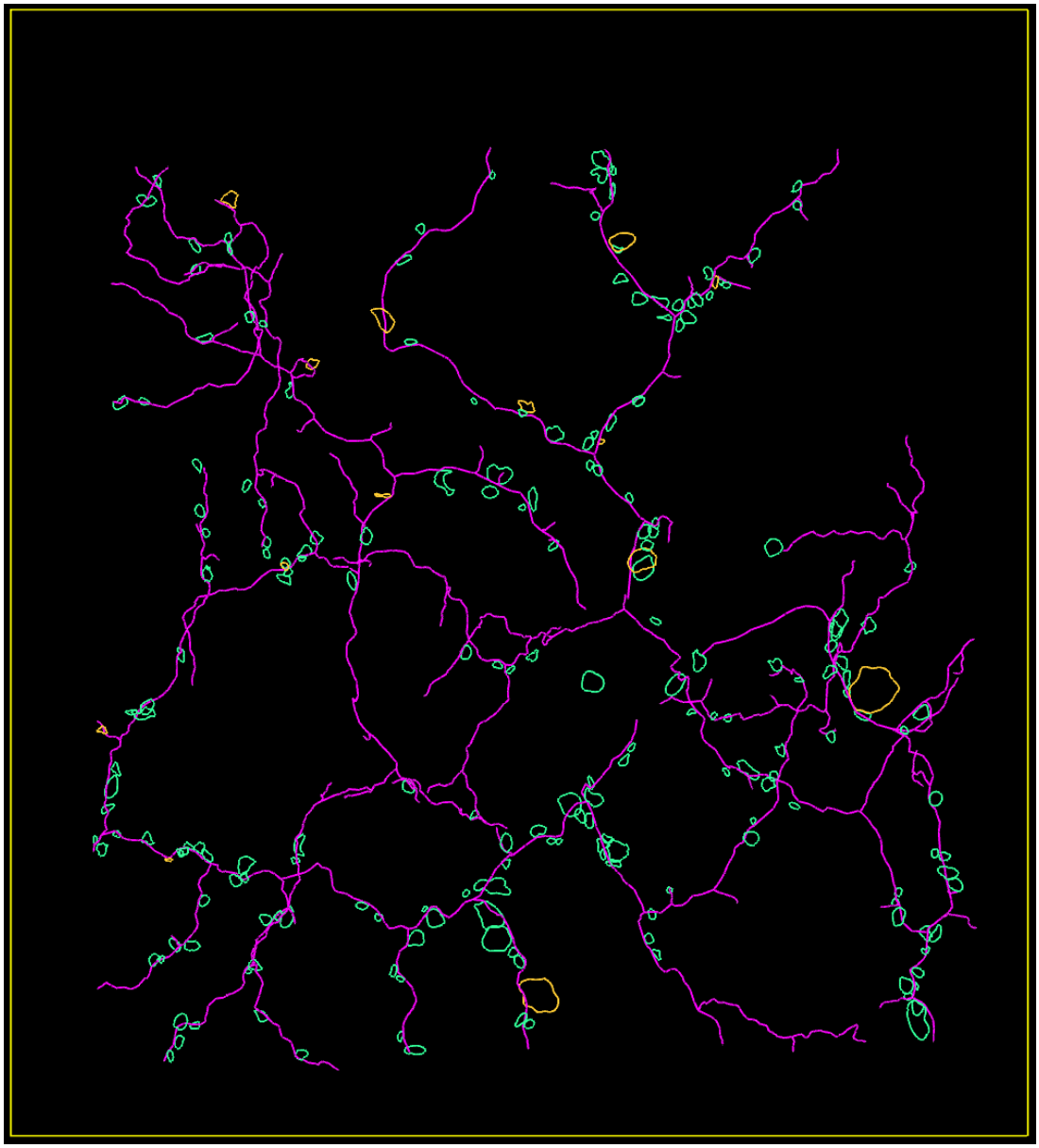

Figure 3.15 All synapses marked on an mRGC

All synapses marked on mRGC V3_right from Volume_3. Purple is the skeleton of V3_right. All green contours are identified synapses that could not be followed back to a cell body. All orange contours are synapses that could be followed back to a cell body.

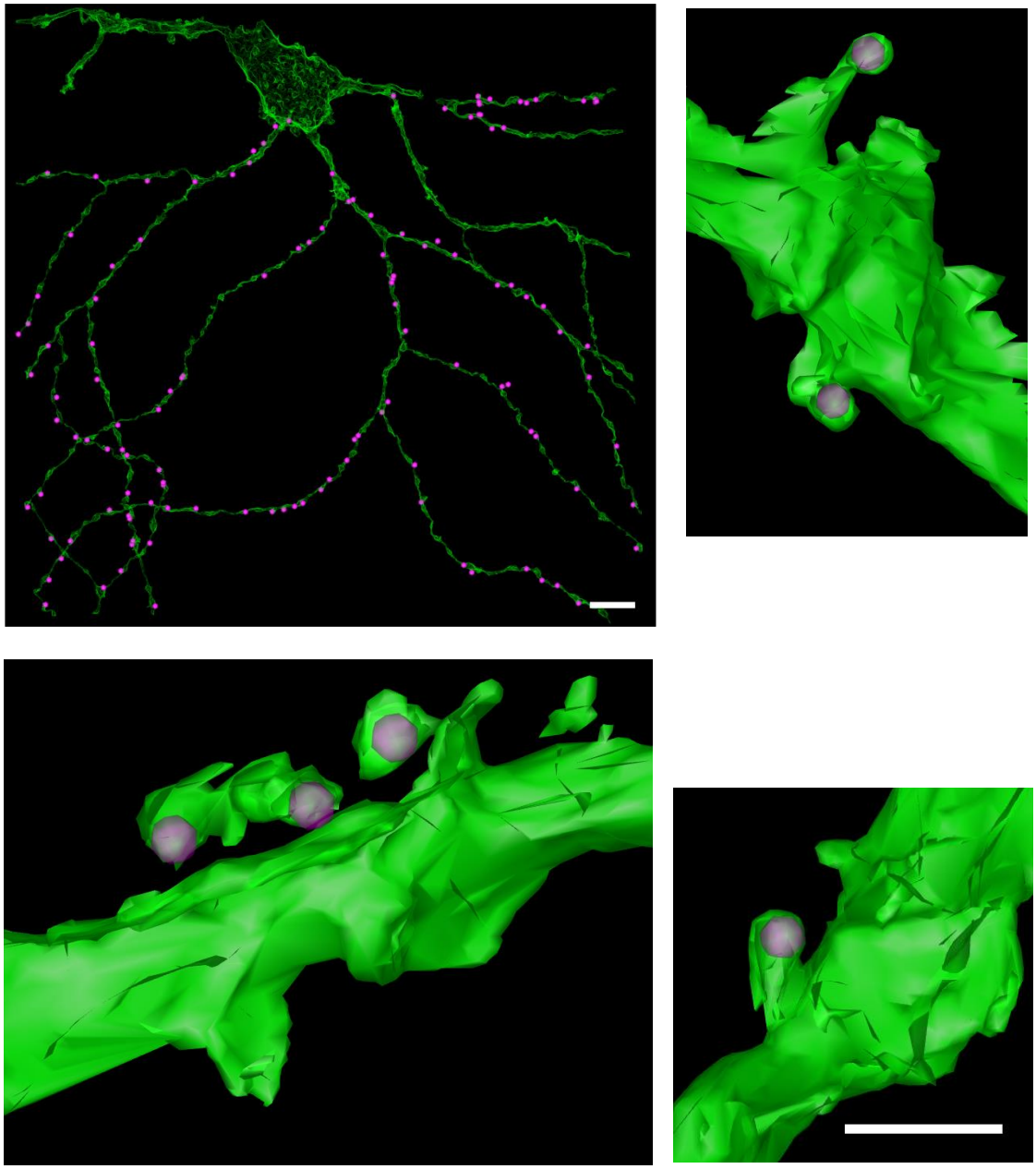

Figure 3.16 Cap synapses from V1_green

3D reconstructions of cap synapses (purple spheres) protruding from the dendrites of an V1_green, and M4 subtype mRGC in Volume_1. Scale bar in top left is 10 um. Scale bar in bottom right is 500 nm.

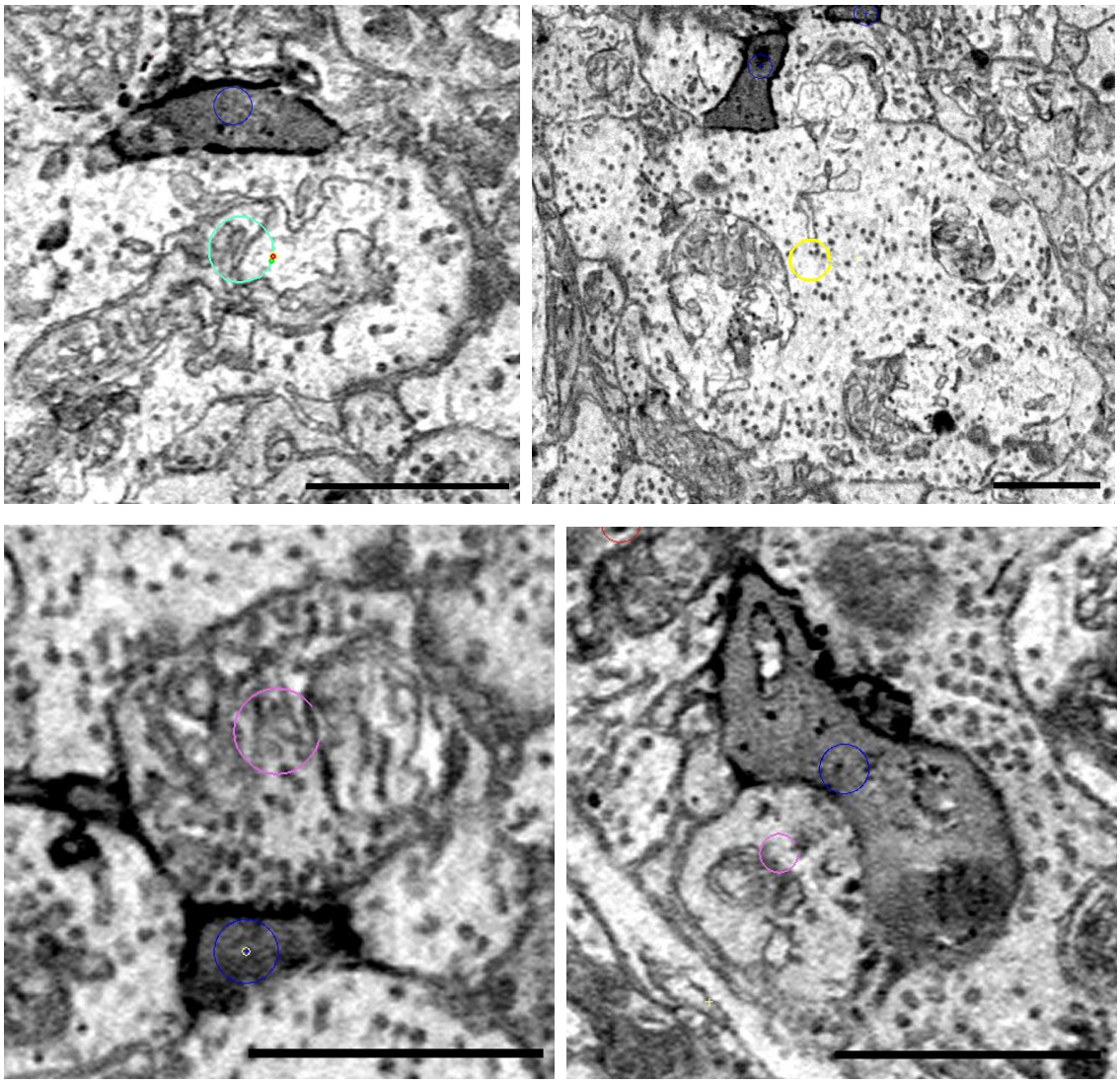

Figure 3.17 Synapses between bipolar cells and mRGC dendrites

Top, left: OFF-stratifying mRGC dendritic process (blue circle) is directly opposed to vesicles docked at the membrane of type 2 cone bipolar cell terminal (teal circle). Top, right: ON-stratifying mRGC dendritic process (blue circle) is directly opposed to vesicles docked at membrane of type 6 cone bipolar cell terminal (yellow circle). Bottom: mRGC interaction (blue circle) with bipolar cell axon (pink circle). Scale bar is 1 um.

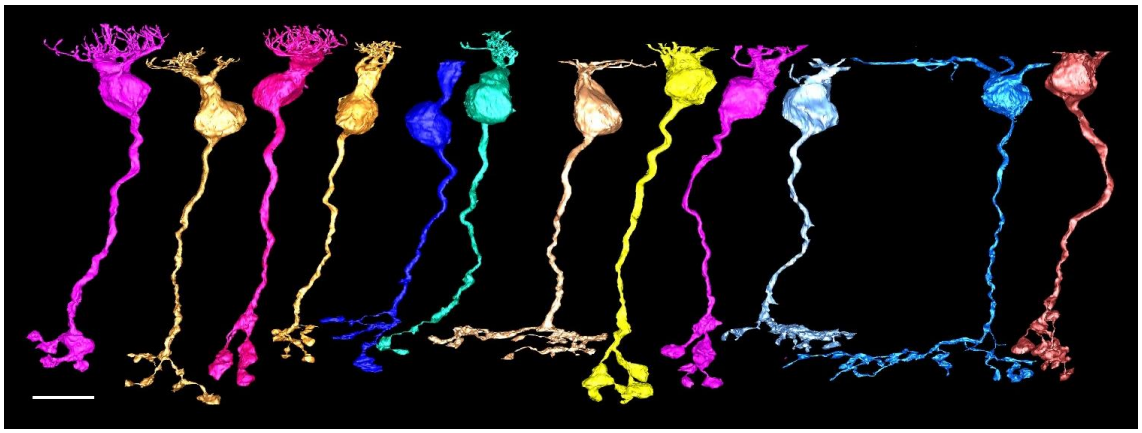

RBC CB6 RBC CB6 CB6 CB7 CB7 RBC RBC CB7 CB8 RBC

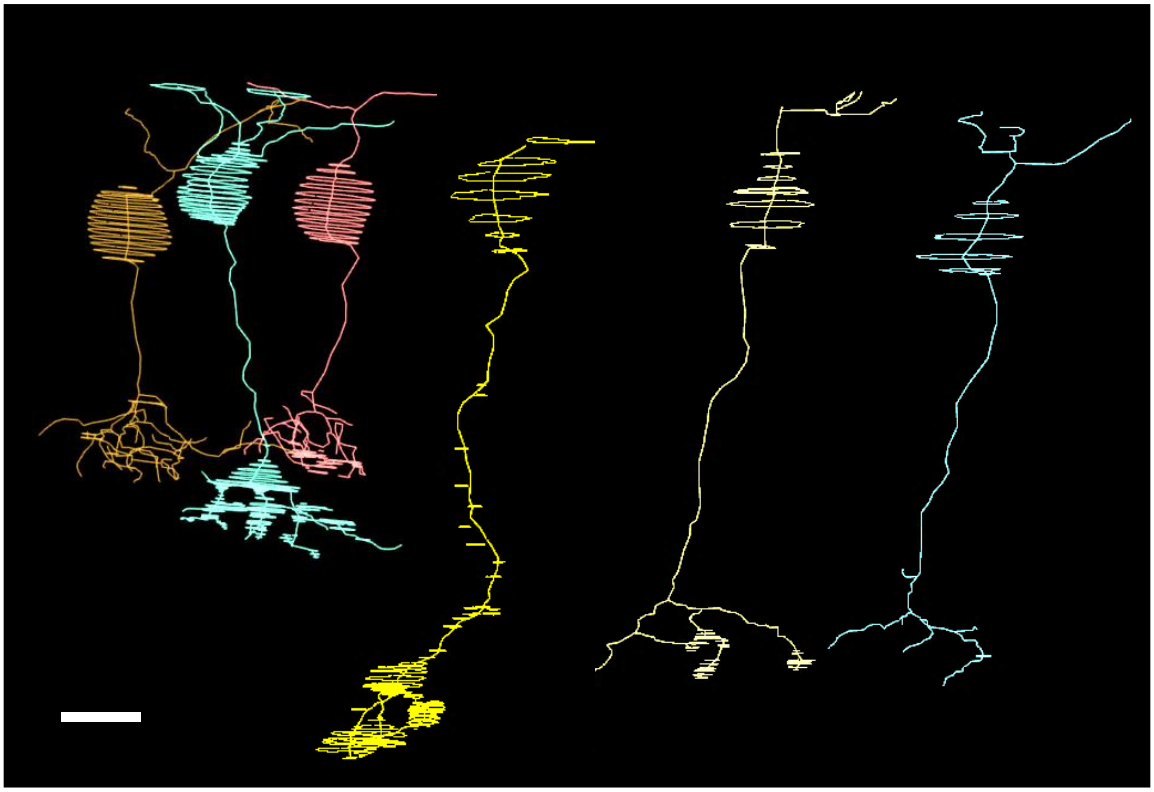

CB2 CB3 CB2 RBC CB7 CB7

Figure 3.18 Bipolar cells presynaptic to mRGCs

Examples of fully segmented and skeletonized bipolar cells that are presynaptic to mRGCs. Scale bar is 5 um.

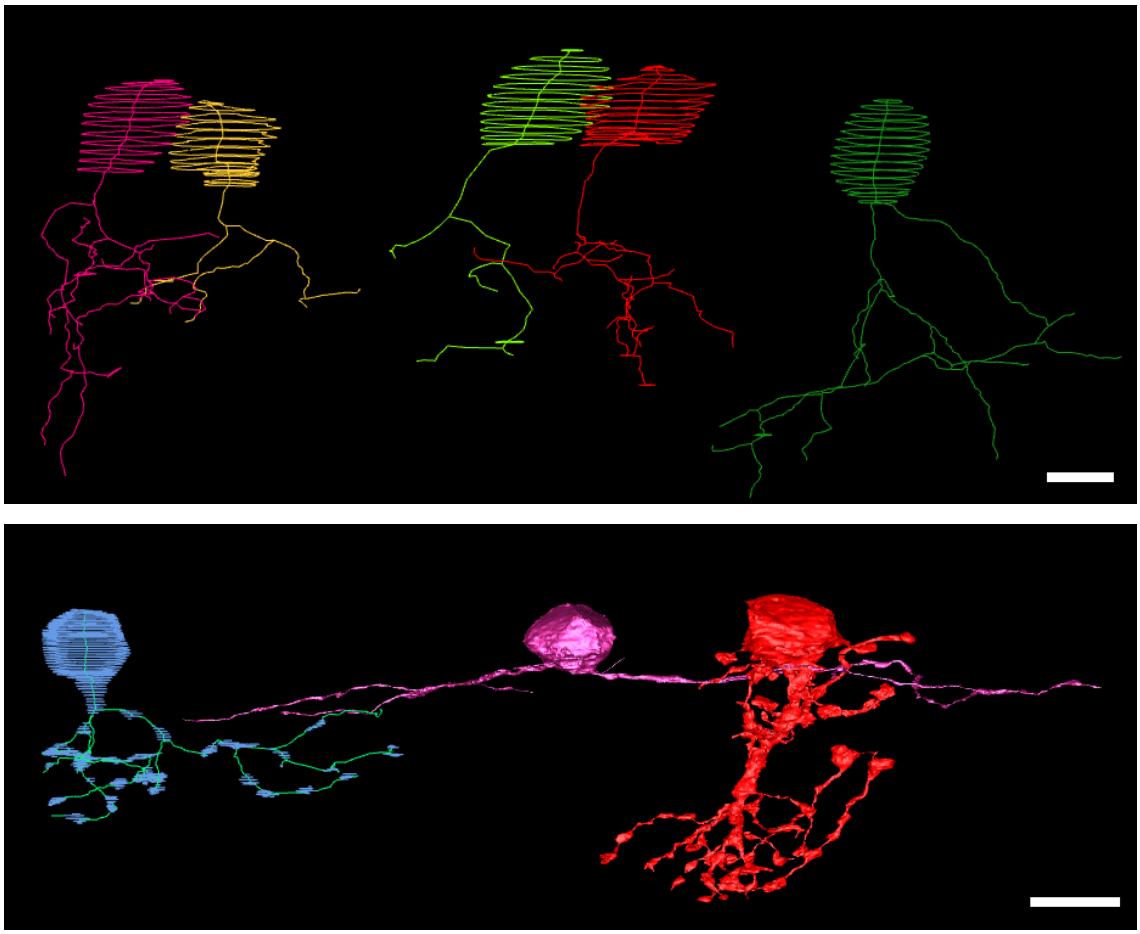

Figure 3.19 Amacrine cells presynaptic to mRGCs

Examples of fully segmented and skeletonized amacrine cells that are presynaptic to mRGCs. Scale bar is 5 um.

	M1	M2	M3	M4	M5
Stratification	OFF	ON	OFF/ ON	ON	ON
Bipolar cells	Total (20): Type 2 (2) Type 3 (2) Type 4 (2) Type 5 (1) Type 6 (5) Type 7 (1) Type 8 (1) Rod (6)	Total (6): Type 6 (3) Rod (3)	Total (16): Type 2 (3) Type 3 (1) Type 5 (2) Type 6 (2) Type 7 (6) Rod (1)	Total (24): Type 6 (15) Type 7 (2) Type 8 (1) Rod (6)	Total (28): Type 6 (8) Type 7 (6) Type 8 (4) Rod (10)
Amacrine cells	Total (12): Dopamine Flag/NO AII	Total (1): A13	Total (10): Flag/NO A1 A5	Could not follow to cell body	Could not follow to cell body

Figure 3.20 Cell types presynaptic to mRGCs

Cell types presynaptic to mRGCs segmented from Volume_1 and Volume_3. Because not every identified synapse could be backtraced to a cell body, the cell types and counts listed here are an underestimation of all possible types and counts. While no amacrine cells were able to be traced back to cell bodies for the M4 and M5, there are many amacrine cell processes that were observed for both M4 and M5.

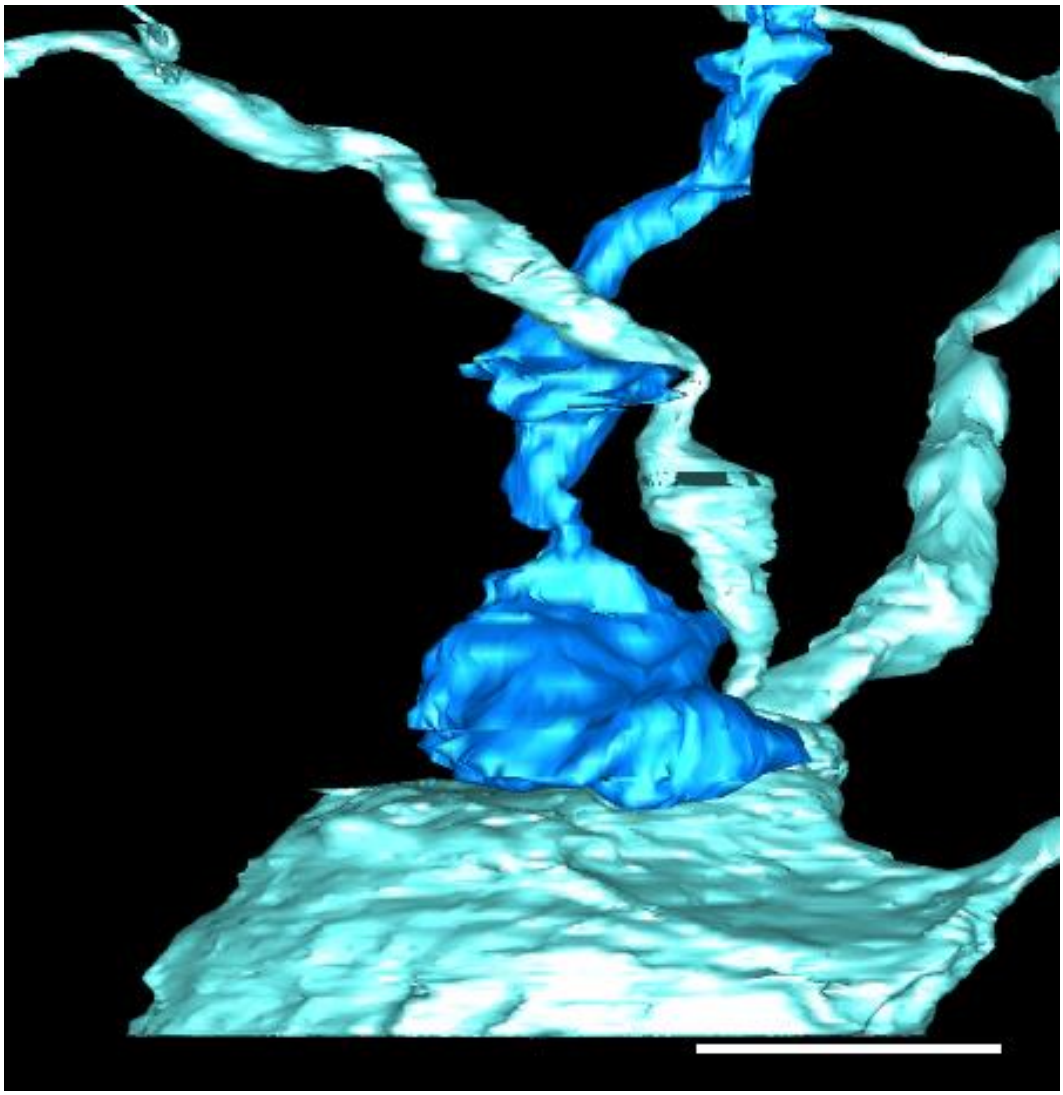

Figure 3.21 Rod bipolar cell to V1_blue (M1 subtype)

3D reconstruction of rod bipolar cell terminal (darker blue) in direct contact with cell body of V1_blue, an M1 subtype mRGC. Scale bar is 5 um.

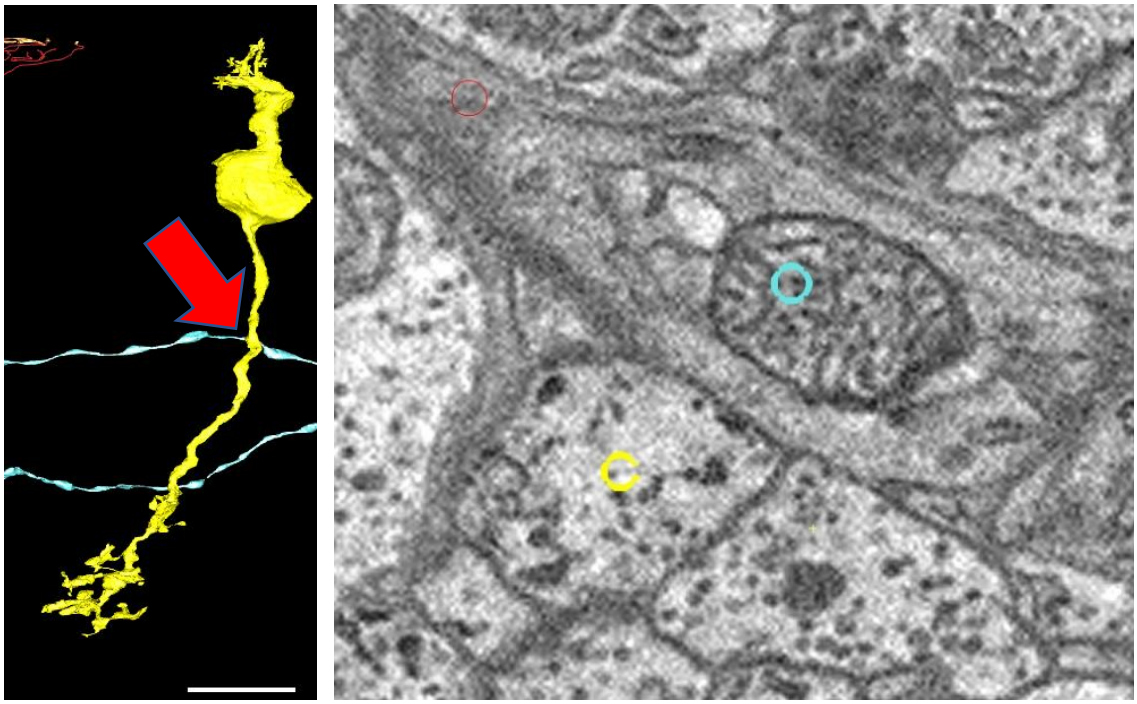

Figure 3.22 Ectopic ON-bipolar cell synapse in OFF-sublamina

Left: ON-bipolar cell (yellow) axon swells near contact point (red arrow) with OFF-stratifying M1 mRGC dendrite (light blue). Right: electron microscopy image showing contact between ON-bipolar cell axon (yellow circle) and mRGC dendrite (light blue circle). Note the vesicles in the bipolar cell axon docked at the membrane. Scale bar is 5 um.

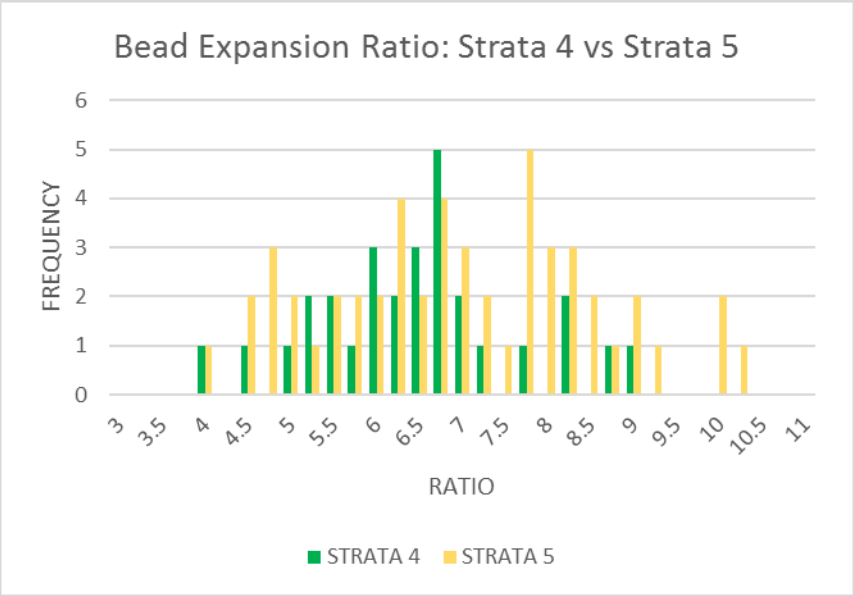

Figure 3.23 Bead-expansion ratio, strata 4 vs. strata 5

Bead-expansion ratio (ratio of bead diameter to base dendrite diameter) of mRGC processes in strata 4 and strata 5 of the ON-sublamina.

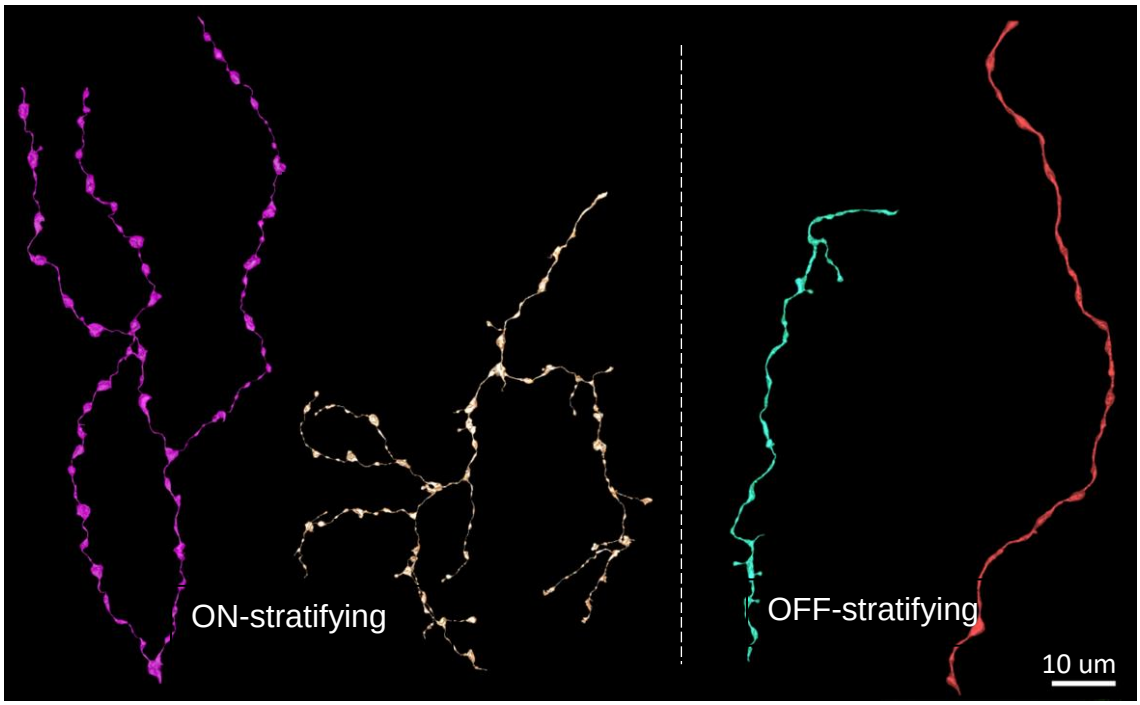

Figure 3.24 ON- and OFF-stratifying mRGC dendrites

3D reconstructions of ON-stratifying (left) and OFF-stratifying (right) mRGC dendrites in the IPL.

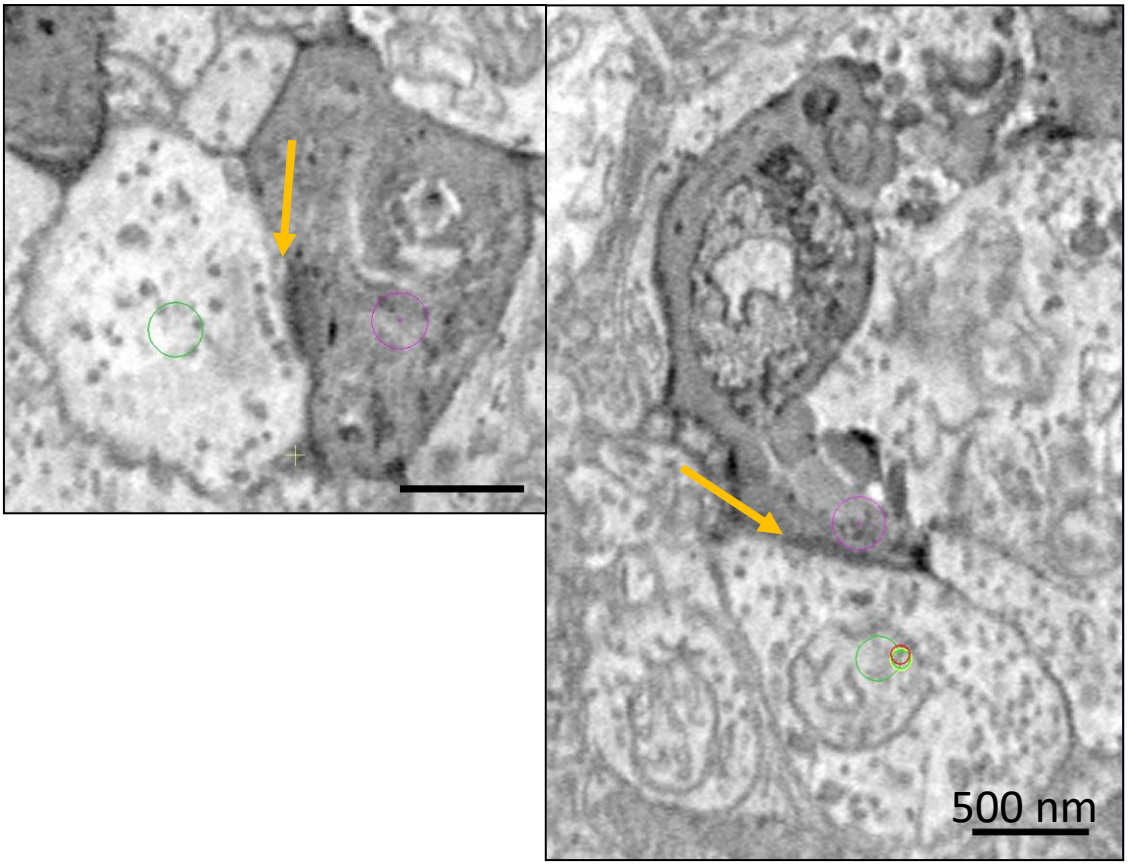

Figure 3.25 Post-synaptic density in miniSOG-labeled mRGC

Presynaptic terminals (green circle) in contact with miniSOG-labeled mRGC dendrites (purple circle). Yellow arrows point to post-synaptic densities. Scale bar is 500 nm.

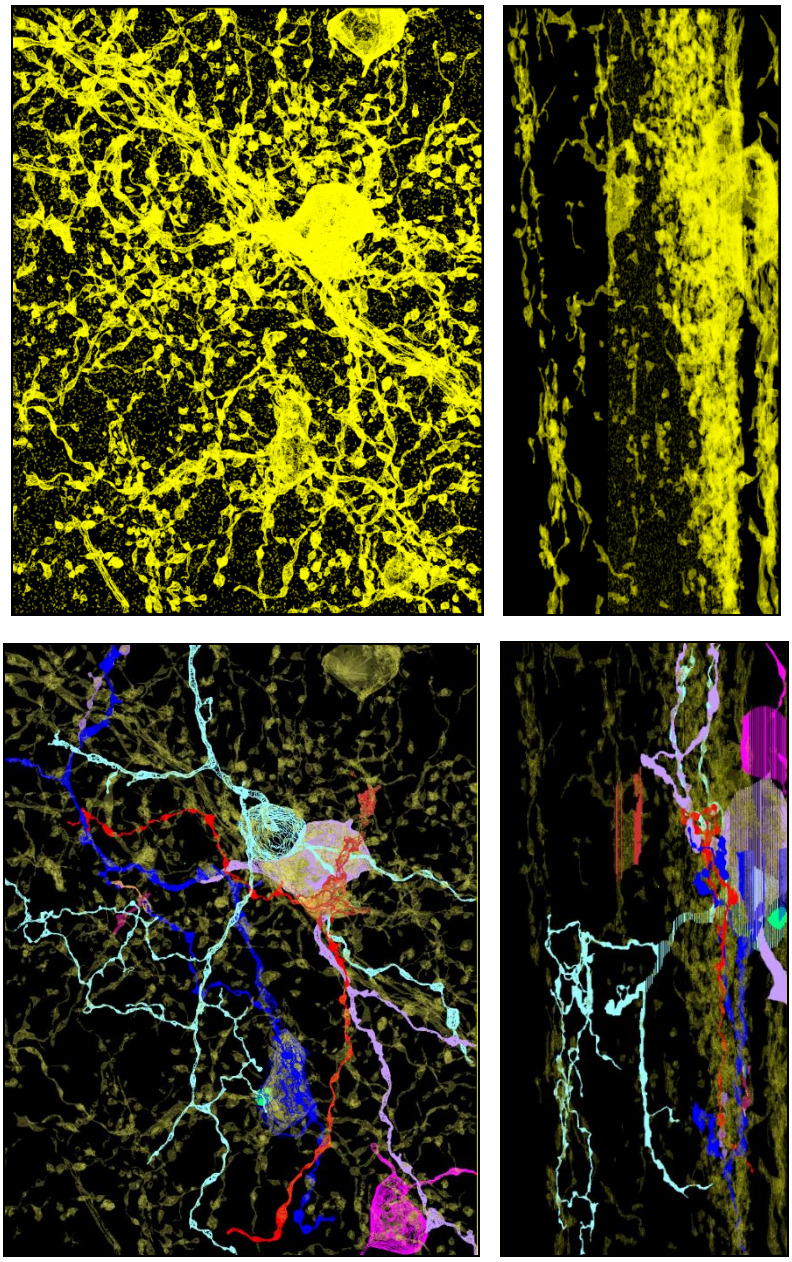

Figure 3.26 Autosegmentation results

Top: *En face* (left) and cross-sectional (right) model view of Volume_2 after thresholding for darkness. Bottom: *En face* (left) and cross-sectional (right) model view of Volume_2 after excluding objects by size and manual correction.

3.6 References

Baden, Tom, Philipp Berens, Matthias Bethge, and Thomas Euler. 2013. "Spikes in Mammalian Bipolar Cells Support Temporal Layering of the Inner Retina." *Current Biology* 23 (1). Elsevier Ltd: 48–52.

Baver, Scott B, Galen E Pickard, Patricia J Sollars, and Gary E Pickard. 2008. "Two Types of Melanopsin Retinal Ganglion Cell Differentially Innervate the Hypothalamic Suprachiasmatic Nucleus and the Olivary Pretectal Nucleus." *The European Journal of Neuroscience* 27 (7): 1763–70.

Belenky, Michael A, Cynthia A. Smeraski, Ignacio Provencio, Patricia J. Sollars, and Gary E. Pickard. 2003. "Melanopsin Retinal Ganglion Cells Receive Bipolar and Amacrine Cell Synapses." *The Journal of Comparative Neurology* 460 (3): 380–93.

Berson, David M., Ana Maria Castrucci, and Ignacio Provencio. 2010. "Morphology and Mosaics of Melanopsin-Expressing Retinal Ganglion Cell Types in Mice." *The Journal of Comparative Neurology* 518 (13): 2405–22.

Berson, David M, Felice A Dunn, and Motoharu Takao. 2002. "Phototransduction by Retinal Ganglion Cells That Set the Circadian Clock." *Science (New York, N.Y.)* 295 (5557): 1070–73.

Carter-Dawson, L, and Matthew M LaVail. 1979. "Rods and Cones in the Mouse Retina." *Journal of Comparative Neurology* 188: 263–72.

Deerinck, Thomas J, Eric A Bushong, Andrea Thor, and Mark H Ellisman. 2010. "NCMIR Methods For 3D EM : A new protocol for preparation of biological specimens for serial block face scanning electron microscopy," 6–8.

Dumitrescu, Olivia N., Francesco G. Pucci, Kwoon Y. Wong, and David M. Berson. 2009. "Ectopic Retinal ON Bipolar Cell Synapses in the OFF Inner Plexiform Layer: Contacts with Dopaminergic Amacrine Cells and Melanopsin Ganglion Cells." *Journal of Comparative Neurology* 517 (2): 226–44.

Ecker, Jennifer L, Olivia N Dumitrescu, Kwoon Y Wong, Nazia M Alam, Shih-Kuo Chen, Tara LeGates, Jordan M Renna, Glen T Prusky, David M Berson, and Samer Hattar. 2010. "Melanopsin-Expressing Retinal Ganglion-Cell Photoreceptors: Cellular Diversity and Role in Pattern Vision." *Neuron* 67 (1). Elsevier Ltd: 49–60.

Estevez, ME, PM Fogerson, MC Ilardi, Bart G Borghuis, E Chan, S Weng, ON Auferkorte, Jonathan B Demb, and David M. Berson. 2012. "Form and Function of the M4 Cell, an Intrinsically Photosensitive Retinal Ganglion Cell Type Contributing to Geniculocortical Vision." *Journal of Neuroscience*

32 (39): 13608–20.

Ghosh, Krishna K, Sascha Bujan, Silke Haverkamp, Andreas Feigenspan, and Heinz Wässle. 2004. “Types of Bipolar Cells in the Mouse Retina.” *The Journal of Comparative Neurology* 469 (1): 70–82.

Gooley, Joshua J, Jun Lu, Dietmar Fischer, and Clifford B Saper. 2003. “A Broad Role for Melanopsin in Nonvisual Photoreception.” *The Journal of Neuroscience : The Official Journal of the Society for Neuroscience* 23 (18): 7093–7106.

Güler, Ali D, Jennifer L Ecker, Gurprit S Lall, Shafiqul Haq, Cara M Altimus, Wen Liao, Alun R Barnard, Hugh Cahill, Tudor C. Badea, Haiqing Zhao, Mark W Hankins, David M Berson, Robert J Lucas, King-Wai Yau, and Samer Hattar. 2008. “Melanopsin Cells Are the Principal Conduits for Rod/cone Input to Non-Image Forming Vision.” *Nature* 453 (7191): 102–5.

Hatori, Megumi, Hiep Le, Christopher Vollmers, Sheena Racheal Keding, Nobushige Tanaka, Christian Schmedt, Timothy Jegla, and Satchidananda Panda. 2008. “Inducible Ablation of Melanopsin-Expressing Retinal Ganglion Cells Reveals Their Central Role in Non-Image Forming Visual Responses.” *PLoS ONE* 3 (6): e2451.

Hattar, Samer, H.-W. W Liao, M. Takao, D. M. Berson, and K-W W Yau. 2002. “Melanopsin-Containing Retinal Ganglion Cells: Architecture, Projections, and Intrinsic Photosensitivity.” *Science* 295 (5557): 1065–70.

Hoshi, H, W L Liu, S C Massey, and S L Mills. 2009. “ON Inputs to the OFF Layer: Bipolar Cells That Break the Stratification Rules of the Retina.” *J Neurosci* 29 (28): 8875–83.

Hu, Caiping, Dijon D Hill, and Kwoon Y Wong. 2013. “Intrinsic Physiological Properties of the Five Types of Mouse Ganglion-Cell Photoreceptors.” *Journal of Neurophysiology* 109 (7): 1876–89.

Hull, Court, Keith Studholme, Stephen Yazulla, and Henrique von Gersdorff. 2006. “Diurnal Changes in Exocytosis and the Number of Synaptic Ribbons at Active Zones of an ON-Type Bipolar Cell Terminal.” *Journal of Neurophysiology* 96 (4): 2025–33.

Joo, Hannah R, Beth B Peterson, Dennis M Dacey, Samer Hattar, and Shih-Kuo Chen. 2013. “Recurrent Axon Collaterals of Intrinsically Photosensitive Retinal Ganglion Cells.” *Visual Neuroscience* 30 (4): 175–82.

Jusuf, Patricia R., Sammy C S Lee, Jens Hannibal, and Ulrike Gr??nert. 2007. “Characterization and Synaptic Connectivity of Melanopsin-Containing

Ganglion Cells in the Primate Retina." *European Journal of Neuroscience* 26 (10): 2906–21.

Kolb, H. 1979. "The Inner Plexiform Layer in the Retina of the Cat: Electron Microscopic Observations." *Journal of Neurocytology* 8 (3): 295–329.

Kremer, J R, D N Mastronarde, and J R McIntosh. 1996. "Computer Visualization of Three-Dimensional Image Data Using IMOD." *Journal of Structural Biology* 116 (1): 71–76.

Lauritzen, J. Scott, James R. Anderson, Bryan W. Jones, Carl B. Watt, Shoeb Mohammed, John V. Hoang, and Robert E. Marc. 2013. "ON Cone Bipolar Cell Axonal Synapses in the OFF Inner Plexiform Layer of the Rabbit Retina." *Journal of Comparative Neurology* 521 (5): 977–1000.

LoGiudice, L., and G. Matthews. 2009. "The Role of Ribbons at Sensory Synapses." *The Neuroscientist* 15 (4): 380–91.

Macneil, Margaret A., John K. Heussy, Ramon F. Dacheux, Elio Raviola, and Richard H. Masland. 1999. "The Shapes and Numbers of Amacrine Cells: Matching of Photofilled with Golgi-Stained Cells in the Rabbit Retina and Comparison with Other Mammalian Species." *Journal of Comparative Neurology* 413 (2): 305–26.

Midorikawa, Mitsuharu, Yoshihiko Tsukamoto, Ken Berglund, Masaaki Ishii, and Masao Tachibana. 2007. "Different Roles of Ribbon-Associated and Ribbon-Free Active Zones in Retinal Bipolar Cells." *Nature Neuroscience* 10 (10): 1268–76.

Østergaard, Jens, Jens Hannibal, and Jan Fahrenkrug. 2007. "Synaptic Contact between Melanopsin-Containing Retinal Ganglion Cells and Rod Bipolar Cells." *Investigative Ophthalmology and Visual Science* 48 (8): 3812–20.

Schmidt, Tiffany M., Shih-Kuo Chen, and Samer Hattar. 2011. "Intrinsically Photosensitive Retinal Ganglion Cells: Many Subtypes, Diverse Functions." *Trends in Neurosciences* 34 (11). Elsevier Ltd: 572–80.

Schmidt, Tiffany M, and Paulo Kofuji. 2009. "Functional and Morphological Differences among Intrinsically Photosensitive Retinal Ganglion Cells." *Journal of Neuroscience* 29 (2): 476–82.

Schmidt, Tiffany M, and Paulo Kofuji. 2011. "Structure and Function of Bistratified Intrinsically Photosensitive Retinal Ganglion Cells in the Mouse." *The Journal of Comparative Neurology* 519 (8): 1492–1504.

Shu, Xiaokun, Varda Lev-Ram, Thomas J Deerinck, Yingchuan Qi, Ericka B Ramko, Michael W Davidson, Yishi Jin, Mark H Ellisman, and Roger Y

Tsien. 2011. “A Genetically Encoded Tag for Correlated Light and Electron Microscopy of Intact Cells, Tissues, and Organisms.” *PLoS Biology* 9 (4): e1001041.

Sommer, Christoph, Christoph Straehle, Ullrich Kothe, and Fred A. Hamprecht. 2011. “Ilastik: Interactive Learning and Segmentation Toolkit.” *Proceedings - International Symposium on Biomedical Imaging*, 230–33.

Viney, Tim James, Kamill Balint, Daniel Hillier, Sandra Siegert, Zsolt Boldogkoi, Lynn W Enquist, Markus Meister, Constance L Cepko, and Botond Roska. 2007. “Local Retinal Circuits of Melanopsin-Containing Ganglion Cells Identified by Transsynaptic Viral Tracing.” *Current Biology : CB* 17 (11): 981–88.

Zhao, X, B K Stafford, A L Godin, W M King, and K Y Wong. 2014. “Photoresponse Diversity among the Five Types of Intrinsically Photosensitive Retinal Ganglion Cells.” *J Physiol* 592 (Pt 7): 1619–36.

Chapter 4

Conclusion

"Like the entomologist in search of colorful butterflies, my attention has chased in the gardens of the grey matter cells with delicate and elegant shapes, the mysterious butterflies of the soul, whose beating of wings may one day reveal to us the secrets of the mind."

- Recollections of My Life, Santiago Ramón y Cajal

A unifying principle in neuroscience is the existence of parallel pathways that convey feature information from peripheral sensory organs to dedicated targets in the brain. One of the central themes in neuroscience is understanding how these sensory inputs integrate in the brain to effect changes in physiology and behavior. At the very root of this endeavor, and at the heart of this dissertation, is dissecting the circuits involved- identifying the inputs and outputs of a specific cell type.

The mouse retina is made up of over 60 types of cells which include include 2 different photoreceptors, 2 different horizontal cells, 12 different bipolar cells, over 30 different amacrine cells, and over 22 different retinal ganglion cells (Helmstaedter et al. 2013; Kolb et al. 2001; Masland 2011; Jeon, Strettoi, and Masland 1998). The component pieces that make up circuitry for getting rod and

cone signals to the visual cortex and superior colliculus is largely well understood. However, the players involved in conveying light information to inform non-image forming visual processes is largely unknown. What we do know, is that one of the most recently discovered retinal cells, the melanopsin-expressing retinal ganglion cells (mRGC), lies at the center of this pathway.

mRGCs are intrinsically photosensitive retinal ganglion cells which combine their melanopsin-based signaling with rod and cone signals to inform regions of the brain, like the suprachiasmatic nucleus (SCN) and the olivary pretectal nucleus (OPN) which are dedicated to non-image forming (NIF) visual processes such as circadian photoentrainment and pupillary light reflex (PLR), respectively (Berson, Dunn, and Takao 2002; Hattar et al. 2002). In addition to the SCN and OPN, mRGCs have been shown to also send axons to the intergeniculate leaflet (IGL), the ventral lateral geniculate nucleus (vLGN), and most recently, the dorsal LGN (dLGN, classically thought of as an image-forming brain region).

How does one genetically-defined cell type facilitates such diverse functions that occur on such different time scales (hours to days to for photoentrainment, milliseconds to seconds for PLR) and are mediated by such anatomically distinct regions? Do the five subtypes of mRGCs serve specific functions? Since structure and function are intimately related, if mRGC subtypes served specific functions, they should have unique structures that served those functions. In this case, structure means where they are located in the retina, where their dendrites stratify and make connections in the retina, and where their

axons project to and make connections in the brain.

To answer these questions, we injected AAV into the eyes of a transgenic melanopsin-cre mouse (*Opn4*^{Cre}) to target the expression of membrane-tethered miniSOG (miniSOG-farnesyl, miniSOG), a correlated light and electron microscopy label, specifically to mRGCs. The AAV allows for a large amount of miniSOG to be made within the mRGCs, and the farnesylation signal targets the miniSOG-expression to the plasma membrane. Upon photooxidation of the miniSOG under blue light in the presence of diaminobenzidine (DAB), the singlet oxygens miniSOG polymerizes the DAB. The polymerized DAB is then stained for serial blockface scanning electron microscopy (SBEM). In our SBEM volumes of suprachiasmatic nucleus (SCN), olivary pretectal nucleus (OPN), intergeniculate leaflet (IGL), ventral lateral geniculate nucleus (vLGN), dorsal lateral geniculate nucleus (dLGN), and optic nerve (ON), the miniSOG appears as a dense, black label that fills mRGC axons and dendrites, and is concentrated at the plasma membrane of the mRGC somata.

From the studies described in Chapter 2, we see that mRGCs as a group, send axons to image-forming and non-image-forming regions of the brain and that the way in which the mRGCs (again, as a group) interact with those brain regions is different. In the SCN, mRGC boutons are small, most contain only one mitochondria, make *en passant* synapses with the SCN neurons, and are found on thin unmyelinated axons. In the OPN, mRGC boutons are 81% larger than in the SCN and, 66% have more than one mitochondria, and 58% have deep invaginations that engulf dendritic spines and glial processes. Also, OPN axons

are myelinated, are 50% wider, had more boutons per unit length of axon, twice as many branch points, and longer distances of axon between branch points than in the SCN. In the IGL, boutons were similar in volume and mitochondria content as compared to the OPN, but had less spine intrusions than OPN. mRGC boutons in the vLGN were 50% larger than in the OPN, and those in the dLGN showed much greater variation in volume, but were on the whole nearly three times larger than in the OPN. Overall, we see that in the 5 mRGC-recipient brain regions, there are significant differences in bouton morphology and ultrastructure.

The miniSOG also let us visualize and reconstruct the mRGCs in the retina. From our complete segmentation of all miniSOG-labeled processes, we see that mRGC processes occupy 0.4% of the volume of the IPL with 82% of all miniSOG-labeled processes stratifying in strata 4 and 5 and that mRGC processes cover 56.6% of the surface area of the retina. From three miniSOG-labeled retina volumes, we segmented a total of 9 mRGCs and from segmenting those 9 mRGCs found variation in synaptic density, branching frequency, dendritic beading pattern, and soma size. While soma size is often used to identify cell types, it is often highly variable and is thus a weak classifier (Sun, Li, and He 2002; Coombs et al. 2006; Volgyi, Chheda, and Bloomfield 2009). In fact, Hu, Hill, and Wong 2013 report that they found that the mRGC cell bodies changed shape and size during recording so soma size was an unreliable feature to use to classify mRGC subtypes. However, by comparing the segmented objects from all other miniSOG-labeled processes in volume_3, we find that branching frequency, interbead distance, and bead-expansion ratio are all

correlated with the strata of the IPL that those processes stratify in. This is even more convincing when looking at those same features in V3_middle, the bistratified M3 subtype mRGC that was segmented in Volume_3. In V3_middle, internal branch length (a measure of branching frequency), and interbead distance are all smaller for the dendrites that stratify in the ON sublamina and bead expansion ratio was greater in the ON sublamina compared to the OFF sublamina; all within one single cell. If these features were more subtype-specific, we would have expected to see that the features would not change regardless of the strata of ramification.

Lastly, using the miniSOG label with SBEM allowed us to collect large volumes of tissue with ultrastructural resolution. We are able to identify putative synapses between mRGCs and other cells in the IPL by the presence of docked synaptic vesicles, continuous stretches of shared membrane, and in some cases, the presence of a post-synaptic density. By using similar segmentation protocols from on identified putative synapses, we reconstructed over 100 bipolar and amacrine cells that synapse onto the five subtypes of mRGCs. Because we were unable to follow all marked synapses to a bipolar cell or amacrine cell body, our reconstructions of presynaptic partners cannot be used to determine the percentage of any one cell types influence on any one mRGC subtype. They can, however, be used as a catalog to show, at the minimum, what cells are involved in the circuitry of a particular mRGC. Because of similar axonal/dendritic diameters and branching patterns (which determines how difficult it is to follow a particular cell type), we can compare the frequency with which a cell type is

reconstructed between mRGC subtypes. Amacrine cells to the ON-sublamina were few and far between because of how thin the amacrine cell processes were and how far we would have to follow those thin processes back to a cell body. However, for bipolar cells, the presynaptic bipolar cell inputs are dependent on mRGC dendritic stratification within the IPL.

For example, even though M4 and M5 both stratify in the ON-sublamina, M4 mRGC dendrites ramify closer to the inner edge of strata 4 and M5 dendrites ramify closer to the inner edge of strata 5. As such, in comparing the bipolar cell inputs to these cell types, type 8 bipolar cells, which stratify in strata 5, are more commonly found in association with the M4 mRGC. Also, M1s and M3s receive ectopic inputs from axons of ON-bipolar cells in the OFF-sublamina, these ectopic inputs do not occur on ON-stratifying dendrites in the ON-sublamina. Thus, we are not seeing a bipolar cell type with a penchant for axonal synapses, but rather a stratification-dependent feature as both M1 and M3s are affected.

Taken all together, the increased detail regarding the input and outputs of the mRGCs adds weight to the idea that different subtypes of mRGCs may serve different functions.

Because stratification within the IPL determines so many aspects of dendritic morphology, the mRGC subtypes, which stratify differentially within the IPL will noticeably have different dendritic morphologies. M2s, M4s, and M5s which stratify in the ON-sublamina of the IPL would have more prominent and frequent beads and shorter and more frequent branches. Since the beaded varicosities on the mRGC dendrites are known to contain mitochondria, the M2s

and M5s would thus have more frequent mitochondria along their dendritic lengths. The increased mitochondria could be a result of the type/signaling rate of inputs these mRGCs receive based on the types of bipolar and amacrine cells that terminate in the IPL layers where the M2 and M5 dendrites stratify. Considering that M2, M4, and M5 mRGCs are much less intrinsically photosensitive than the M1 mRGCs (Schmidt and Kofuji 2009; Zhao et al. 2014), their function in the retina may not be as dependent on the intrinsic photosensitivity of melanopsin and, instead more dependent on chemical information from bipolar and amacrine cells. M2, M4, and M5 mRGCs have been shown to have increased spontaneous spike rates, as compared to M1 and M3 subtypes (Zhao et al. 2014). The increased mitochondria that we see here may facilitate that response. The increased bead expansion ratio may also affect the physiology of the cell by increasing the surface area with which an ON-stratifying mRGC uses to contact bipolar and amacrine cells. The increased surface area may help make up for the decreased expression of melanopsin as compared to the M1 mRGC subtype.

The M1 mRGCs monostratify in the OFF-sublamina of the IPL and would supposedly only receive input from OFF-bipolar cells. However, we show that they in fact receive a significant amount of ON-bipolar cell input in addition to OFF-bipolar cells and amacrine cells. Given that the M1 has a net ON-response, and the fact that the OFF-stratifying mRGC processes are less beaded and less branched, it is possible that the M1 mRGC ON-response is dependent more on its own melanopsin-based intrinsic photosensitivity as opposed to a bipolar or

amacrine cell driven response. Taken into consideration with the non-M1s lesser intrinsic photosensitivity, but increased branching and beading by virtue of its stratification within the IPL, the increased branching and beading features seen in the ON-sublamina may be a manifestation of a decreased dependency on melanopsin-based input and an increased dependency on rod and cone driven inputs.

If we factor this significant rod and cone based input into the function of mRGCs, our findings suggest that non-M1s have significant rod and cone input and thus may play a far larger role in image-forming vision that once previously thought. In our segmentation of miniSOG-labeled mRGC processes in different retinal-recipient brain regions, we find significantly larger miniSOG-labeled mRGC terminals in the dorsal lateral geniculate nucleus (dLGN) and ventral lateral geniculate nucleus (vLGN)- regions of the brain classically thought to be involved in image-forming vision. Retrograde labeling studies to the dLGN showed that half of M2, M3, and M5 mRGC subtypes were labeled but that nearly all M4 subtypes were labeled (Estevez et al. 2012). If soma size is correlated with axon caliber (Williams and Chalupa 1983) and if axon caliber is proportional to bouton volume, then perhaps the variation seen in dLGN is related to the variety of mRGC subtypes that project to the dLGN. If this is the case, the much smaller variation in bouton size seen in the suprachiasmatic nucleus (SCN) would be due to a narrower subset of mRGC inputs. Because there are no techniques to preferentially label M3, M4, or M5 subtypes, it is unknown what roles these subtypes might play in the SCN.

Lastly, Zhao et al. 2014 showed that M2-M5 mRGC subtypes have center-surround receptive fiends. Combined with the fact that M2-M5 dendritic processes will stratify in the ON-sublamina where they are more highly branched, heavily beaded, and subsequently, mitochondria-laden and the fact that M2-M5 can be retrogradely labeled from the dLGN, the highly rod/cone dependent input to mRGCs in the ON-sublamina may be driving image-forming vision in the dLGN. The excluded M1, with its high intrinsic photosensitivity, long, thin, less-branched, less-beaded dendrites may then stand out as the true irradiance detector that signals to the circadian pacemaker.

Overall, these studies have filled in many colors of this paint-by-number piece describing the connectivity of mRGCs. The results of these studies reveal striking ultrastructural differences between mRGC subtypes, mRGC processes that stratify in different sublamina, and mRGC-recipient brain regions which highlight the fact that mRGCs are a heterogeneous group of cells that mediate a variety of functions. Our findings validate many other mRGC circuitry studies and provides many new details regarding different cell types that might be involved in mRGC-subtype-specific circuitry.

4.1 References

Berson, David M, Felice A Dunn, and Motoharu Takao. 2002. "Phototransduction by Retinal Ganglion Cells That Set the Circadian Clock." *Science (New York, N.Y.)* 295 (5557): 1070–73.

Hattar, Samer, H.-W. W Liao, M. Takao, D. M. Berson, and K-W W Yau. 2002. "Melanopsin-Containing Retinal Ganglion Cells: Architecture, Projections, and Intrinsic Photosensitivity." *Science* 295 (5557): 1065–70.

Helmstaedter, Moritz, Kevin L. Briggman, Srinivas C. Turaga, Viren Jain, H. Sebastian Seung, and Winfried Denk. 2013. "Connectomic Reconstruction of the Inner Plexiform Layer in the Mouse Retina." *Nature* 500 (7461). Nature Publishing Group: 168–74.

Jeon, C J, E Strettoi, and R H Masland. 1998. "The Major Cell Populations of the Mouse Retina." *The Journal of Neuroscience : The Official Journal of the Society for Neuroscience* 18 (21): 8936–46.

Kolb, H, R Nelson, P Ahnelt, and N Cuenca. 2001. "Cellular Organization of the Vertebrate Retina." *Progress in Brain Research* 131: 3–26.

Masland, Richard H. 2011. "Cell Populations of the Retina: The Proctor Lecture." *Investigative Ophthalmology and Visual Science* 52 (7): 4581–91.

Sekaran, S., D. Lupi, S. L. Jones, C. J. Sheely, S. Hattar, K. W. Yau, R. J. Lucas, R. G. Foster, and M. W. Hankins. 2005. "Melanopsin-Dependent Photoreception Provides Earliest Light Detection in the Mammalian Retina." *Current Biology* 15 (12): 1099–1107.

Williams, R W, and L M Chalupa. 1983. "An Analysis of Axon Caliber within the Optic Nerve of the Cat: Evidence of Size Groupings and Regional Organization." *The Journal of Neuroscience : The Official Journal of the Society for Neuroscience* 3 (8): 1554–64.

Zhao, X, B K Stafford, A L Godin, W M King, and K Y Wong. 2014. "Photoresponse Diversity among the Five Types of Intrinsically Photosensitive Retinal Ganglion Cells." *J Physiol* 592 (Pt 7): 1619–36.